# INSTITUTO DE FISICA – FACULTAD DE CIENCIAS UNIVERSIDAD AUTONOMA DE SAN LUIS POTOSI



#### Uncontrollable Errors in the Measurements of an Atomic Gravimeter & A Novel Hybrid Microwave Interferometer for Detection of Molecular Interactions

#### 

# Thesis advisor **Dr. Eduardo Gómez García**

A thesis submitted to the Instituto de Física, Facultad de Ciencias UASLP in the fulfillment of the requirements for the degree of Doctorado en Ciencias (Física)

San Luis Potosí, S.L.P., México 27 de Noviembre del 2025

#### Uncontrollable Errors in the Measurements of an Atomic Gravimeter & A Novel Hybrid Microwave Interferometer for Detection of Molecular Interactions.

# Dr. Antonio Morelos Pineda Presidente Dr. Jürguen Engelfried Jatzkowski Sinodal Dr. John Alexander Franco Villafañe Sinodal Dr. Jesús Urías Hermosillo Sinodal Dr. Rubén Flores Mendieta Sinodal Suplente Dr. Fernando Ramírez Martínez Sinodal Externo

THESIS COMMITTEE

Uncontrollable Errors in the Measurements of an Atomic Gravimeter & A Novel Hybrid Microwave Interferometer for Detection of Molecular Interactions © 2025 by Juan Mario Cervantes Martinez is licensed under Creative Commons Attribution-NonCommercial-NoDerivatives 4.0 International.

To view a copy of this license, visit https://creativecommons.org/licenses/by-nc-nd/4.0/

# Acknowledgments

I want to thank my family for their constant support during my Ph.D. especially to my mother whose always been a role model for me. I want to thank my friends for always cheering me up and being wonderful people. Lastly, I particularly want to thank my thesis advisor for his unwavering patience and professional wisdom; I aspire to be as great a scientist as he is.

# Contents

List of Figures v				
Αl	ostra	ect I	ix	
1	Uno	controllable Errors in the Measurements of an Atomic Gravimeter	1	
	1.1	Introduction	1	
	1.2	Phase Writing on Atoms	2	
	1.3	The Case With No Aperture	4	
	1.4	Far Field Diffraction	6	
	1.5	Near Field Diffraction	8	
	1.6	Photon Recoil Correction	15	
	1.7	Conclusion	20	
A۱	ostra	et II	22	
<b>2</b>	AN	Novel Hybrid Microwave Interferometer for Detection of Molecular		
	Inte	eractions	<b>23</b>	
	2.1	Introduction	23	
	2.2	Traditional methods	25	
		2.2.1 Fluorescence and Absorption	25	
		2.2.2 Phase Change	28	
	2.3	Hybrid Microwave-Optical Interferometer	32	
		2.3.1 Signal Current for the hybrid microwave-optical interferometer	33	
		<ul><li>2.3.2 Index of refraction for the hybrid microwave-optical interferometer</li><li>2.3.3 Analytical approximations for the hybrid microwave-optical inter-</li></ul>	35	
		ferometer signal	36	
	2.4	Conclusions	44	
$\mathbf{A}$	Diff	raction of a Gaussian beam by a square aperture	53	
В		ntributions to the wavefront curvature from a square aperture in the field.	55	
$\mathbf{C}$	Der	ivation of the optical Bloch equations for the three-Level $\Lambda$ System	57	
D		proximations for the steady-state of the optical Bloch equations of three-Level $\lambda$ system.	63	

# List of Figures

1.1	The depiction of the experimental configuration in the numerical simulation illustrates the Raman beam, the atomic cloud, and the aperture. The Raman beam consists of a non-diffracted Gaussian beam alongside a diffracted and retro-reflected Gaussian beam, with the atomic cloud interacting with both beams	9
1.2	The phase shift is examined as a function of the aperture size $(a)$ normalized to the beam waist $(W_0)$ . In this case, $z=2$ m, $W_0=1.5$ cm, and $\lambda=780$ nm, with all atoms initially located at the origin, displaying a "transverse" temperature of $T_b=1~\mu{\rm K}$ and a duration of $T=20$ ms. a) The findings are shown for a circular aperture (in blue) and a square aperture (in green). The inset offers a zoomed-in view to highlight the oscillations. b) The raw data and the envelope of the phase shift for the circular aperture (blue) follow the function $e^{-a^2/W_0^2}$ (indicated by the solid red line, see Eq. 1.32), while the square aperture (green) aligns with a similar function $(1/20)e^{-1.15a^2/W_0^2}$ (represented by the dashed orange line).	10
1.3	The transverse phase of the beam that has been diffracted through a circular aperture is described by Equations 1.25 and 1.30. In our analysis, we set the parameters as follows: $z_0=10^3$ m, $\lambda=780$ nm, $z_W=0$ , $z=2$ m, and $a=W_0\simeq 1.5$ cm. For the sake of clarity in visualization, a phase offset of $-\pi/2$ was incorporated into the plot	11
1.4	The phase shift of the interference fringes is analyzed as a function of the aperture size, incorporating the diffraction effect across all pulses (represented in blue) or solely on the initial pulse (depicted in red). The oscillations correspond to the phase shift of the diffracted beam's field (as indicated in Eq. 1.32, shown in green dashed lines). The parameters utilized include $z=2$ m, $z_W=0$ m, $z_0=10^3$ m, $\lambda=780$ nm, and $\sigma_A=10^{-7}$ m	12
1.5	The envelope of the oscillations in the phase shift of the interference fringes is illustrated as a function of the initial width $(\sigma_A)$ of the atomic cloud (shown in blue). This behavior is explained by Equation 1.38 (represented by the dashed red line). The effect significantly decreases when the cloud size surpasses the cutoff value $\sigma_{\Psi}$ (marked by the vertical line, Equation 1.36). The parameters used in this analysis include $z_0 = 1000$ m, $\lambda = 780$ nm, $z = 2$ m, $W_0 = 1.5$ cm, $a \simeq 2W_0$ , $T_b = 1\mu K$ , $T = 20$ ms, and $\Omega_0 = 2\pi \times 10^3$ rad/s	13
1.6	A ring of emitters is positioned at the aperture for a) a circular aperture in contrast to b) a square aperture. The point $P$ is located on the axis at a distance $z$ from the aperture	15

1.7	The depiction of a Gaussian beam emphasizes three regions where the propagation vector exhibits a transverse component. The red arrows indicate the direction of the propagation vector, while the black dashed lines illustrate the curvature of the wavefront. In zones a) and c), the transverse component of the propagation vector can be intuitively inferred from the curvature of the wavefront. Conversely, in zone b), the emergence of the transverse component of the propagation vector is attributed to the enhanced spatial confinement of the beam, as this region corresponds to the beam's waist.	16
1.8	The absolute value of the photon recoil correction is presented as a function of aperture size for both the phase gradient term (depicted in blue) and the amplitude-dependent term (illustrated in red), corresponding to the first and second terms in Equation 1.40. In this analysis, we have excluded the oscillating component and retained only the envelope. The parameters utilized include $z_0 = 10^3$ m, $\lambda = 780$ nm, $z = 2$ m, $W_0 = 1.5$ cm, $z_W = 0$ , and $\sigma_A = 1.4 \times 10^{-5}$ m	18
1.9	The absolute value of the photon recoil correction is presented as a function of the atomic cloud size, distinguishing between the amplitude term (depicted in red) and the phase gradient term (illustrated in blue). For the amplitude term, a similar averaging effect is observed as shown in Fig. 1.5, with a comparable cutoff size indicated by Eq. 1.36 (represented by the green dashed vertical line). In contrast, the phase gradient term achieves its maximum value near the cutoff size but remains lower than the contribution from the amplitude term. The parameters utilized include $z_0 = 1000 \text{ m}$ , $\lambda = 780 \text{ nm}$ , $z = 2 \text{ m}$ , $W_0 = 1.5 \text{ cm}$ , $z_W = 0$ , and $a \simeq 2W_0$ .	19
1.10	The absolute value of the fractional correction in gravimetry, represented as $\delta g/g$ , is due to wavefront aberrations (shown in blue) and the photon recoil correction (shown in red), which correspond to the first and second terms of Equation 1.50. The parameters used are $z_0 = 1000$ m, $\lambda = 780$ nm, $z = 2$ m, $W_0 = 1.5$ cm, $z_W = 0$ , and $\sigma_A = 10^{-7}$ m	20
2.1	Illustration of several common detection methods, $a$ ) fluorescence spectroscopy, $b$ ) absorption spectroscopy, $c$ ) Mach-Zehnder interferometer for phase change measurements. In this figure $D$ is a photodiode detector, B.S. stands for Beam Splitter and M for Mirror. Figure $d$ ) show a diagram of a two-level quantum system with decay rate $\gamma$ being driven by an external electric field of frequency $\omega_l$ and detuning $\delta_{ab}$	26
2.2	Graph of the coefficient of population $\rho_{aa}$ for the excited state $ a\rangle$ as a function of the detuning $\delta_{ab}$ . For b) I have plotted the ratio $\rho_{aa}/ \Omega_{ab} ^2$ as it appears in Eqs. 2.20 and 2.21. For both graphs I have plotted several values for the Rabi frequency, for the solid blue line $ \Omega  = 1\gamma$ , for the red dashed line $ \Omega  = 2\gamma$ , and for the green dot-dashed line $ \Omega  = 5\gamma$	29
2.3	Graph of the coefficient of coherence $\rho_{ab}$ between the excited $ a\rangle$ and ground levels $ b\rangle$ as a function of the detuning $\delta_{ab}/\gamma$ . For $b$ ) I have plotted the real part of the ratio $\rho_{ab}/\Omega_{ab}$ as it appears in Eq. 2.38. For both graphs I have plotted several values of the Rabi frequency, for the solid blue line $ \Omega  = 1\gamma$ , for the red dashed line $ \Omega  = 2\gamma$ , and for the green dot-dashed	
	line $ \Omega  = 5\gamma$	32

2.4	a) Schematic for the hybrid microwave-optical interferometer, in this figure $\omega_l$ is the laser frequency, $\omega_m$ is the modulation frequency, D is the detector	
	(photodiode), MW stands for microwave, X is a current mixer and LPF	
	stands for low-pass filter. b) Energy diagram of the three-level system, $\Omega_{ab}$	
	and $\Omega_{ac}$ are the Rabi frequencies of the system, $\gamma_{ab}$ and $\gamma_{ac}$ are the decay	
	rates from the excited state $ a\rangle$ , $\delta_{ab}$ and $\delta_{ac}$ are the one-photon detunings,	
	$\delta_{cb}$ is the two-photon detunig. See appendix C for their definitions	33
2.5	Plot of the real components of the coherence's $\rho_{ab}/\Omega_{ab}$ , in solid blue, and	
	$\rho_{ac}/\Omega_{ac}$ , in dasehd red, as a function of the detuning of one of the beams	
	$(\delta_{ab}/\gamma)$ given by Eq. D.1. For all plots $\gamma_{ab} = \gamma_{ac} = \gamma$ and $\Omega_{ab} = \Omega_{ac} = \Omega$ .	
	For a), $\Omega = 30\gamma$ and $\delta_{ac} = -100\gamma$ . For b) $\Omega = 60\gamma$ and $\delta_{ac} = -100\gamma$ . For	
	c), $\Omega = 30\gamma$ and $\delta_{ac} = -200\gamma$ . For d), $\Omega = 60\gamma$ and $\delta_{ac} = -200\gamma$	38
2.6	Plot of the real components of the coherence's $\rho_{ab}/\Omega_{ab}$ and $\rho_{ac}/\Omega_{ac}$ as a	
	function of the detuning of one of the beams $(\delta_{ab})$ . Solid lines are given by	
	Eq. D.1, dashed lines are given by Eq. 2.73. For all plots $\gamma_{ab} = \gamma_{ac} = \gamma$	
	and $\Omega_{ab} = \Omega_{ac} = \Omega$ . For $a$ , $\Omega = 30\gamma$ and $\delta_{ac} = -100\gamma$ . For $b$ , $\Omega = 60\gamma$	
	and $\delta_{ac} = -100\gamma$ . For $c$ , $\Omega = 30\gamma$ and $\delta_{ac} = -200\gamma$ . For $d$ , $\Omega = 60\gamma$ and	
	$\delta_{ac} = -200\gamma \dots $	39
2.7	Plot of the real components of the coherence's $\rho_{ab}/\Omega_{ab}$ (blue) and $\rho_{ac}/\Omega_{ac}$	
	(red) as a function of the detuning of one of the beams $(\delta_{ab}/\gamma)$ . Solid lines	
	are the full solution (Eq. D.1), in blue $\rho_{ab}$ and in red $\rho_{ac}$ , dashed lines	
	are the approximation detuned from the two-photon resonance (Eq. D.6)	
	and dotted lines are the linear approximation at the two-photon resonance	
	(Eq. D.2). At higher detunings both curves follow the envelope given by	
	Eq. D.4. For both plots $\gamma_{ab} = \gamma_{ac} = \gamma$ , $\Omega_{ab} = \Omega_{ac} = \Omega$ and $\delta_{ac} = -200\gamma$ .	
	For a) $ \Omega  = 40\gamma$ and for b) $ \Omega  = 100\gamma$	39
2.8	Plot of the real components of the differential normalized coherence's	
	$(\rho_{ab}/\Omega_{ab} - \rho_{ac}/\Omega_{ac})$ as a function of the two-photon detuning $\delta_{cb}/\gamma$ . Solid	
	blue lines are the full solution (Eq.D.1) and red dashed lines are the ana-	
	lytical approximations. In both graphs $\gamma_{ab} = \gamma_{ac} = \gamma$ and $\Omega_{ab} = \Omega_{ac} = \Omega$ .	
	For a) in red Eq.D.3 $\Omega = 20\gamma$ , $\delta_{ab} \approx \delta_{ac} = 1000\gamma$ . For b) in red Eq.D.11	11
2.0	$\Omega_H = 30\gamma$ and $\delta_{ab} \approx \delta_{ac} = 1000\gamma$	41
2.9	corresponding Rabi frequency as a function of the one-photon detuning	
	corresponding Rabi frequency as a function of the one-photon detuning $\delta_{ab}/\gamma$ . The graph is centered around the two-photon resonance $\delta_{cb} = 0$	
	$\delta_{ab} / \delta_{ac}$ . The graph is centered around the two-photon resonance $\delta_{cb} = 0 = \delta_{ab} - \delta_{ac}$ . For both graphs $\Omega_{ab} = \Omega_{ac} = \Omega$ and $\gamma_{ab} = \gamma_{ac} = \gamma$ . For a)	
	$\delta_{ac} = 100\gamma$ , in blue $ \Omega  = 10\gamma$ and in red $ \Omega  = 20\gamma$ . For b) $\delta_{ac} = 200\gamma$ , in	
	blue $ \Omega  = 10\gamma$ and in red $ \Omega  = 20\gamma$	42
2.10	Phase difference $(\phi_1 - \phi_2)$ , with an OD = 1, as a function of two parameters,	12
	$\delta_{ac}$ , which is the detuning of the non-modulated laser with respect to the	
	$a \leftrightarrow c$ transition, and modulation frequency $\omega_m$ . For this graph $\gamma_{ab} =$	
	$\gamma_{ac} = \gamma$ , $\Omega_{ac} = \Omega_{ab} = \Omega = 5\gamma$ , and the two-photon transition frequency	
	$\omega_{cb} = 25\gamma$	43

#### Abstract I

There is a persistent interest in minimizing the dimensions of portable atomic gravimeters. This reduction inevitably results in the truncation of the Gaussian wings of the excitation laser beams, the implications of which have not yet been fully assessed. The diffraction pattern generated by this aperture creates ripples in the wavefront, influencing both the phase and the intensity. We examine the alteration in the measured value of an atomic gravimeter due to phase fluctuations in the wavefront. Fortunately, this alteration demonstrates a Gaussian decay in relation to the size of the aperture. For larger clouds, we notice a reduced effect due to averaging across transverse positions that show different shift values. Interestingly, we found that variations in intensity also provide a notable correction to the photon recoil, contributing roughly equally to the previously mentioned shift in the measurement of gravitational acceleration. Our results should aid in establishing the minimum size of an apparatus necessary to achieve a certain level of accuracy.

## Chapter 1

# Uncontrollable Errors in the Measurements of an Atomic Gravimeter

#### 1.1 Introduction

Interferometry stands as one of the most beneficial techniques available to scientists, offering versatile applications across various scientific disciplines that significantly enhance the accuracy of numerous measurements. An interferometer utilizes the interference patterns of coherent waves to glean insights about the system under investigation. Historically, the wave theory of light was bolstered by Thomas Young's inquisitive nature, as he demonstrated the wave nature of light through his famous double slit experiment, effectively challenging Isaac Newton's corpuscular theory. This pivotal moment marked the beginning of the practical application of coherent wave interference. Among the most notable historical applications of interferometry is the Michelson-Morley experiment, which indirectly established that light does not require a medium for its propagation [1].

In recent years, interferometry has become extensively utilized for measuring the lengths and shapes of optical components with nanometer precision. One of the most remarkable achievements of contemporary interferometry was the measurement and detection of gravitational waves coming from the collision between two black holes, further validating Albert Einstein's most significant theory.

The technique of interferometry extends beyond the realm of electromagnetic waves. Following the identification of matter interference at atomic and sub-atomic levels, along with the advancement of quantum mechanics, matter-wave interferometers have demonstrated significant efficacy. In recent decades, cold atom interferometers [2, 3] have emerged as a valuable instrument for inertial sensing [4], capable of measuring various phenomena such as gravitational acceleration [5, 6, 7], gravity gradients [8, 9], and rotational movements [10, 11, 12]. Furthermore, these interferometers have been employed in fundamental physics research, including the determination of the fine structure constant [13, 14], the Newtonian gravitational constant [15, 16], tests of the weak equivalence principle [17, 18, 19], and the detection of gravitational waves [20, 21, 22]. Recently, there have also been proposals to utilize them as detectors for ultralight dark matter [23]. In the context of their application in the field, these sensors have undergone ongoing miniaturization to transform them into portable devices capable of measuring, for instance, the local gravitational acceleration [24, 25, 6, 26, 27, 28, 29, 30, 31, 32, 33, 34].

The accuracy of atomic gravimeters is frequently constrained by the distortions present

in the wavefront of the Raman beams employed for excitation [35, 36, 37, 38, 39, 40, 23]. These distortions can be mitigated through meticulous design of the Raman pathway, which begins with spatially filtered beams and incorporates optical components characterized by high surface flatness.

The wavefront can be actively controlled in addition to the aforementioned methods [41]. Furthermore, an in situ characterization of the beam profile can be achieved through measurements conducted with the atomic cloud [42, 40]. Additionally, it is possible to directly characterize and rectify the deformations on the wavefront that have the most significant impact [43].

A sufficiently uniform laser illumination on atoms minimizes decoherence, which can be accomplished through the use of flat-top beams [44, 45] or collimated Gaussian beams with a large waist [46, 37]. The combination of large laser beams and the smaller dimensions necessary for portable devices results in truncated Gaussian beams.

It is evident that there is a significant necessity to assess the impact of an aperture in atomic gravimetry [26, 9]. Reference [38] discovered that altering the size of an aperture in the Raman beams results in a notable shift in gravity measurements. The method of adjusting the diameter of the Raman beams through the implementation of an aperture has been widely adopted in various studies [47, 48]. However, their analysis overlooks the diffraction effects, which we demonstrate to be quite significant.

This thesis provides an examination of how an aperture influences the trajectory of Raman beams. The presence of the aperture alters both the phase and amplitude of the wavefront, and our findings indicate that these changes result in a significant shift in the measurement of gravitational acceleration (g) that must be considered.

The structure of the thesis is organized as follows: Chapter 1.2 presents a clear explanation of how to express the phase of the beams in relation to atomic states. Chapter 1.3 investigates the situation without an aperture, establishing a foundational reference for further analysis. Chapter 1.4 discusses the far field case, which, although not directly applicable to atomic gravimetry, offers important insights into diffraction effects. In Chapter 1.5, we delve into the near field scenario, which is more pertinent to practical applications. Lastly, Chapter 1.6 introduces the correction for photon recoil caused by the aperture, which we have found to have a significant effect on intensity variations.

#### 1.2 Phase Writing on Atoms

In this chapter we will show how the phase of the interferometric beams are written on the final states of the atoms. we will consider that the beams are very close to resonance, meaning that its momentum is not far of from the design trajectory. The equations for the dynamics of the two states of the atom for the first pulse are

$$i\dot{C}_{e,1} = \frac{1}{2}\Omega e^{i\phi_{\Omega,1}} e^{i\delta t} e^{i\Delta t^2} C_{g,1} \qquad (a)$$

$$i\dot{C}_{g,1} = \frac{1}{2}\Omega e^{-i\phi_{\Omega,1}} e^{-i\delta t} e^{-i\Delta t^2} C_{e,1} \qquad (b)$$

The procedures to obtain these equations are widely available in the literature, and these equations can be obtained by using time dependent perturbation theory for a two-state quantum system driven by an external optical field [49, 50]. Here  $C_{l,i}$  is the coefficient for the excited state e or ground state g of the atom,  $\phi_{\Omega,1}$  is the phase related to the wavefront of the Raman Beam,  $\delta t$  is the phase associated with the detuning due to the Doppler effect, and  $\Delta t^2$  is the phase associated with the evolution of the atom in free

fall and frequency ramp that provides the measurement of the value of g [2]. The atoms will then experience a series of light pulses characterized as an atomic Mach-Zehnder interferometer. For the pulses, we will neglect the effect of the  $\Delta t^2$  phase since the duration of the pulses is very short compared to the duration of the time between pulses [2]. With these considerations in mind, the solutions to Eq.1.1 are

$$C_{e,1}(t) = -i\frac{\Omega}{\tilde{\Omega}}e^{i\phi_{\Omega,1}}e^{i\frac{\delta}{2}t}Sin\left(\frac{\tilde{\Omega}}{2}t\right) \qquad (a)$$

$$C_{g,1}(t) = e^{-i\frac{\delta}{2}t}\left(Cos\left(\frac{\tilde{\Omega}}{2}t\right) + i\frac{\delta}{\tilde{\Omega}}Sin\left(\frac{\tilde{\Omega}}{2}t\right)\right) \qquad (b)$$

Where  $\tilde{\Omega} = \sqrt{|\Omega|^2 + \delta^2}$ . The duration of the first pulse is equal to  $\tau_1 = \frac{\pi}{2|\Omega|}$ , now taking in consideration that  $\delta$  is small, particularly  $\frac{\delta}{|\Omega|} \ll 1$ , the coefficients for the excited and ground state after the first pulse are

$$C_{e,1}(\tau_1) = -\frac{i}{\sqrt{2}}e^{i\phi_{\Omega,1}}$$
 (a) 
$$C_{g,1}(\tau_1) = \frac{1}{\sqrt{2}}$$
 (b)

Now a dark time with a duration of  $T_1 \gg \tau_1$  happens and the atoms accumulate the respective phase so for the second pulse the equations for the two states are

$$i\dot{C}_{e,2} = \frac{1}{2}\Omega e^{i\phi_{\Omega,2}} e^{i\delta T_1} e^{i\Delta T_1^2} e^{i\delta t} C_{g,2} \qquad (a)$$

$$i\dot{C}_{g,2} = \frac{1}{2}\Omega e^{-i\phi_{\Omega,2}} e^{-i\delta T_1} e^{-i\Delta T_1^2} e^{-i\delta t} C_{e,2} \qquad (b)$$

These equations have the following solution

$$C_{e,2}(t) = e^{i\frac{\delta}{2}t} \left[ \left[ Cos\left(\frac{\tilde{\Omega}}{2}t\right) - i\frac{\delta}{\tilde{\Omega}}Sin\left(\frac{\tilde{\Omega}}{2}t\right) \right] C_{e,1}(\tau_1) - i\frac{\Omega}{\tilde{\Omega}}e^{i\phi_{\Omega,2}}e^{i\delta T_1}e^{i\Delta T_1^2}Sin\left(\frac{\tilde{\Omega}}{2}t\right) C_{g,1}(\tau_1) \right]$$
(a)
$$C_{g,2}(t) = e^{-i\frac{\delta}{2}t} \left[ \left[ Cos\left(\frac{\tilde{\Omega}}{2}t\right) + i\frac{\delta}{\tilde{\Omega}}Sin\left(\frac{\tilde{\Omega}}{2}t\right) \right] C_{g,1}(\tau_1) - i\frac{\Omega}{\tilde{\Omega}}e^{-i\phi_{\Omega,2}}e^{-i\delta T_1}e^{-i\Delta T_1^2}Sin\left(\frac{\tilde{\Omega}}{2}t\right) C_{e,1}(\tau_1) \right]$$
(b) (1.5)

The duration of the second pulse is now  $\tau_2 = \frac{\pi}{|\Omega|}$  and the coefficients for the excited and ground state after the second pulse are

$$C_{e,2}(\tau_2) = -\frac{i}{\sqrt{2}} e^{i\phi_{\Omega,2}} e^{i\delta T_1} e^{i\Delta T_1^2}$$

$$(a)$$

$$C_{g,2}(\tau_2) = -\frac{1}{2} e^{-i\delta T_1} e^{-i\Delta T_1^2} e^{i(\phi_{\Omega,1} - \phi_{\Omega,2})}$$

$$(b)$$

Now another dark time occurs and the atom accumulates phase, so the equations for the third and last pulse are

$$i\dot{C}_{e,3} = \frac{1}{2}\Omega e^{i\phi_{\Omega,3}} e^{i\delta T_2} e^{i\Delta T_2^2} e^{i\delta t} C_{g,3} \qquad (a)$$

$$i\dot{C}_{g,3} = \frac{1}{2}\Omega e^{-i\phi_{\Omega,3}} e^{-i\delta T_2} e^{-i\Delta T_2^2} e^{-i\delta t} C_{e,3} \qquad (b)$$

Whose solutions are pretty much the same as in Eq.1.5 so we will proceed to write directly the coefficient of the excited state after the third pulse which has a duration of  $\tau_3 = \frac{\pi}{2|\Omega|}$ 

$$C_{e,3}(\tau_3) = \left[ -\frac{i}{2} e^{i\delta T_1} e^{i\Delta T_1^2} e^{i\phi_{\Omega,2}} + \frac{i}{2} e^{i\delta(T_2 - T_1)} e^{i\Delta(T_2^2 - T_1^2)} e^{i(\phi_{\Omega,1} - \phi_{\Omega,2} + \phi_{\Omega,3})} \right]$$
(1.8)

And if we factor out some terms we obtain

$$C_{e,3}(\tau_3) = \frac{i}{2} \left[ -1 + e^{i\delta(T_2 - 2T_1)} e^{i\Delta(T_2^2 - 2T_1^2)} e^{i(\phi_{\Omega,1} - 2\phi_{\Omega,2} + \phi_{\Omega,3})} \right] e^{i\delta T_1} e^{i\Delta T_1^2} e^{i\phi_{\Omega,2}}$$
(1.9)

Given that  $T_2 = 2T_1$  we can appreciate that the phase due to the Doppler effect, arising from momentum components different than from the design trajectory, cancels out and we can rewrite the coefficient as

$$C_{e,3}(\tau_3) = \frac{1}{2} e^{i\phi_{Global}} \left[ -1 + e^{i\left(2\Delta T_1^2 + \phi_{\Omega,Total}\right)} \right]$$
(1.10)

Where  $\phi_{Global} = \delta T_1 + \Delta T_1^2 + \phi_{\Omega,2} + \frac{\pi}{2}$  and  $\phi_{\Omega,Total} = \phi_{\Omega,1} - 2\phi_{\Omega,2} + \phi_{\Omega,3}$ . Given that we are measuring the probability that the atom is on the excited state, the signal that we will detect is proportional to  $|C_{e,3}(\tau_3)|^2$ 

$$S(\Delta) = |C_{e,3}(\tau_3)|^2 = \frac{1}{2} \left( 1 - Cos \left( 2\Delta T_1^2 + \phi_{\Omega,Total} \right) \right)$$
 (1.11)

And here we can clearly see that the phase due to the wavefront is written directly onto the signal.

#### 1.3 The Case With No Aperture

We first examine just a pure Gaussian beam without distortions

$$E(x,y,z) = \frac{iA}{z_o} \frac{W_0}{W(z)} \hat{\varepsilon} \exp\left(-\frac{\rho^2}{W^2(z)}\right) \exp\left(ikz + \frac{ik}{2R(z)}\rho^2 - i\zeta(z)\right), \tag{1.12}$$

with A a constant proportional to the amplitude, W(z) the beam width (1/e) that depends on the axial coordinate with respect to the waist position  $(z_W)$ ,  $W_0$  the waist radius,  $\rho^2 = x^2 + y^2$ , k the magnitude of the wave vector,  $z_0$  the Rayleigh range, R(z) the radius of curvature of the wavefront,  $\hat{\varepsilon}$  the polarization and  $\zeta(z)$  the Gouy phase, with

$$W(z) = W_0 \sqrt{1 + \left(\frac{z}{z_0}\right)^2}, \quad R(z) = z \left[1 + \left(\frac{z_0}{z}\right)^2\right]$$
$$\zeta(z) = \arctan\left(\frac{z}{z_0}\right), \quad W_0 = \sqrt{\frac{2z_0}{k}}. \tag{1.13}$$

In atomic gravimetry, the Raman beams typically originate from a single mode fiber and are reflected back by a mirror to create counter-propagating beams [28]. The Rabi frequency becomes proportional to  $E_1 \times E_2^*$  [51] with  $E_1$  the field evaluated at  $z_a$ , the axial position of the atoms, and  $E_2$  evaluated at  $z_a + \Delta z$  that includes the additional distance for retro-reflection. Previous analyses have examined how changes in the amplitude and phase of Raman beams influence atomic interferometry [52, 37, 46, 36, 41, 38, 44]. These variations impact the detuning of Rabi oscillations, along with the size and phase of the Rabi frequency. As a consequence, there is a decrease in sensitivity due to diminished fringe visibility and systematic effects arising from shifts in the interference fringes. Nowadays, the distortions in the Raman beams pose a significant challenge to the precision of atomic gravimetry [39, 38, 6], and understanding these distortions is complex [53, 42, 40, 36, 41, 54]. The phase of the Rabi frequency in the Raman transition is influenced by the phase difference between the two fields ( $E_1$  and  $E_2$ ) at the desired location.

Even when dealing with a Gaussian beam that has no distortions (Eq. 1.12), there is still a phase shift in the gravimetric measurement. Imagine an atomic cloud where all the atoms are aligned along the axis ( $\rho_1 = \sqrt{x^2 + y^2} = 0$ ), and the beam waist is sufficiently large that we can ignore any variations in amplitude.

In the duration of the free fall time (T) within the gravimetric sequence, an atom possessing a transverse velocity v experiences displacements of  $\rho_2 = vT$  and  $\rho_3 = 2vT$  at the second and third interferometric pulses, respectively, in a  $\pi/2$ - $\pi$ - $\pi/2$  Mach Zehnder interferometric sequence. If we consider the pulses to be extremely brief, the resulting phase shift of the interference fringes can be described by the following expression [38, 46].

$$\phi = \theta_1 - 2\theta_2 + \theta_3,\tag{1.14}$$

with  $\theta_i = \alpha \rho_i^2(v)$  the phase of the Rabi frequency at pulse i, and

$$\alpha = \frac{k}{2} \left( \frac{1}{R(z_a)} - \frac{1}{R(z_a + \Delta z)} \right). \tag{1.15}$$

The atomic cloud at temperature  $T_b$  exhibits a velocity distribution characterized by a width of  $\sigma_v = \sqrt{k_B T_b/m}$ . By averaging all the atoms and assuming perfect visibility, the resulting interference patterns are

$$S = \int_{-\infty}^{\infty} P(v) \frac{1}{2} \left( 1 - \cos[\Phi + \phi(v)] \right) dv, \tag{1.16}$$

where  $\Phi$  is the gravitational phase including the frequency sweep [6]. For small phase shifts, we can keep only terms linear in  $\phi$  so that

$$\cos[\Phi + \phi] = \cos(\Phi)\cos(\phi) - \sin(\Phi)\sin(\phi) \simeq \cos(\Phi) - \phi\sin(\Phi), \tag{1.17}$$

then

$$S \simeq \int_{-\infty}^{\infty} P(v) \frac{1}{2} \left( 1 - (\cos \left[ \Phi \right] - \phi(v) \sin \left[ \Phi \right] \right) \right) dv$$
$$= \frac{1}{2} \left( 1 - (\cos \left[ \Phi \right] - \langle \phi \rangle \sin \left[ \Phi \right] \right) \right) \simeq \frac{1}{2} \left( 1 - \cos \left[ \Phi + \langle \phi \rangle \right] \right), \tag{1.18}$$

this means that when you average the fringe signals from all the atoms, the result creates a shift that is roughly equal to the average fringe shifts of the individual atoms.

Assuming  $\theta_i = \alpha_n \rho^{2n}$  in Eq. 1.14, the average shift gives

$$\langle \phi \rangle = \alpha_n (2^{3n} - 2^{n+1}) T^{2n} \sigma_v^{2n} n!,$$
 (1.19)

where we write the shift in terms of the velocity width. The shift depends on the temperature as  $T_b^n$ , which in particular is linear for n=1 [42, 46]. To quickly approximate the shift caused by the curvature of the wavefront, one can use a polynomial expansion in terms of  $\rho^2$  along with Eq.1.19. The wavefront of the Gaussian beam (Eq. 1.12) has a quadratic transverse dependence (n=1). The amount of correction varies based on the locations of the atoms in relation to the waist and the distance of retro-reflection, and it can be determined through calculations, taking  $\alpha_n = \alpha$  from Eq. 1.15 [46]. Taking for example in Eq. 1.19 rubidium atoms at  $T_b = 1$   $\mu$ K and a beam with  $z_a = 0$ ,  $W_0 = 1.5$  cm,  $\Delta z = 1$  m and T = 0.1 s gives a  $\langle \phi \rangle = -2 \times 10^{-5}$  rad.

#### 1.4 Far Field Diffraction

Introducing an aperture alters the wavefront of the Gaussian beam, leading to changes in the transverse amplitude and phase profile (we will disregard polarization from this point onward). The variations in phase are particularly significant because they directly translate into a shift in the interferometer phase (as indicated in Eq. 1.14), so we will concentrate on these first. It is instructive to analyze the far field case first. In the Fraunhofer diffraction, the field at a distant screen is obtained from

$$E(x, y, z) = \left(\frac{-ik}{2\pi z}\right) \exp\left(ikz + \frac{ik}{2z}\rho^2\right) \times$$

$$\times \int_{-\infty}^{\infty} \int_{-\infty}^{\infty} E'(x', y', 0)p(x', y') \exp\left(-i\frac{k}{z}(xx' + yy')\right) dx' dy',$$
(1.20)

where E'(x', y', z') is the electric field right at the aperture and p(x', y') is the aperture function.

We concentrate on circular apertures with a radius of a and square apertures with a side length of 2a, both of which restrict light outside the aperture situated at z' = 0. By illuminating the aperture with a Gaussian beam (Eq. 1.12) that has its waist at  $z' = -z_W$ , we derive a result for the square aperture.

$$E(x, y, z) = \left(\frac{Ak}{2\pi z z_0}\right) \frac{W_0}{W(-z_W)} \exp\left(ik(z - z_W) + \frac{ik}{2z}\rho^2 - i\zeta(-z_W)\right) \times \frac{\pi}{Q(-z_W)} \exp\left(-\frac{k^2}{4z^2Q(-z_W)}\rho^2\right) f_E(x) f_E(y), \tag{1.21}$$

with

$$f_E(x) = \frac{1}{2} \operatorname{erf} \left[ a \sqrt{Q(-z_W)} + i \frac{kx}{2z} \frac{1}{\sqrt{Q(-z_W)}} \right] - \frac{1}{2} \operatorname{erf} \left[ -a \sqrt{Q(-z_W)} + i \frac{kx}{2z} \frac{1}{\sqrt{Q(-z_W)}} \right], \quad (1.22)$$

and similarly for  $f_E(y)$ , and with

$$Q(z) = \frac{1}{W^2(-z_W)} - i\frac{k}{2R(-z_W)}. (1.23)$$

The methods used to achieve the earlier results are explained in Appendix A. Next, for a circular opening, we have

$$E(\rho, z) = \left(\frac{-ik}{2\pi z}\right) \exp\left(ikz + \frac{ik}{2z}\rho^2\right) 2\pi \int_0^\infty E'(\rho', 0)p(\rho')J_0\left(\frac{k\rho\rho'}{z}\right)d\rho',\tag{1.24}$$

with  $J_0$  the zero order Bessel function. The equation can be written as an expansion in Bessel functions  $(J_n)$  [55]

$$E(\rho, z) = \left(\frac{Ak}{2\pi z z_0}\right) \frac{W_0}{W(-z_W)} \exp\left(ik(z - z_W) + i\frac{k\rho^2}{2z} - i\zeta(-z_W)\right) \times \frac{\pi}{Q(-z_W)} \left(\exp\left(-\frac{k^2\rho^2}{4z^2Q(-z_W)}\right)\right) - e^{-Q(-z_W)a^2} \sum_{n=0}^{\infty} \left(-\frac{k\rho}{2zaQ(-z_W)}\right)^n J_n\left(\frac{k\rho a}{z}\right)\right). \quad (1.25)$$

Equation 1.19 illustrates that the phase shift of the interferometric fringes can be determined if the value of  $\alpha_n$  is known, which can be derived from a Taylor expansion in the transverse variable  $\rho$  of the previously mentioned equations for the electric field (Eqs. 1.21 and 1.25).

In the case of a square aperture (Eq. 1.21), there are three factors that influence the transverse phase dependence.

$$\Psi_T = \frac{k}{2z} \rho^2 \left( 1 - \frac{k}{2z} \operatorname{Im} \left[ \frac{1}{Q(-z_W)} \right] \right) + \Xi_E, \tag{1.26}$$

with  $\Xi_E$  any contributions coming from  $f_E(x)f_E(y)$  (Eq. 1.22).

The effect of the aperture depends on its size compared to the width of the beam and the curvature of the beam's wavefront where the aperture is located.

We will begin by examining the scenario that features a beam characterized by a flat wavefront, that is, with  $|z_W| \ll z_0$ . When the aperture is significantly larger than the beam size  $(a \gg W_0)$ , it behaves much like there is no aperture at all.

In Appendix B, it is demonstrated that only the initial term in Equation 1.26 has a significant contribution ( $\Psi_T = (k/2z)\rho^2$ ). Consequently, the curvature of the beam on a distant screen mirrors that of a Gaussian beam alone, as expressed in Equation 1.12. As stated in Equation 1.13, the radius of curvature of the wavefront at considerable distances

is determined by the distance from the beam waist to the screen, which in this scenario is approximately z, given that the waist is situated very near to the aperture.

The same outcome persists as the aperture size decreases, as in this scenario  $f_E(x)$  and  $f_E(y)$  are real numbers (Eq. B.3 of Appendix B) and  $\Xi_E = 0$ . Consequently, the curvature of the wavefront corresponds solely to that of a spherical wave emanating from the aperture.

The alternative limit involves examining a waist that is significantly distant from the aperture, specifically when  $|z_W| \gg z_0$  (but still with  $|z_W| \ll z$  to be in the far field). In cases where the aperture is large  $(a \gg W(-z_W))$ , it exerts no influence, resulting in  $\Xi_E = 0$ . Consequently, the contributions from the remaining two terms in Eq. 1.26 yield the following (refer to Appendix B)

$$\Psi_T = \frac{k}{2z} \rho^2 \left( 1 + \frac{z_W}{z} \right) \simeq \frac{k}{2(z - z_W)} \rho^2,$$
(1.27)

This relates to a radius of curvature  $R = z - z_W$ , which indicates the distance from the waist to the screen, as would be anticipated when there is no aperture. When the aperture size is decreased, it adds a term from  $\Xi_E \simeq \frac{kz_W}{2z^2}\rho^2$ , resulting in the overall transverse phase described in Appendix B,

$$\Psi_T \simeq \frac{k}{2z}\rho^2 - \frac{kz_W}{2z^2}\rho^2 + \frac{kz_W}{2z^2}\rho^2 = \frac{k}{2z}\rho^2,$$
(1.28)

In other words, when the aperture is quite small, it produces nearly uniform illumination and acts as the source of a spherical wave in the far field. Here, the radius of curvature of the wavefront (R = z) is determined by the distance from the aperture to the screen, regardless of the beam waist's location. In this final scenario, the aperture alters the curvature of the wavefront in the far field from  $R = z - z_W$  to R = z. This adjustment leads to a minor change in the value of  $\alpha$  (refer to Eq. 1.15), which subsequently affects the phase shift of the interferometric fringes (see Eq. 1.19).

#### 1.5 Near Field Diffraction

The previous chapter provided us with some understanding of how an aperture influences the far field, but the majority of interferometry experiments utilize beams in the near field. In fact, for interferometry, it is preferable to have a highly collimated beam with a large waist in order to achieve consistent illumination of the atomic cloud [46, 44, 37].

The diffraction in the near field is described by [56]

$$E(x,y,z) = \left(\frac{-ik}{2\pi z}\right) e^{ikz} \times$$

$$\times \int_{-\infty}^{\infty} \int_{-\infty}^{\infty} E'(x',y',0)p(x',y') \exp\left(i\frac{k}{2z}((x-x')^2 + (y-y')^2)\right) dx'dy'. \quad (1.29)$$

In the case of a square aperture we obtain the same as Eq. 1.21 but with

$$Q(-z_W) = \frac{1}{W^2(-z_W)} - i\frac{k}{2R(-z_W)} - i\frac{k}{2z}$$

$$= \frac{1}{W^2(-z_W)} - i\frac{k}{2R'}$$
(1.30)

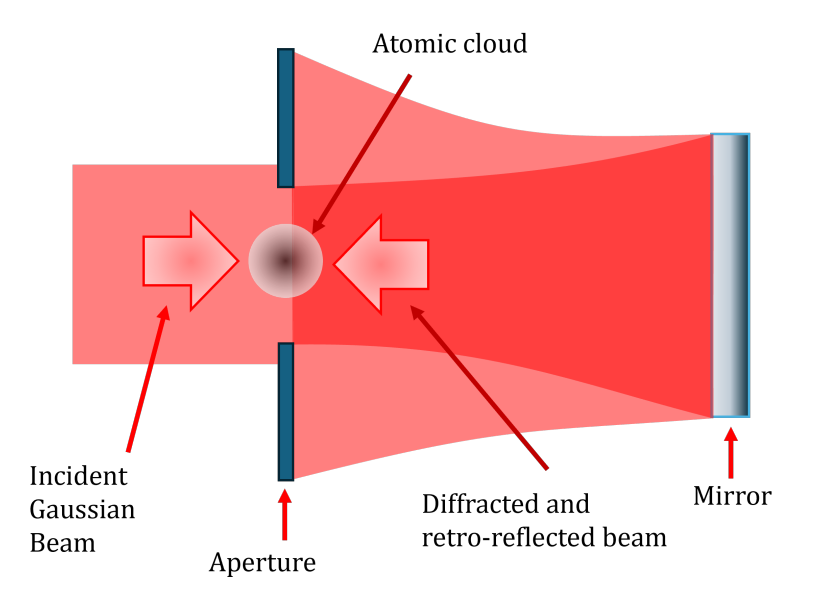


Figure 1.1: The depiction of the experimental configuration in the numerical simulation illustrates the Raman beam, the atomic cloud, and the aperture. The Raman beam consists of a non-diffracted Gaussian beam alongside a diffracted and retro-reflected Gaussian beam, with the atomic cloud interacting with both beams.

where for the last expression we define  $R' = R(-z_W)z/(R(-z_W)+z)$ . Typically  $R(-z_W) \gg z$  so that  $R' \simeq z$ . For the circular aperture we obtain the same result as Eq. 1.25 with  $Q(-z_W)$  given by Eq. 1.30.

We investigate how beam diffraction influences the interference fringes. We continue to assume that the pulses are extremely short, allowing us to describe the phase shift using Eq. 1.14. As the atomic cloud expands, each atom interacts with the Raman pairs, experiencing a phase change due to diffraction. This altered phase is reflected in the Rabi frequency at each pulse and position. The overall signal represents the average of the signals of all atoms within the expanding atomic cloud.

We carry out a Monte Carlo average on atoms that have randomly assigned positions and velocities [46]. The sample follows a two-dimensional (x, y) Gaussian distribution for the positions, centered at the origin with a width of  $\sigma_A$ . We omit the axial position (z) as diffraction effects are minimal in that direction within a distance of  $\sigma_A$ .

Additionally, there is a Gaussian distribution of transverse velocities  $(v_x, v_y)$  that is centered around zero, with a width  $\sigma_v$  that varies based on the temperature. We determine the phase of the diffracted beam for each atom during each pulse in order to ascertain the phase of the Rabi frequency associated with the Raman transition, which subsequently allows us to calculate the shift in the interference fringes for that particular atom.

We calculate the average signal of all the atoms and adjust the resulting interference patterns to find their displacement. For minor shifts, this method yields results comparable to averaging the shifts of each individual atom, as demonstrated in Eq. 1.18.

The diffracted beam exhibits changes in both amplitude and phase across its width. To comprehend how these variations influence the interference patterns, we will examine them individually. Phase changes are directly transformed into shifts in the fringes (see Eq. 1.14), so we will first evaluate their impact, overlooking the changes in intensity.

We incorporate the phase  $(\phi_{\Omega})$  of the diffracted beam (see Eq. 1.29) into the Rabi

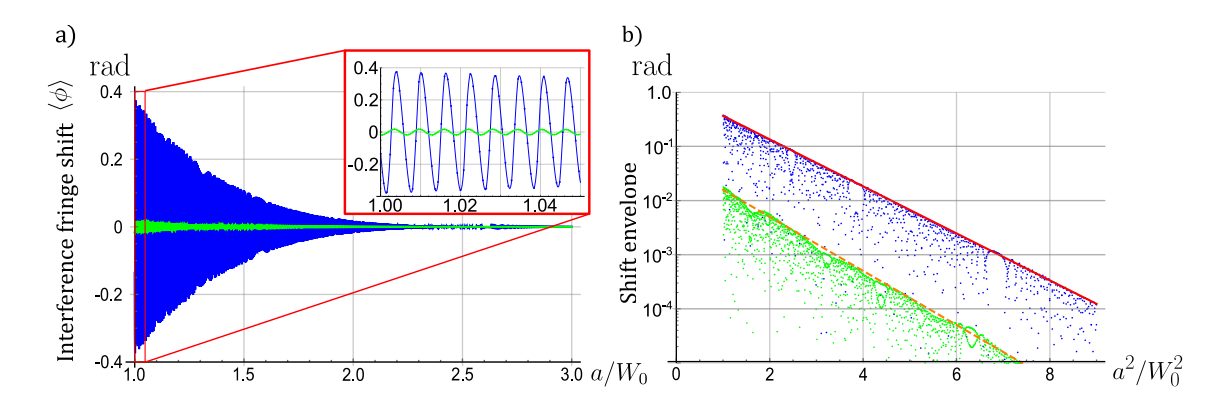


Figure 1.2: The phase shift is examined as a function of the aperture size (a) normalized to the beam waist  $(W_0)$ . In this case, z=2 m,  $W_0=1.5$  cm, and  $\lambda=780$  nm, with all atoms initially located at the origin, displaying a "transverse" temperature of  $T_b=1$   $\mu \rm K$  and a duration of T=20 ms. a) The findings are shown for a circular aperture (in blue) and a square aperture (in green). The inset offers a zoomed-in view to highlight the oscillations. b) The raw data and the envelope of the phase shift for the circular aperture (blue) follow the function  $e^{-a^2/W_0^2}$  (indicated by the solid red line, see Eq. 1.32), while the square aperture (green) aligns with a similar function  $(1/20)e^{-1.15a^2/W_0^2}$  (represented by the dashed orange line).

frequency, while keeping the magnitude of the Rabi frequency  $(\Omega_0)$  uniform across the entire atomic cloud (thus,  $\Omega = \Omega_0 e^{i\phi_{\Omega}}$ ). We'll address the intensity dependence at a later time.

We consider the aperture to be located directly at the atoms' position, ensuring that the input beam is an ideal Gaussian beam (as described in Equation 1.12). In contrast, the retro-reflected beam is subjected to diffraction and has traveled a distance (z) on its return path to the atoms, as depicted in Figure 1.1.

Initially, we examine the scenario of a highly restricted velocity distribution in the axial  $(v_z)$  direction, which would occur when employing the suitable selection pulse [46]. This allows us to concentrate on the influence of the beam's transverse profile, effectively assuming that there is no Doppler shift at this stage.

Figure 1.2a illustrates the phase shift of the interference fringes in relation to the aperture size, normalized to the Raman beam waist. Notably, a significant phase shift occurs for apertures that are comparable in size to the beam waist. Furthermore, this phase shift exhibits a sensitive oscillation with changes in aperture size, as depicted in the inset, complicating the prediction of the anticipated phase shift in specific experimental configurations.

Fortunately, larger apertures lead to a reduction in phase shift, allowing for the establishment of limits on the necessary correction. The envelope of the phase shift exhibits a Gaussian relationship with the size of the aperture (Figure 1.2b), as we will demonstrate in the following calculations.

The phase shift observed in the interference fringes is attributed to the diffraction occurring at the aperture. In Figure 1.3, the transverse variation of the phase of the diffracted beam is illustrated, as described by Eqs. 1.25 and 1.30, for a circular aperture. The plot reveals a prominent peak at the center, accompanied by radial oscillations.

The central peak plays a crucial role in the displacement of the interference fringes. In the simulation, we initialize all atoms at the origin ( $\sigma_A = 0$ ), ensuring that during the first pulse, every atom experiences the phase shift associated with the central feature.

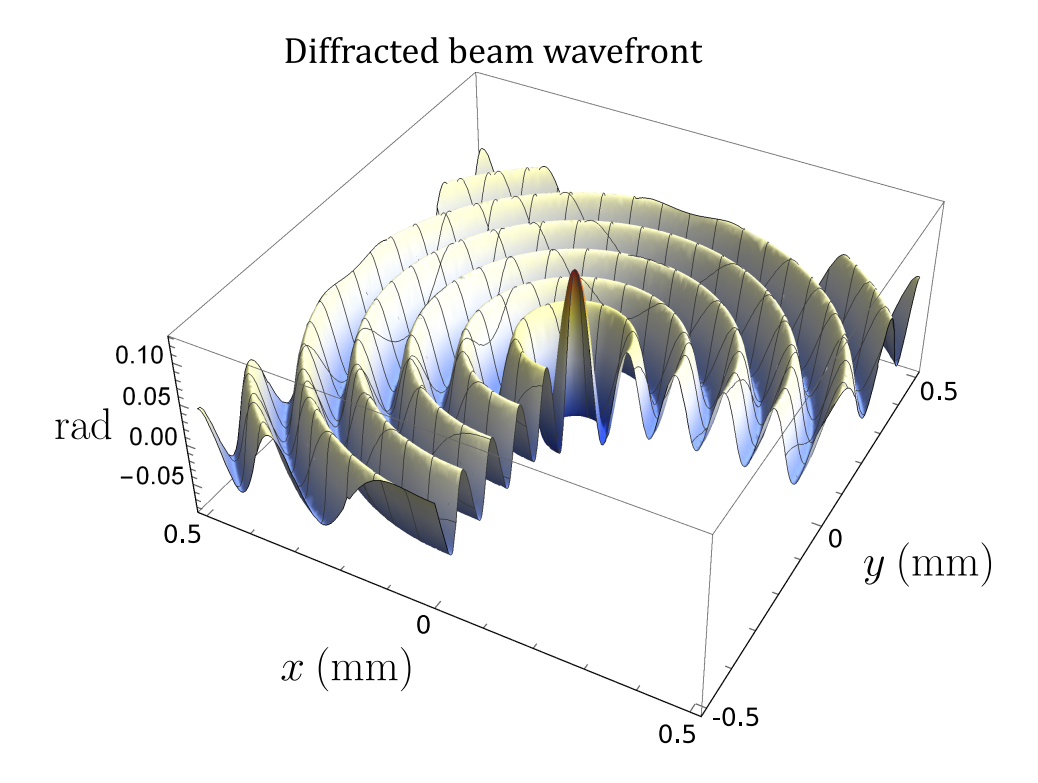


Figure 1.3: The transverse phase of the beam that has been diffracted through a circular aperture is described by Equations 1.25 and 1.30. In our analysis, we set the parameters as follows:  $z_0 = 10^3$  m,  $\lambda = 780$  nm,  $z_W = 0$ , z = 2 m, and  $a = W_0 \simeq 1.5$  cm. For the sake of clarity in visualization, a phase offset of  $-\pi/2$  was incorporated into the plot.

During the second and third pulses, the atomic cloud experiences an increase in size, causing the atoms to interact with the oscillating phase, which results in a significantly reduced contribution. Consequently, the first pulse is responsible for the shift. In fact, if we exclude the diffraction effects from the second and third pulses in our calculations while retaining them for the first pulse, the outcome remains largely unchanged (Fig. 1.4).

To evaluate the fringe shift, we examine the electric field along the axis directly (Eq. 1.24 with  $\rho = 0$  and Q given by Eq. 1.30), and we get

$$E(\rho = 0, z) = \left(\frac{AkW_0}{zz_0W(-z_W)}\right) J_0(0) \exp\left[ik(z - z_W) - i\zeta(-z_W)\right] \int_0^a e^{-Q(-z_W)\rho'^2} \rho' d\rho'$$

$$= \left(\frac{AkW_0}{zz_0W(-z_W)}\right) J_0(0) \exp\left[ik(z - z_W) - i\zeta(-z_W)\right] \frac{1 - e^{-Q(-z_W)a^2}}{2Q(-z_W)} (1.31)$$

Our focus lies in examining how the phase of the field is influenced by the aperture size a, as described by the subsequent expression.

$$\Psi_{a} = \operatorname{Arg}\left(1 - e^{-Qa^{2}}\right) = \operatorname{ArcTan}\left[-e^{-a^{2}/W^{2}(-z_{W})} \frac{\sin\left(ka^{2}/2R'(-z_{W})\right)}{1 - e^{-a^{2}/W^{2}(-z_{W})}\cos\left(ka^{2}/2R'(-z_{W})\right)}\right] \\
\simeq -e^{-a^{2}/W^{2}(-z_{W})} \frac{\sin\left(ka^{2}/2R'\right)}{1 - e^{-a^{2}/W^{2}(-z_{W})}\cos\left(ka^{2}/2R'(-z_{W})\right)}, \quad (1.32)$$

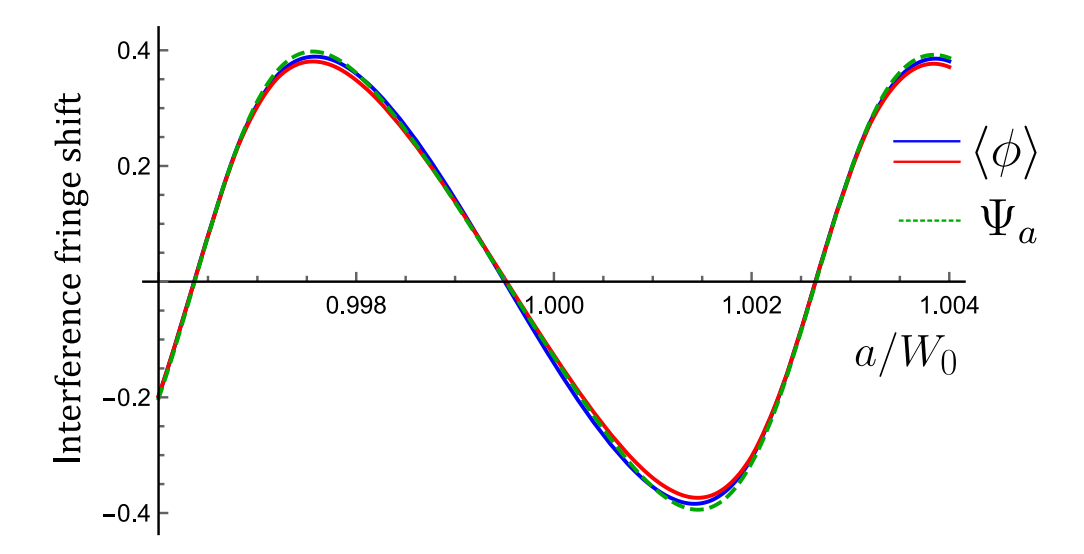


Figure 1.4: The phase shift of the interference fringes is analyzed as a function of the aperture size, incorporating the diffraction effect across all pulses (represented in blue) or solely on the initial pulse (depicted in red). The oscillations correspond to the phase shift of the diffracted beam's field (as indicated in Eq. 1.32, shown in green dashed lines). The parameters utilized include z=2 m,  $z_W=0$  m,  $z_0=10^3$  m,  $\lambda=780$  nm, and  $\sigma_A=10^{-7}$  m.

where we have used  $ArcTan[x] \simeq x$  for small x.

Figure 1.4 illustrates that Eq. 1.32 accounts for the phase shift detected in the interference fringes. The envelope of these shifts is influenced by the amount of light obstructed by the aperture and adheres to the Gaussian distribution characteristic of transverse beams. An integer count of oscillations is achieved when the argument of the trigonometric function equals  $2\pi n$ , where n is an integer. The aperture values

$$a_n = \sqrt{4\pi nR'/k} \simeq \sqrt{2n\lambda z},\tag{1.33}$$

fulfil such condition and correspond to the Fresnel Zones [57].

The first pulse largely influences the phase shift since the cloud is significantly smaller than the central peak illustrated in Fig. 1.3. To illustrate this, we computed the amplitude of the oscillations in the phase shift based on the initial atomic cloud width,  $\sigma_A$ , as shown in Fig. 1.5.

The envelope of the phase shift remains the same until the width of the atomic cloud is similar to the width of the central feature shown in Fig. 1.3. Beyond that point, the atoms obtain various phase values that average to create a diminished effect. This acts like a low-pass filter, with a cutoff frequency determined by the width of the central feature in the diffracted phase front.

The width is derived from Equation 1.25, with Q provided by Equation 1.30. For a small radial distance ( $\rho \ll 2z/kW_0$ ), the exponential in Equation 1.25 can be approximated to 1, allowing us to retain only the first term in the sum to achieve

$$E(\rho, z) \simeq \left(\frac{Ak}{2\pi z z_0}\right) \frac{W_0}{W(-z_W)} \exp\left(ik(z - z_W) + \frac{ik}{2z}\rho^2 - i\zeta(-z_W)\right) \times \left(1.34\right)$$

$$\times \frac{1}{2Q} \left[1 - J_0\left(\frac{k\rho a}{z}\right)e^{-Qa^2}\right].$$

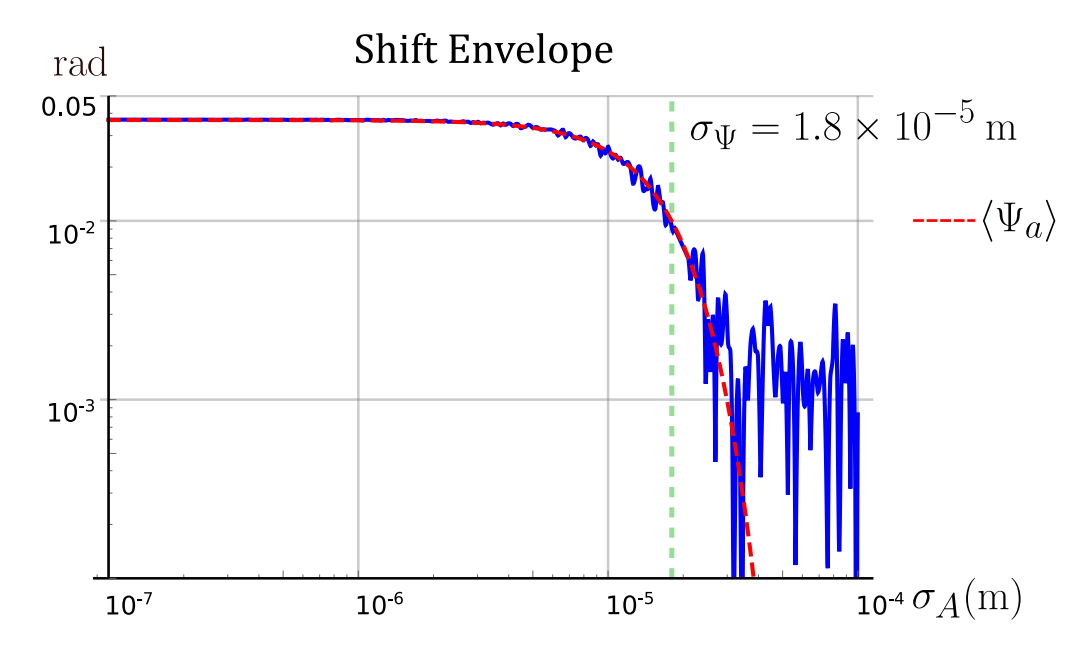


Figure 1.5: The envelope of the oscillations in the phase shift of the interference fringes is illustrated as a function of the initial width  $(\sigma_A)$  of the atomic cloud (shown in blue). This behavior is explained by Equation 1.38 (represented by the dashed red line). The effect significantly decreases when the cloud size surpasses the cutoff value  $\sigma_{\Psi}$  (marked by the vertical line, Equation 1.36). The parameters used in this analysis include  $z_0 = 1000$  m,  $\lambda = 780$  nm, z = 2 m,  $W_0 = 1.5$  cm,  $a \simeq 2W_0$ ,  $T_b = 1\mu K$ , T = 20 ms, and  $\Omega_0 = 2\pi \times 10^3$  rad/s.

The dependence of the phase on the aperture values (for a small angle) is expressed as follows

$$\Psi_{a} = \operatorname{Arg}\left[1 - J_{0}\left(\frac{k\rho a}{z}\right)e^{-Qa^{2}}\right] \simeq -e^{-a^{2}/W^{2}(-z_{W})} \frac{J_{0}\left(k\rho a/z\right)\sin\left(ka^{2}/2R'(-z_{W})\right)}{1 - e^{-a^{2}/W^{2}(-z_{W})}J_{0}\left(k\rho a/z\right)\cos\left(ka^{2}/2R'(-z_{W})\right)}.$$
(1.35)

If  $a > W^2(-z_W)$ , the radial dependence is primarily captured in  $J_0(k\rho a/z)$ , and the width of the central feature is roughly at the point where the argument of the zero-order Bessel function equals zero  $(j_{0,1} = 2.4)$ , which means that

$$\sigma_{\Psi} = \frac{j_{0,1}z}{ka}.\tag{1.36}$$

This value genuinely aligns with the cloud size at which averaging begins to occur, resulting in a significant reduction in the amplitude of the phase shift oscillations (see Fig. 1.5).

A basic estimation summarizes the core idea of phase averaging across the sample. Previously, we demonstrated that the overall average shift of the fringes among all the atoms can be approximated by the average of the individual shifts (Eq. 1.18). We calculate the average phase, as described in Eq. 1.35, over the Gaussian atomic cloud.

We consider the scenario where  $a > W(-z_W)$  to facilitate the simplification of the integral by setting the denominator to 1, resulting in an average shift of

$$\langle \Psi_a \rangle \simeq \int_0^{2\pi} \int_0^{\infty} \frac{1}{2\pi\sigma_A^2} e^{-\rho^2/2\sigma_A^2} e^{-a^2/W^2(-z_W)} J_0\left(\frac{k\rho a}{z}\right) \sin\left(\frac{ka^2}{2R'(-z_W)}\right) \rho d\rho d\theta. \tag{1.37}$$

By employing a summation analogous to that utilized in [55], we derive

$$\langle \Psi_a \rangle \simeq e^{-a^2/W^2(-z_W)} \sin\left(\frac{ka^2}{2R'(-z_W)}\right) \exp\left(-\frac{j_{0,1}^2}{2} \left[\frac{\sigma_A}{\sigma_\Psi}\right]^2\right).$$
 (1.38)

The analytical expression represented by the red dashed line in Fig. 1.5 illustrates the decrease in the phase shift of the fringes resulting from the averaging effect of the atoms within an extended cloud. This phenomenon accounts for the predominance of the first pulse's influence, as the size of the cloud significantly increases for the later pulses in the gravimetric sequence due to thermal expansion.

When the value of  $\sigma_A$  is significantly large, a residual effect arises due to the incomplete cancellation of the contributions from the wave front ripples during the averaging process. This effect is approximately two orders of magnitude smaller compared to that observed with a small cloud.

The relationship between  $\sigma_{\Psi}$  (Eq. 1.36) and the experimental parameters can be explained by examining the field generated by a ring of emitters at the location of the aperture.

The distance to an axial point P is equivalent to the distance the diffracted beam covers during retro-reflection (z). Since all the points on the ring travel the same distance, they all contribute to the electric field at point P in phase.

As we expand the radius of the ring, the phase of the field produced at point P varies similarly to the Fresnel Zones (as described in Eq. 1.33). A lens with a radius of a that forms an image at a distance z (where the numerical aperture is approximately  $NA \simeq a/z$ ) would achieve a certain resolution [57]

$$r = \frac{0.61\lambda}{NA} \simeq 2\pi (0.61) \frac{z}{ka},$$
 (1.39)

that has an equivalent dependence as the width of the central diffraction feature (Eq. 1.36).

When the emitters are arranged in a square configuration, as would occur with a square aperture, their contributions to the field at point P will not be synchronized in phase as is illustrated in Figure 1.6.

This elucidates the reason for the more pronounced phase shift of the interference fringes observed with a circular aperture in comparison to a square aperture (Fig. 1.2).

By selecting values of a=2 cm, z=50 cm, and  $\lambda=780$  nm, one finds that  $\sigma_{\Psi}\approx7$   $\mu$ m, this value is less than the usual dimensions of atomic clouds, resulting in a significant reduction in the shift of the interference fringes due to the averaging effect. Furthermore, decreasing the distance from the aperture to the atoms (z) enhances the averaging process and diminishes the shift.

The earlier findings were derived solely by taking into account the phase of wavefront aberrations. An aperture of adequate dimensions contributes insignificantly to the fluctuations in fringe contrast. When employing apertures with a size a greater than the beam waist W, which is anticipated in atomic interferometry, a minor intensity modulation is observed superimposed on the Gaussian beam as a result of the aperture's presence.

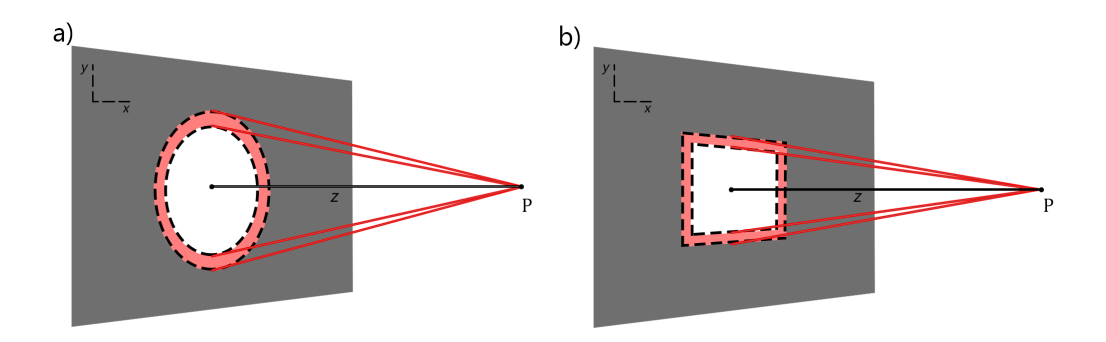


Figure 1.6: A ring of emitters is positioned at the aperture for a) a circular aperture in contrast to b) a square aperture. The point P is located on the axis at a distance z from the aperture.

The inclusion of this intensity modulation results in a minimal alteration to the previously mentioned outcomes. Prior analyses have examined the impact of the axial velocity distribution [46, 54], and incorporating these factors into the Monte Carlo simulations yields an insignificant effect on the aperture phenomena discussed earlier. Additionally, the low average velocity of the atomic cloud contributes negligibly. Consequently, the primary influence arises from the phase variations in the beams caused by the aperture.

The maximum shift occurs at the origin; however, in practical experimental scenarios that generate atomic clouds with minor discrepancies in their initial positions, a reduction will be observed due to the averaging of the associated phase shift (as indicated in Eq. 1.35 when evaluated with  $\rho \neq 0$ ).

#### 1.6 Photon Recoil Correction

In the preceding chapters, we have demonstrated that the aperture causes aberrations in the beams, resulting in a shift in the measured interferometric phase. Additionally, there exists a lesser-known correction that warrants consideration, which pertains to a modification of the momentum transferred in relation to  $\hbar k$ . By expressing the axial momentum transfer as  $p_z = \hbar k (1 + [\delta k/k])$ , the fractional photon recoil correction can be articulated as follows [58]

$$\frac{\delta k}{k} = -\frac{1}{2} \left| \frac{\nabla_T \Psi}{k} \right|^2 + \frac{1}{2k^2} \frac{\nabla_T^2 A_E}{A_E},\tag{1.40}$$

with  $\Psi$  and  $A_E$  the phase and magnitude of the electric field of the beam, and  $\nabla_T$  acting only on the transverse variables.

The initial term of Eq. 1.40 is quite recognizable, as a transverse gradient in the phase corresponds to the presence of transverse momentum components  $(p_x \text{ and } p_y)$  that would diminish the axial  $(p_z)$  component to maintain a constant momentum magnitude. One might assume that this correction has already been accounted for in the discussions of earlier chapters, which focus on transverse phase variations. However, this assumption is incorrect, as demonstrated by examining a beam exhibiting identical curvature at both the input and during retro-reflection. In this scenario, the prior analysis indicates that there is no phase shift in the interferometric fringes whatsoever; nevertheless, both beams experience a reduction in axial momentum transfer by the same amount, which does not result in cancellation.

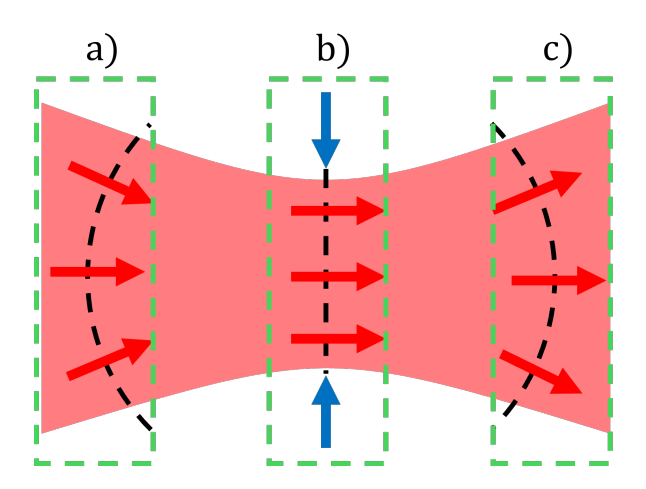


Figure 1.7: The depiction of a Gaussian beam emphasizes three regions where the propagation vector exhibits a transverse component. The red arrows indicate the direction of the propagation vector, while the black dashed lines illustrate the curvature of the wavefront. In zones a) and c), the transverse component of the propagation vector can be intuitively inferred from the curvature of the wavefront. Conversely, in zone b), the emergence of the transverse component of the propagation vector is attributed to the enhanced spatial confinement of the beam, as this region corresponds to the beam's waist.

The second term in Equation 1.40 is less familiar and pertains to fluctuations in intensity; it has been associated, for instance, with phenomena such as the Gouy phase [59]. This term contributes significantly to the photon recoil correction, as demonstrated in the following sections. In the absence of an aperture, the Gaussian beam described in Equation 1.12 results in a correction of

$$\frac{\delta k}{k} = -\frac{1}{2} \left| \frac{\rho}{R(z - z_W)} \right|^2 + \frac{2}{k^2} \left( \frac{\rho^2}{W^4(z - z_W)} - \frac{1}{W^2(z - z_W)} \right). \tag{1.41}$$

It is important to recognize that a correction exists even when the beam exhibits a plane wavefront, due to its transverse intensity profile, this previous statement is illustrated in Figure 1.7.

The aperture introduces further variations in both the phase and intensity, which are significant to Eq. 1.40. When examining a large aperture  $(a > W_0)$  and small distances from the beam axis  $(\rho < 2z/kW_0)$ , we retain only the first term in Eq. 1.25 to derive

$$E(\rho, z) = \frac{kA}{2zz_0Q} \exp\left(ik(z - z_W) + i\frac{k\rho^2}{2z} - i\zeta(-z_W)\right) *$$

$$* \left(\exp\left(-\frac{k^2\rho^2}{2^2z^2Q}\right) - \exp\left(-Qa^2\right)J_0\left(\frac{k\rho a}{z}\right)\right).$$
(1.42)

We are considering the case when  $z_0 \gg z$  and  $z_0 \gg |z_W|$ , then  $Q \simeq 1/W_0^2 - ik/2z$ , and the term in the exponent becomes

$$-\frac{k^2\rho^2}{2^2z^2Q} = -\frac{z_0^2}{z^2+z_0^2}\frac{\rho^2}{W_0^2} - i\frac{z_0^2}{z^2+z_0^2}\frac{k\rho^2}{2z},$$

and the electric field of Eq. 1.42 gives

$$E(\rho, z) = \frac{kA}{2zz_0Q} \exp\left(ik(z - z_W) + i\frac{k\rho^2}{2R(z)} - i\zeta(-z_W)\right) *$$

$$* \left(\exp\left(-\frac{\rho^2}{W(z)^2}\right) - \exp\left(-Qa^2 + i\beta\frac{k\rho^2}{2z}\right)J_0\left(\frac{k\rho a}{z}\right)\right).$$
(1.43)

The amplitude of the field (for  $\rho < 2z/ka$ ) is

$$A_E \simeq \frac{kA}{2zz_0|Q|} \left( \exp\left(-\frac{\rho^2}{W(z)^2}\right) - \exp\left(-\frac{a^2}{W_0^2}\right) \cos\left(\frac{ka^2}{2z}\right) J_0\left(\frac{k\rho a}{z}\right) \right), \tag{1.44}$$

and the phase

$$\Psi \simeq k(z - z_W) + \frac{k\rho^2}{2R(z)} - \zeta(z_W) - \exp\left(-\frac{a^2}{W_0^2}\right) \sin\left(\frac{ka^2}{2z}\right) J_0\left(\frac{k\rho a}{z}\right) + \arctan\left(-\frac{kW_0^2}{2z}\right). \quad (1.45)$$

The Laplacian for the amplitude dependent term of Eq. 1.40 gives

$$\nabla_T^2 A_E = \frac{kA}{2zz_0|Q|} \exp\left(-\frac{\rho^2}{W(z)^2}\right) \left[\frac{4\rho^2}{W(z)^4} - \frac{4}{W(z)^2}\right] + \frac{kA}{2zz_0|Q|} \left(\frac{ka}{z}\right) \exp\left(-\frac{a^2}{W_0^2}\right) \cos\left(\frac{ka^2}{2z}\right) * \left[J_1\left(\frac{k\rho a}{z}\right)/\rho + \frac{ka}{2z}\left(J_0\left(\frac{k\rho a}{z}\right) - J_2\left(\frac{k\rho a}{z}\right)\right)\right], \quad (1.46)$$

and the gradient for the phase dependent term

$$\frac{\nabla_T \Psi}{k} = \frac{\rho}{R(z)} + \left(\frac{a}{z}\right) \exp\left(-\frac{a^2}{W_0^2}\right) \sin\left(\frac{ka^2}{2z}\right) J_1\left(\frac{k\rho a}{z}\right). \tag{1.47}$$

The same Monte Carlo method employed previously is utilized to compute the photon recoil correction (Eq. 1.40) across an atomic cloud, varying with the size of the aperture (Fig. 1.8). Given that the gravitational phase exhibits a linear dependence on both g and  $k_z$ , the fractional adjustment in the measured value of g is expressed as  $\delta k/k$ .

The influence of the phase gradient (represented in blue in Fig. 1.8) is less significant than that of the amplitude (depicted in red) [58]. The corrections exhibit rapid oscillations in relation to the aperture size (as shown in Eqs. 1.46 and 1.47), akin to the observations made in earlier chapters. Therefore, our focus is on determining the envelope of these oscillations to establish a limit on their contributions. The derived envelope for the phase gradient contribution (as per Eq. 1.47) yields

$$\frac{1}{2} \left| \frac{\nabla_T \Psi}{k} \right|^2 \le \frac{1}{2} \left| \frac{\sigma_A}{R(z)} + \left( \frac{k \sigma_A a^2}{2z^2} \right) e^{-a^2/W_0^2} \right|^2, \tag{1.48}$$

and the one for the amplitude (Eqs. 1.44 and 1.46) is

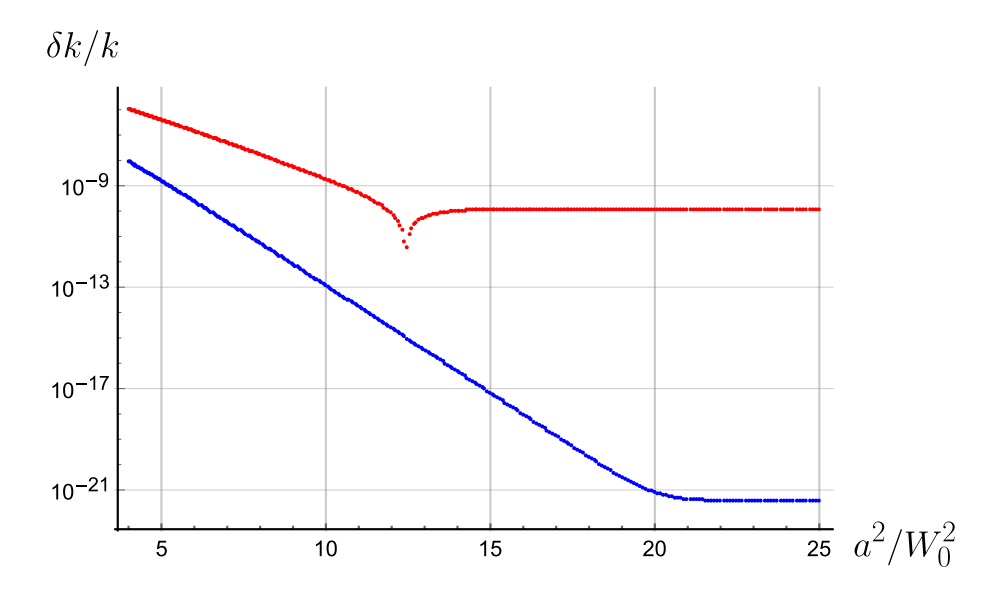


Figure 1.8: The absolute value of the photon recoil correction is presented as a function of aperture size for both the phase gradient term (depicted in blue) and the amplitude-dependent term (illustrated in red), corresponding to the first and second terms in Equation 1.40. In this analysis, we have excluded the oscillating component and retained only the envelope. The parameters utilized include  $z_0 = 10^3$  m,  $\lambda = 780$  nm, z = 2 m,  $W_0 = 1.5$  cm,  $z_W = 0$ , and  $\sigma_A = 1.4 \times 10^{-5}$  m.

$$\frac{1}{2k^2} \frac{\nabla_T^2 A_E}{A_E} \le -\frac{2}{k^2 W(z)^2} + \frac{1}{2} \left(\frac{a}{z}\right)^2 e^{-a^2/W_0^2}.$$
 (1.49)

In both expressions, the first term signifies the asymptotic value linked to a Gaussian beam without an aperture (see Eq. 1.41). The effect of the aperture is captured by the following term, which decreases in a Gaussian fashion. However, the phase contribution (refer to Eq. 1.48) has an exponent that is twice that of the amplitude (as shown in Eq. 1.49), making it negligible for larger aperture sizes.

We investigate the relationship between the photon recoil correction  $\delta k/k$  (as defined in Eq. 1.40) and the size of the atomic cloud (illustrated in Fig. 1.9). Our findings reveal a pattern that closely resembles that depicted in Fig. 1.5 for the amplitude contribution (represented by the red line), indicating a decrease in the correction for cloud sizes exceeding a certain threshold. The Laplacian of the amplitude diffracted through the aperture (as expressed in Eq. 1.46) reaches its peak value precisely at the origin and tends to average out to a lower value as the cloud size increases.

The cutoff size is once more aligned with the central feature of the diffracted beam, as represented by the vertical green dashed line (Eq. 1.36). The contribution from the phase gradient, depicted by the blue line, attains its peak near the cutoff cloud size and remains less than the contribution from the amplitude. Maintaining a small cloud while altering the initial position of the atomic cloud also results in an enhancement of this contribution, which can be assessed using Eq. 1.47.

In order to evaluate the contributions arising from the phase variations discussed in chapter 1.5 alongside those resulting from the photon recoil correction presented in this chapter, we express both as fractional corrections to the measurement of g

$$\frac{\delta g}{g} = -\frac{\langle \Psi_a \rangle}{2gkT^2} + \frac{\delta k_T}{k},\tag{1.50}$$

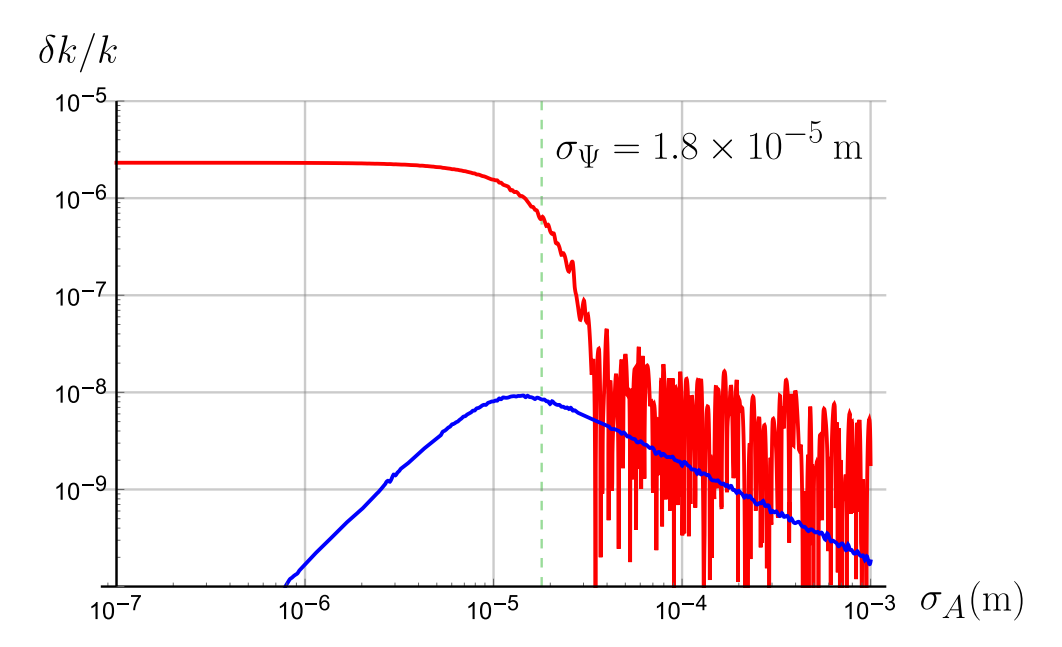


Figure 1.9: The absolute value of the photon recoil correction is presented as a function of the atomic cloud size, distinguishing between the amplitude term (depicted in red) and the phase gradient term (illustrated in blue). For the amplitude term, a similar averaging effect is observed as shown in Fig. 1.5, with a comparable cutoff size indicated by Eq. 1.36 (represented by the green dashed vertical line). In contrast, the phase gradient term achieves its maximum value near the cutoff size but remains lower than the contribution from the amplitude term. The parameters utilized include  $z_0 = 1000$  m,  $\lambda = 780$  nm, z = 2 m,  $w_0 = 1.5$  cm,  $z_0 = 0$ , and  $z_0 = 0$ .

here,  $\langle \Psi_a \rangle$  denotes the total phase attributed to the wavefront aberration caused by the aperture (as indicated in Eq. 1.38), while  $\delta k_T/k = (\delta k_i + \delta k_d)/k$  is defined by Eq. 1.40, which encompasses the contributions from both the incident beam  $(\delta k_i)$  and the diffracted beam  $(\delta k_d)$ .

Given that g is directly proportional to k, any fractional change in k results in an equivalent fractional change in g. Figure 1.10 illustrates the fractional correction in gravimetry, represented as  $\delta g/g$ , arising from the wavefront contributions discussed in chapter 1.5 (indicated by blue points) and those attributed to the photon recoil correction presented in this chapter (denoted by red points). These correspond to the first and second terms of Eq. 1.50, respectively. For a small atomic cloud, the envelope for both terms can be approximated by (Eqs. 1.38 and 1.49)

$$\delta g/g \simeq \left(-\frac{1}{2gkT^2} + \frac{a^2}{2z^2}\right)e^{-a^2/W_0^2}.$$
 (1.51)

Both contributions, namely the wavefront aberration term  $(-e^{-a/W_0^2}/2gkT^2)$  and the photon recoil term  $(a^2e^{-a^2/W_0^2}/2z^2)$ , demonstrate a Gaussian decay in relation to the size of the aperture. However, they are distinguished by different factors that determine the importance of each contribution. Over extended durations, the photon recoil correction emerges as the dominant factor, as the wavefront aberration contribution is quantified as a phase that accumulates during the dark intervals of the interferometric sequence. The two contributions are equal at a specific time determined by

$$T = \frac{z}{a\sqrt{gk}},\tag{1.52}$$

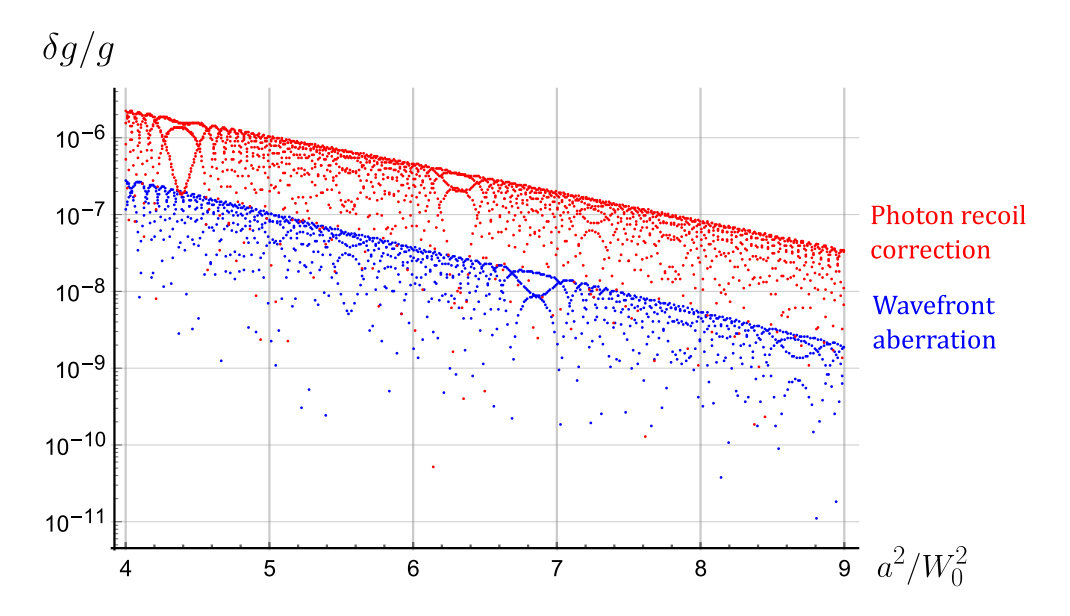


Figure 1.10: The absolute value of the fractional correction in gravimetry, represented as  $\delta g/g$ , is due to wavefront aberrations (shown in blue) and the photon recoil correction (shown in red), which correspond to the first and second terms of Equation 1.50. The parameters used are  $z_0 = 1000$  m,  $\lambda = 780$  nm, z = 2 m,  $W_0 = 1.5$  cm,  $z_W = 0$ , and  $\sigma_A = 10^{-7}$  m.

the relationship is influenced by both the aperture size and the diffraction distance. Under the specified parameters, they contribute equally at a time of T = 7 ms for an aperture size of  $a = 2W_0$ .

In conclusion, the findings from chapters 1.5 and 1.6 indicate that the presence of an aperture in the Raman beams contributes significantly and must be considered or mitigated. Analyzing traps with a size of  $\sigma_A$  and an initial position that fluctuates within a range of  $\sigma_i$  is effectively the same as examining a trap with a fixed initial position but with an adjusted size of  $\sigma_t = \sqrt{\sigma_A^2 + \sigma_i^2}$ . In typical experimental setups, the size  $(\sigma_t)$  exceeds the cutoff value  $\sigma_{\Psi}$  (as defined in Eq. 1.36), resulting in a correction reduction of approximately two orders of magnitude when compared to a smaller atomic cloud.

#### 1.7 Conclusion

With the miniaturization of atomic sensors, a significant truncation of the excitation beams occurs. We assess the impact of this aperture on the trajectory of the Raman beams in atomic gravimetry. The truncation of the Gaussian wings results in the formation of a diffraction pattern. The ripples in the wavefront cause a displacement of the interference fringes, consequently affecting the measured gravitational acceleration. It is the phase variations, rather than amplitude variations, in the wavefront that primarily influence this effect.

A significant shift in the interference fringes occurs for atoms positioned directly along the optical axis of the beam, exhibiting rapid oscillations in relation to the aperture size. Accounting for this shift in a practical experimental setting would be quite complex; therefore, we instead established an upper limit for its impact on the gravimetric phase, which exhibits a Gaussian decay as the aperture size increases. Additionally, this shift demonstrates an oscillating transverse dependence. In the case of atomic clouds with widths exceeding the width of the central ripple of the wavefront, an averaging effect

is observed, which diminishes the contribution from diffraction caused by the aperture. Notably, all points along the edge of a circular aperture contribute coherently, resulting in a more pronounced effect compared to that of a rectangular aperture.

Although the transverse intensity variations may have an insignificant impact on the aforementioned effect, they provide a significant correction to the photon recoil, which in turn alters the measurement of gravitational acceleration. Similarly to previous observations, this correction diminishes in its contribution when averaged over extensive atomic samples.

The shift in the interference fringes, along with the photon recoil correction, leads to a change in the measurement of a comparable magnitude over a duration of approximately 7 ms for the specified parameters. Notably, the intensity fluctuations emerge as the primary correction factor during extended measurement periods. We recommend to experimentalists that if an aperture is located in the path of the Raman beams, the radius of the aperture should exceed three times the beam's waist at the point of entry (a > 3W(z)). Alternatively, if feasible, the aperture should be designed in a square geometry to decrease further more the error contribution due to distortions. These findings will be instrumental in determining the minimum size of an apparatus that can still ensure a specific level of accuracy. The prior research has been formally completed, resulting in the publication of a research article [60].

#### Abstract II

We expand on a new approach for determining whether two molecules interact to create a compound molecule. This method involves exciting the sample using two distinct laser frequencies and assessing the relative phase shift of the transmitted light. The proposed design stimulates the sample within the optical range where a significant response occurs and utilizes a hybrid microwave interferometer to measure the phase. The method has advantageous scaling with the experimental parameters. This approach is highly resilient to external phase variations, including those caused by temperature changes, which typically pose the greatest challenge in interferometric measurements.

## Chapter 2

# A Novel Hybrid Microwave Interferometer for Detection of Molecular Interactions

#### 2.1 Introduction

This section of my thesis builds on previous research conducted by a colleague [61]. In their study, they successfully achieved a comprehensive characterization of the signals produced by atomic transitions both in resonance (absorption and fluorescence) and offresonance (phase change). As part of this characterization, they took into account various noise sources, including dark current, shot noise, and technical noise, aiming to establish a detection threshold for the number of particles associated with each method. They focused on the characterization of signals and noise sources in relation to the experimental parameters to enhance the signal-to-noise ratio for each approach. Additionally, they introduced a hybrid interferometer featuring one arm with two laser frequencies in the optical domain interacting with a sample, and a second arm functioning in the microwave domain. Their efforts were directed towards deriving an analytical expression for the signal of the hybrid interferometer to characterize it using multiple experimental parameters, while also incorporating various noise sources to optimize the signal-to-noise ratio. Nevertheless, the characterization of the proposed design was incomplete in their research; however, they achieved a significant result that serves as the basis for my work and builds on the previous findings.

In recent decades, there has been a significant rise in interest in the detection of molecules and their interactions at the single-particle level. Today, there are numerous methods for the detection and characterization of these molecules [62, 63]. Our focus here is on methods that use radiation, which represent a substantial portion of the available methods [64, 65, 66, 67, 68, 69, 70, 71]. Generally speaking, with respect to the interaction of light with the sample, one could classify them as resonant or non-resonant methods. Resonant techniques usually involve prior knowledge of the sample in question, and the radiation is absorbed in the medium and re-emitted as fluorescence. Resonant methods are usually preferred because they give a stronger signal. Sometimes, the molecules have a weak response to radiation or their concentration is so low that the signal is buried in the noise. One solution is the use of fluorophores that attach to the particle of interest and enhance fluorescence [72]. When using this technique, it is called labeling and it is important to ensure that the molecular interaction is not modified compared to the label-free case.

In non-resonant methods, the absorption of the radiation is so low that the effect of the medium is detected by measuring the changes to the transmitted light. Usually non-resonant methods do not require prior knowledge of the sample in order to detect it; therefore, they open the possibility to detect a plethora of samples without changing the experimental setup, and since they do not rely on the resonant interaction with light there is no need for a labeling technique. These methods have been of great interest in recent years [73, 74], and there have been great advances in their detection capabilities [75, 76, 77]. Some of the current methods that produce remarkable results are whispering gallery modes [78, 79, 80] and surface plasmon resonance [81] as well as methods that use the enhancement properties of optical cavities for label-free detection [82]. There has also been great advances in microscopy, in combination with scattering interference, that allow us to visualize nanoparticles beyond the diffraction limit [83] and even able to image a single atom [84]. Standard interferometric techniques can be classified as non-resonant label-free methods of detection, and they have been shown to be a reliable bio-sensor [85]. Aiding both resonant and non-resonant methods, there are some techniques that increase the sensitivity for detection, such as functionalization of a surface, which will fix particles to the surface instead of drifting in the solution by Brownian motion, or by focusing light onto the sample which will increase the light-matter interaction, both of these techniques increase the average particle density perceived by the detector, which will directly result into a larger signal and it will provide a lower concentration limit.

Besides classifying the methods as resonant or non-resonant, one could also consider an extra classification by taking into account the number of light beams used in the detection, for example a modern resonant two-beam method would be Surface-Enhanced Raman Spectrocscopy, which has been shown to be able to reach the single-molecule detection regime [86, 87] and one can also use a combination of resonant and non-resonant methods in order to enhance the detection properties [88, 89]. With these classifications in mind we can note that while on the resonant methods there are those involving one or two light beams, on the non-resonant methods only exist those with one light beam. What we propose here is an entirely new type of method, a non-resonant two-beam method involving a hybrid microwave-optical interferometer capable of detecting Raman dynamics without the dispersion of light.

Here I introduce a detection method that utilizes a two-photon transition measured outside of resonance. Non-resonant detection can be achieved by exciting with two frequencies and observing phase changes in the two transmitted beams. This approach has not been fully exploited thus far, likely due to its reliance on a nonlinear effect that is diminished by being out of resonance. The second frequency is not generated from fluorescence; rather, it is already incorporated into the excitation process. Consider, for instance, two relatively new molecules about which we have limited knowledge, yet we still wish to determine if they can form a compound molecule. The combination of these two molecules modifies their vibrational and rotational spectrum. In this case, usually one could use Raman spectroscopy; however, because of our limited knowledge of the molecules, identifying the significant peaks in the molecular spectrum will likely prove challenging. When we excite the molecules using two different frequencies, it is probable that we will not be in resonance with any two-photon transition, which means that we are dealing with a non-resonant excitation. However, as we will demonstrate later on, there exists a signal that can be extracted to determine the formation or absence of the compound molecule. Although the method may not provide extensive details regarding the interaction between the two molecules, it should be capable of determining whether an arbitrary pair of molecules forms a compound. The proposed method involves

non-resonant (relative phase) detection utilizing two excitation frequencies.

#### 2.2 Traditional methods

In this section, I will take on a few traditional detection methods, resonant and non-resonant, which are absorption, fluorescence, and a one-beam phase change in the form of a Mach-Zehnder interferometer, as illustrated in Fig. 2.1. I will obtain an analytical expression for the signal in the form of an electric current that they might produce when detecting a sample. For all methods, the detected light will be measured using a photodiode, which provides a current  $i_{\rm pd}$  proportional to the incident light power P on its surface  $i_{\rm pd}=RP$ , where R is the photodiode responsivity, an intrinsic property of each type of photodiode.

#### 2.2.1 Fluorescence and Absorption

Beginning with fluorescence spectroscopy, where a beam of light passes through a sample and with a lens, we collect the re-emitted light (Fig. 2.1a). I model the sample as a two-level system with a spontaneous decay rate  $\gamma$  from the excited state, see Fig. 2.1d. The system is subject to an external oscillating electric field of the form

$$\vec{E} = E\vec{\xi}\cos\left(kz - \omega_l t + \phi_E\right),\tag{2.1}$$

The specifics of the dynamics of such a system is quite well known in literature [49], so I will skip the full procedure and only focus on the task at hand. Due to spontaneous emission, most of the sample population remains in the ground state  $|b\rangle$ , but because of the presence of the external field, the excited  $|a\rangle$  state begins to be populated. As population is driven from the ground  $|b\rangle$  to the excited  $|a\rangle$  state the sample then radiates photons in all directions with a rate of emission  $\gamma_p = \gamma \rho_{aa}$  where  $\rho_{aa}$  is the population in the excited  $|a\rangle$  state. Because of the spontaneous emission, the radiated power per unit volume of the sample is  $\hbar\omega_{ab}\gamma\rho_{aa}N$ , where  $\hbar\omega_{ab}$  is the energy of the radiated photons,  $\omega_{ab} = \omega_a - \omega_b$  is the frequency of transition, and N is the density of particles. The total volume of the sample that actively emits photons is V = lA where l is the length of the sample, and A is the transverse beam area, to simplify things, I choose that the beam area is equal to the sample area. The total radiated power is then  $\hbar\omega_{ab}\gamma\rho_{aa}NlA$ , which we collect only a fraction  $\eta$  of this power with the aid of a lens,  $\eta$  is called the collection efficiency. The total power arriving at the photodiode is then

$$P = \eta \hbar \omega_{ab} \gamma \rho_{aa} NlA, \tag{2.2}$$

and the current that the photodiode emits for the fluorescence method is

$$i_{\rm f} = R\eta\hbar\omega_{ab}\gamma\rho_{aa}NlA. \tag{2.3}$$

Now, by slightly changing the setup, we can perform absorption spectroscopy (Fig. 2.1 b). Without the sample the photodiode receives the full power of the light beam P which makes it emit a current of magnitude  $i_l = RP$ . But with the sample, the transmitted power is decreased by the dispersed amount, so the transmitted power arriving at the photodiode is then

$$P_{\text{sample}} = P - \hbar \omega_{ab} \gamma \rho_{aa} NlA, \qquad (2.4)$$

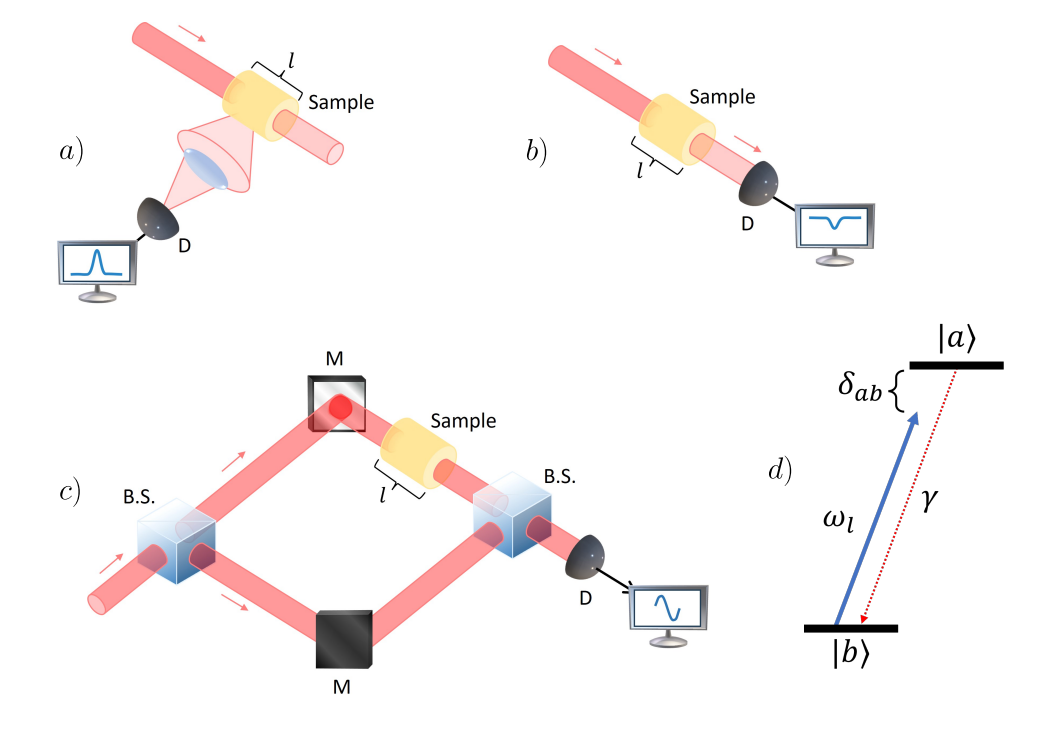


Figure 2.1: Illustration of several common detection methods, a) fluorescence spectroscopy, b) absorption spectroscopy, c) Mach-Zehnder interferometer for phase change measurements. In this figure D is a photodiode detector, B.S. stands for Beam Splitter and M for Mirror. Figure d) show a diagram of a two-level quantum system with decay rate  $\gamma$  being driven by an external electric field of frequency  $\omega_l$  and detuning  $\delta_{ab}$ .

and the current is

$$i_{\text{sample}} = RP - R\hbar\omega_{ab}\gamma\rho_{aa}NlA,$$
 (2.5)

and by taking the difference between the current with no sample and the current with the sample I obtain

$$i_{a} = R\hbar\omega_{ab}\gamma\rho_{aa}NlA. \tag{2.6}$$

We can appreciate that the expressions for the currents for fluorescence and absorption are very similar, albeit except for the collection efficiency, this is because it is the same phenomenon just different detection procedures. Both expressions depend on the excited-state population, which for a two-level system in the steady state is [49]

$$\rho_{aa} = \frac{|\Omega_{ab}|^2}{\gamma^2 + 2|\Omega_{ab}|^2 + 4\delta_{ab}^2},\tag{2.7}$$

where  $\Omega_{ab} = -e\vec{\xi} \cdot \langle a|\vec{r}|b\rangle (E/\hbar)e^{i\phi_E}$  is the Rabi frequency and  $\delta_{ab} = \omega_l - \omega_{ab}$  the detuning. By using the definition of the on-resonance saturation parameter  $s_0 = 2|\Omega_{ab}|^2/\gamma^2 = I/I_s$  where  $I_s = \gamma \pi h c/3\lambda_{ab}^3$  is the saturation intensity [49]; I can rewrite the expression for the excited state population for the steady-state case as

$$\rho_{aa} = \frac{s_0/2}{1 + s_0 + (2\delta_{ab}/\gamma)2},\tag{2.8}$$

for low intensities  $(s_0 < 1)$  I can approximate it by

$$\rho_{aa} \approx \frac{s_0/2}{1 + (2\delta_{ab}/\gamma)^2},\tag{2.9}$$

where we can see that it depends on  $\delta^{-2}$ , this means that unless we are very close to resonance ( $|\delta_{ab}| < \gamma$ ) the current is very suppressed and it would be difficult to detect any particles. One way to circumvent this is by increasing the intensity of the light beam, which will broaden the dispersion curve, as its show in Fig. 2.2, and also increase the decay rate  $\gamma \to \sqrt{\gamma^2 + 2|\Omega_{ab}|^2}$  [49]. However, this will also increase the noise in the detection [61], so there is a counterpoint to increasing the light intensity to obtain a stronger signal if the detuning is high.

An important factor to consider as well is the Doppler effect, since the particles in the sample have a velocity distribution due to the thermal energy, even if the light is right on resonance  $\omega_l = \omega_{ab}$ , there still exist a detuning due to the Doppler effect  $\delta_{ab} = -\omega_{ab}v_z/c$ , then averaging the excited state population over the distribution of velocities for a laser set on resonance with the static atoms we have

$$\bar{\rho}_{aa} = \int_{-\infty}^{\infty} \frac{s_0/2}{1 + s_0 + \frac{4\omega_{ab}^2 v_z^2}{\sigma^2 c^2}} \sqrt{\frac{m}{2\pi k_B T}} \exp\left(-\frac{mv_z^2}{2k_B T}\right) dv_z, \tag{2.10}$$

with a change of variables in the form of  $u^2 = \omega_{ab}^2 v_z^2 / \gamma^2 c^2$  I obtain

$$\bar{\rho}_{aa} = \frac{s_0}{2} \sqrt{\frac{m}{2\pi k_B T}} \int_{-\infty}^{\infty} \frac{1}{1 + s_0 + 4u^2} \exp\left(-\frac{m\gamma^2 c^2 u^2}{2\omega_{ab}^2 k_B T}\right) \frac{\gamma c}{\omega_{ab}} du, \tag{2.11}$$

and by defining  $\sigma_v = \sqrt{k_B T/m}$ , which is the width of the velocity distribution, I can now define a width of detunings due to the Doppler effect as  $\sigma_D = \omega_{ab} \sigma_v/c$ , using these definitions I rewrite  $\bar{\rho}_{aa}$  as

$$\bar{\rho}_{aa} = \frac{s_0}{2} \frac{\gamma}{\sigma_D} \frac{1}{\sqrt{2\pi}} \int_{-\infty}^{\infty} \frac{1}{1 + s_0 + 4u^2} \exp\left(-\frac{\gamma^2 u^2}{2\sigma_D^2}\right) du, \tag{2.12}$$

approximating for low intensities  $s_0 < 1$ , we can obtain an analytical expression for the integral and the result is

$$\bar{\rho}_{aa} = \frac{s_0}{2} \left[ \sqrt{\frac{\pi}{8}} \frac{\gamma}{\sigma_D} \exp\left(\frac{\gamma^2}{8\sigma_D^2}\right) \operatorname{Erfc}\left(\sqrt{\frac{\gamma^2}{8\sigma_D^2}}\right) \right], \tag{2.13}$$

and since the expression in the square parentheses does not depend on intensity I can write it as a coefficient of Doppler correction  $C_D$ 

$$C_D = \sqrt{\frac{\pi \gamma^2}{8\sigma_D^2}} \exp\left(\frac{\gamma^2}{8\sigma_D^2}\right) \operatorname{Erfc}\left(\sqrt{\frac{\gamma^2}{8\sigma_D^2}}\right). \tag{2.14}$$

For example, using Rubidium with  $\gamma = 2\pi \times 6 \times 10^6 \text{Hz}$ ,  $\omega_{eg} = 384.23 \times 10^{14} \text{Hz}$ , and T = 300 K I obtain  $C_D \approx 0.1$ , which means that we only work with around 10% of the atoms. If we consider a Doppler width greater than the natural width  $\sigma_D > \gamma$  then we can make the following approximations,  $\exp\left(\gamma^2/8\sigma_D^2\right) \approx 1$  and  $\operatorname{Erfc}\left(\sqrt{\gamma^2/8\sigma_D^2}\right) \approx 1$ , with those in mind then the coefficient  $C_D$  is now

$$C_D \approx \sqrt{\frac{\pi}{8}} \frac{\gamma}{\sigma_D},$$
 (2.15)

this shows that the factor  $C_D$  ends up being the ratio of the natural width  $(\gamma)$  and the Doppler width  $(\sigma_D)$ , meaning that off all the atoms in the sample we only excite the

fraction that is approximately within the natural width. The expression of  $\bar{\rho}_{aa}$  can now be rewritten as  $\bar{\rho}_{aa} = s_0 C_D/2$ . In the case when the temperature is zero, the integral in Eq. 2.10 becomes the integral of the coefficient of population of the excited state and a Dirac delta distribution, which by its properties evaluates any function of  $v_z$  into the center of the distribution which in this case is 0, so in the case for zero temperature we obtain  $\bar{\rho}_{aa} = (s_0/2)/(1+s_0)$  and for low intensities we obtain the approximation  $\bar{\rho}_{aa} \approx s_0/2$ . This means that the coefficient for Doppler correction  $C_D$  is equal to 1 meaning that we excite all the atoms in the sample, this is reasonable because we are in resonance with all the atoms. Now substituting this result into the expression for the current in the fluorescence scheme (Eq. 2.3) I obtain

$$i_{\rm f} = R\eta\hbar\omega_{ab}\gamma\frac{s_0}{2}C_DNlA, \qquad (2.16)$$

and replacing the definition of  $s_0$  and regrouping I obtain

$$i_{\rm f} = RNl\eta \left(\frac{\hbar\omega_{ab}\gamma}{2I_s}\right)(IA)C_D,$$
 (2.17)

where IA = P, where P is the power of the incident light beam, and  $\hbar\omega_{ab}\gamma/2I_s = 3\lambda_{ab}^2/2\pi = \sigma$  is the cross section of light-matter interaction [49]; with this relations I can rewrite the previous expression as

$$i_{\rm f} = RP(Nl\sigma)\eta C_D, \tag{2.18}$$

similarly, for absorption I obtain

$$i_{\rm a} = RP(Nl\sigma)C_D,\tag{2.19}$$

now, without explicitly working out the dependence of  $\rho_{aa}$  I can obtain similar expressions, for fluorescence I obtain

$$i_{\rm f} = RP(Nl\sigma)\eta\gamma^2 \frac{\rho_{aa}}{|\Omega_{ab}|^2},\tag{2.20}$$

and for absorption

$$i_{\rm a} = RP(Nl\sigma)\gamma^2 \frac{\rho_{aa}}{|\Omega_{ab}|^2}.$$
 (2.21)

Although the last expressions do not consider the Doppler effect, since that involves working explicitly with the expression for  $\rho_{aa}$ , they are helpful for further comparisons, mainly we can observe that these resonant methods involve the population in the excited state, because the method for detection involves measuring the emitted or absorbed photons; also we can see that the two methods depend on the density of particles N with units  $1/m^3$ , the length of the sample l with units m, and the cross section of interaction  $\sigma$  with units  $m^2$ , where the product of the three is a number that I interpret to be the effective number of interacting particles  $Nl\sigma$ .

### 2.2.2 Phase Change

Moving forward, now I analyze the phase change detection method, we have a light beam that is split, sent through different paths, where in one path the beams goes through the sample, recombined, and then measured with a photodiode (Fig. 2.1 c). In this case the frequency of the beam is so far off from any transition of the sample that there is no absorption or fluorescence even if I increase the intensity ( $|\delta| \gg \gamma$ ,  $|\Omega_{ab}|$ ). The magnitude

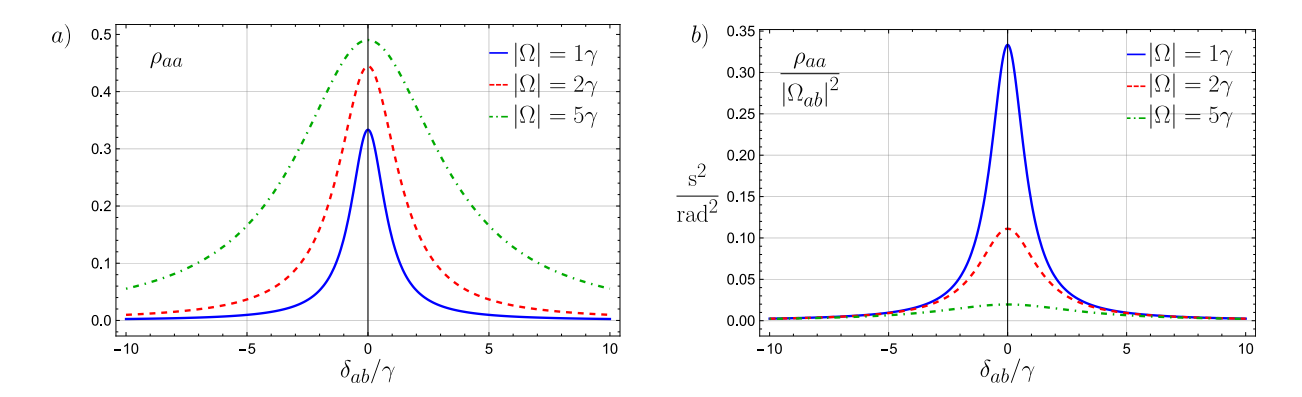


Figure 2.2: Graph of the coefficient of population  $\rho_{aa}$  for the excited state  $|a\rangle$  as a function of the detuning  $\delta_{ab}$ . For b) I have plotted the ratio  $\rho_{aa}/|\Omega_{ab}|^2$  as it appears in Eqs. 2.20 and 2.21. For both graphs I have plotted several values for the Rabi frequency, for the solid blue line  $|\Omega| = 1\gamma$ , for the red dashed line  $|\Omega| = 2\gamma$ , and for the green dot-dashed line  $|\Omega| = 5\gamma$ .

of the optical field when going through the sample remains unchanged, but not its phase, since the sample has a refractive index n. First consider a scenario without the sample but with a path difference of  $\Delta z$  between the arms, in this case the intensity arriving at the detector is

$$I = I_0 \frac{1}{2} (1 + \cos k \Delta z), \qquad (2.22)$$

with  $I_0 = \frac{1}{2}\epsilon_0 c E^2$ . To be more susceptible to phase changes in the interferometer, it is common to choose  $k\Delta z = \pi/2$  to be in the linear response of the interference fringes. With this selection, the intensity arriving at the photodiode is just  $I = I_0/2$  and the current that emmits is

$$i_{\text{n.s.}} = RP/2,$$
 (2.23)

with  $P = AI_0$ . Now with a sample of length l and index of refraction n in one of the beams, there will be a phase difference in the arm with the sample given by  $\phi = kl(n-1)$ , the intensity arriving at the photodiode is

$$I_{\text{w.s.}} = I_0 \frac{1}{2} (1 + \sin(\phi)),$$
 (2.24)

still considering that  $k\Delta z = \pi/2$ , the current is then

$$i_{\text{w.s.}} = RP \frac{1}{2} (1 + \sin(\phi)).$$
 (2.25)

By taking the difference between the current with the sample Eq. 2.25 and the current with no sample Eq. 2.23, we are able to isolate just the effect of the phase change introduced by the sample, and I obtain the following expression

$$i_{\text{phase}} = \frac{1}{2} RP \sin(\phi). \tag{2.26}$$

Considering a small phase  $\phi < 1$  and substituting the expression for the phase  $\phi$  I obtain

$$i_{\text{phase}} \approx \frac{1}{2}RP\phi = \frac{1}{2}RPkl(n-1),$$
 (2.27)

where now, I have to work on an expression for the index of refraction that relates to the quantum properties of the sample. First, let us recall that we can write the polarization

density of a homogeneous dielectric isotropic material in two different ways, one being proportional to the external electric field [90]

$$P = \frac{1}{2}\tilde{\chi}\epsilon_0\tilde{E} + c.c., \tag{2.28}$$

where  $\tilde{\chi}$  is the complex electric susceptibility of the medium. I can rewrite it as follows

$$P = \epsilon_0 E \left( \chi_{re} \cos \phi_E - \chi_{im} \sin \phi_E \right). \tag{2.29}$$

The other way to write the polarization density is that we consider the medium as a homogeneous density of dipole moments

$$P = N\langle \mu \rangle, \tag{2.30}$$

where  $\langle \mu \rangle$  is the average dipole moment. Modeling our sample as a distribution of two-level quantum systems, we can follow the formalism of the density matrix to write

$$N\langle\mu\rangle = N \operatorname{Tr}\left[\rho\mu\right] = N\mu_{ab}\left(\rho_{ab} + \rho_{ba}\right) = N\mu_{ab} 2\operatorname{Re}\left[\rho_{ab}\right],\tag{2.31}$$

where in this previous equation  $\mu_{ab} = \mu_{ba}$  since it's a real measurable quantity defined as  $\mu_{ab} = \vec{\xi} \cdot \langle a|e\vec{r}|b\rangle$ , and  $\rho_{ab}$  is the coherence term between the ground  $|b\rangle$  and excited  $|a\rangle$  levels. Now, lets multiply  $\rho_{ab}$  by a factor of 1 to obtain

$$P = 2N\mu_{ab} \operatorname{Re} \left[ \Omega_{ab} \rho'_{ab} \right], \qquad (2.32)$$

with  $\rho'_{ab} = \rho_{ab}/\Omega_{ab}$ , and  $\Omega_{ab} = -(\mu_{ab}E/\hbar)e^{i\phi_E}$ , I then expand the previous expression to obtain

$$P = 2N\mu_{ab} \left( \operatorname{Re} \left[ \Omega_{ab} \right] \operatorname{Re} \left[ \rho'_{ab} \right] - \operatorname{Im} \left[ \Omega_{ab} \right] \operatorname{Im} \left[ \rho'_{ab} \right] \right), \tag{2.33}$$

and by explicitly replacing the expression for  $\Omega_{ab}$  I obtain

$$P = \frac{2N\mu_{ab}^{2}E}{\hbar} \left( -\cos\left[\phi_{E}\right] \operatorname{Re}\left[\rho_{ab}^{'}\right] + \sin\left[\phi_{E}\right] \operatorname{Im}\left[\rho_{ab}^{'}\right] \right). \tag{2.34}$$

By equating both expressions for the polarization density (Eq.2.29 and 2.34) I obtain the following expressions for the real and imaginary parts of the electric susceptibility

$$\chi_{re} = -\frac{2N\mu_{ab}^2}{\hbar\epsilon_0} \operatorname{Re} \left[ \frac{\rho_{ab}}{\Omega_{ab}} \right], \qquad (2.35)$$

$$\chi_{im} = -\frac{2N\mu_{ab}^2}{\hbar\epsilon_0} \operatorname{Im} \left[ \frac{\rho_{ab}}{\Omega_{ab}} \right].$$

Now, recalling that the refractive index of a medium depends on the relative permittivity and relative permeability of the medium  $n = \sqrt{\epsilon_r \mu_r}$  with  $\epsilon_r = 1 + \tilde{\chi}$  and  $\mu_r = 1$  since I do not consider any magnetic effects in the medium, we obtain for the refractive index then  $n = \sqrt{1 + \tilde{\chi}}$ , approximating for small values of the electric susceptibility I obtain

$$\tilde{n} \approx 1 + \frac{1}{2}\chi_{re} + i\frac{1}{2}\chi_{im},\tag{2.36}$$

where the imaginary part is proportional to the absorption of the medium and the real part is the traditional refractive index, by replacing the expression for the real part of the electric susceptibility I obtain the following expression for the refractive index

$$n = 1 - \frac{N\mu_{ab}^2}{\hbar\epsilon_0} \operatorname{Re}\left[\frac{\rho_{ab}}{\Omega_{ab}}\right]. \tag{2.37}$$

Substituting this expression into the current for the interferometer Eq. 2.27 I obtain

$$i_{\text{phase}} = \frac{1}{2} RPkl \frac{N\mu_{ab}^2}{\hbar\epsilon_0} \text{Re} \left[ -\frac{\rho_{ab}}{\Omega_{ab}} \right],$$
 (2.38)

and using the relation for a two level system  $\gamma = \omega_{ab}^3 \mu_{ab}^2 / 3\pi \epsilon_0 \hbar c^3$  [49] and rearranging some terms I obtain

$$i_{\text{phase}} = \frac{1}{2} RP(Nl) \left(\frac{3\pi k}{k_{ab}^3}\right) \gamma \text{Re} \left[-\frac{\rho_{ab}}{\Omega_{ab}}\right].$$
 (2.39)

Now, k is the wavevector of the field and  $k_{ab}$  is the wavevector of the  $a \leftrightarrow b$  transition. I can write  $k/k_{ab}^3$  in terms of their angular frequencies to obtain

$$\frac{k}{k_{ab}^3} = \frac{c^2 \omega_l}{\omega_{ab}^3},\tag{2.40}$$

and use the definition of the detuning  $\delta = \omega_l - \omega_{ab}$  to obtain

$$\frac{k}{k_{ab}^3} = \frac{c^2}{\omega_{ab}^2} + \frac{c^2 \delta_{ab}}{\omega_{ab}^3} = \frac{1}{k_{ab}^2} \left( 1 + \frac{\delta_{ab}}{\omega_{ab}} \right). \tag{2.41}$$

Although we are highly detuned from the transition ( $|\delta_{ab}| \gg \gamma$ ,  $|\Omega_{ab}|$ ) I consider that the detuning  $\delta_{ab}$  will be small compared to  $\omega_{ab}$  and therefore  $\delta_{ab}/\omega_{ab} \ll 1$ . With this approximation, I can write the expression for the current as

$$i_{\rm phase} \approx \frac{1}{2} RP(Nl\sigma) \gamma \text{Re} \left[ -\frac{\rho_{ab}}{\Omega_{ab}} \right].$$
 (2.42)

I can compare this expression with the currents for fluorescence and absorption (Eq. 2.20 and Eq. 2.21), all three expressions have in common the following quantities, incident beam power P, particle density N, sample length l, and cross section of interaction  $\sigma$ , which highlights the common phenomenon in all three methods, the light-matter interaction. However, here the signal current depends on the coherence between the quantum levels, in this way one can consider the interferometric scheme of detection as a measurement of coherence in a system, if it were a pure ensemble, meaning that there is no coherence between levels, this current will be zero.

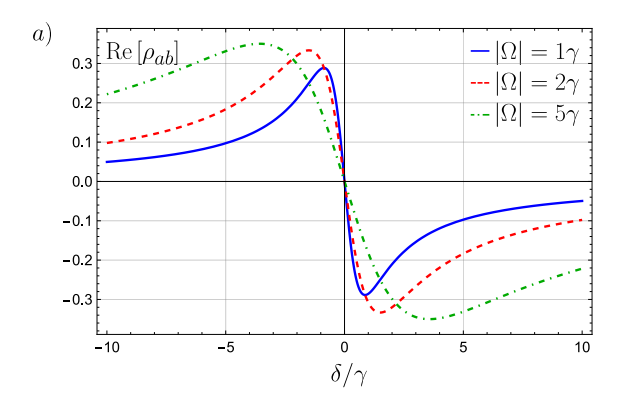
By working out explicitly the expression for  $\rho_{ab}$  in the steady-sate case I obtain [49]

$$\rho_{ab} = \frac{(i\gamma - 2\delta_{ab})\,\Omega_{ab}}{\gamma^2 + 2|\Omega_{ab}|^2 + 4\delta_{ab}^2}.$$
(2.43)

I have plotted the real part of the coherence in Fig. 2.3, I only choose the real part since it is proportional to the signal of the interfeometer. The shape of the real part of  $\rho_{ab}$  shows a dispersive form that widens as the intensity, or in this case the Rabi frequency, increases. Approximating for a large detuning  $|\delta_{ab}| \gg \gamma$ ,  $|\Omega_{ab}|$  and substituting into the expression for the current I obtain

$$i_{\text{phase}} \approx \frac{1}{2} RP(Nl\sigma) \frac{\gamma}{2\delta_{ab}},$$
 (2.44)

where we can observe a scaling with the detuning as  $\delta^{-1}$ , this is quite helpful as a method of detection, compared with resonant methods. In a resonant method, one requires



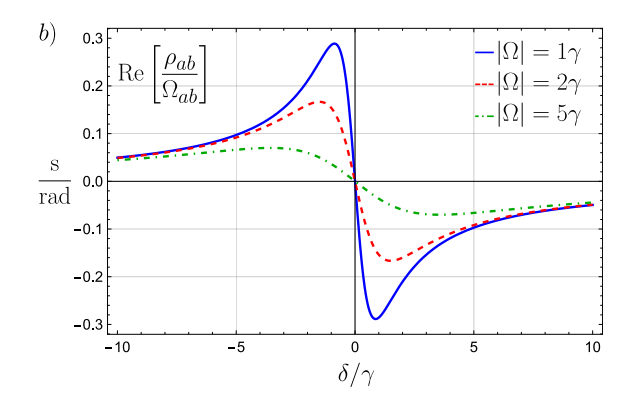


Figure 2.3: Graph of the coefficient of coherence  $\rho_{ab}$  between the excited  $|a\rangle$  and ground levels  $|b\rangle$  as a function of the detuning  $\delta_{ab}/\gamma$ . For b) I have plotted the real part of the ratio  $\rho_{ab}/\Omega_{ab}$  as it appears in Eq. 2.38. For both graphs I have plotted several values of the Rabi frequency, for the solid blue line  $|\Omega| = 1\gamma$ , for the red dashed line  $|\Omega| = 2\gamma$ , and for the green dot-dashed line  $|\Omega| = 5\gamma$ .

prior knowledge, like the resonant transition frequency, to be able to strongly detect the particle of interest. Here, with a non-resonant detection, one might not need to know such information because the current signal is not as suppressed if one is out of resonance with the transition. However, one of the biggest limitations of this type of detectors is the fluctuations due to temperature, a change in temperature introduces a change in sample length  $\Delta l$  as well as a change in the refractive index  $\Delta n$  which translate into a change in the measured phase

$$\phi + \Delta \phi = k(l + \Delta l)(n + \Delta n - 1)$$

$$= kl(n - 1) + k\Delta l(n - 1) + kl\Delta n + k\Delta l\Delta n,$$
(2.45)

and the change in phase due to temperature fluctuations is

$$\Delta \phi = k \left( \Delta l(n-1) + l \Delta n + \Delta l \Delta n \right). \tag{2.46}$$

Since k is in the optical range, this change in phase can be considerable. I have then obtained expressions for the current for the three methods, to end this chapter, let us present the equations of the currents for the different methods, in their two versions, that I have obtained so far

Fluorescence: 
$$i_{\rm f} = RP(Nl\sigma)\eta C_D \gamma^2 \frac{\rho_{aa}}{|\Omega_{ab}|^2}; \quad i_{\rm f} = RP(Nl\sigma)\eta C_D.$$
 (2.47)

Absorption: 
$$i_{\mathbf{a}} = RP(Nl\sigma)C_D\gamma^2 \frac{\rho_{aa}}{|\Omega_{ab}|^2}; \quad i_{\mathbf{a}} = RP(Nl\sigma)C_D.$$
 (2.48)

Phase change: 
$$i_{\text{phase}} = \frac{1}{2} RP(Nl\sigma) \gamma \text{Re} \left[ -\frac{\rho_{ab}}{\Omega_{ab}} \right]; \quad i_{\text{phase}} = \frac{1}{2} RP(Nl\sigma) \frac{\gamma}{2\delta_{ab}}.$$
 (2.49)

Note that the factor RP by itself has dimensions of current, then all of the other factors must amount to an adimensional factor, and so rightfully do so.

### 2.3 Hybrid Microwave-Optical Interferometer

Here I introduce a Mach-Zehnder type hybrid microwave-optical interferometer. The main incentive behind the design of the interferometer was to measure phase changes of

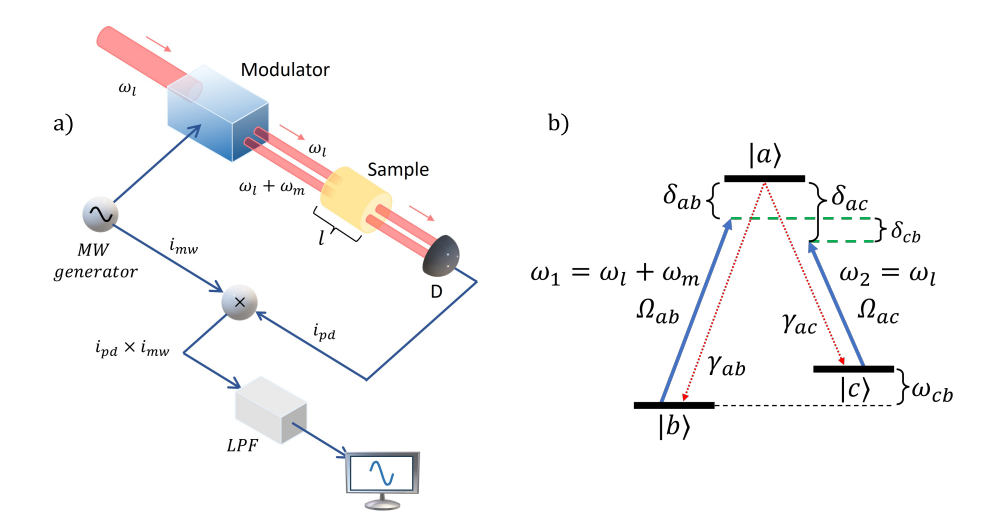


Figure 2.4: a) Schematic for the hybrid microwave-optical interferometer, in this figure  $\omega_l$  is the laser frequency,  $\omega_m$  is the modulation frequency, D is the detector (photodiode), MW stands for microwave, X is a current mixer and LPF stands for low-pass filter. b) Energy diagram of the three-level system,  $\Omega_{ab}$  and  $\Omega_{ac}$  are the Rabi frequencies of the system,  $\gamma_{ab}$  and  $\gamma_{ac}$  are the decay rates from the excited state  $|a\rangle$ ,  $\delta_{ab}$  and  $\delta_{ac}$  are the one-photon detunings,  $\delta_{cb}$  is the two-photon detuning. See appendix C for their definitions.

the lasers due to a coherent Raman process, considering our interest in the alteration of the vibrational or rotational spectra resulting from the combination of the two molecules, it is reasonable to contemplate a measurement that encompasses two frequencies. Standard Raman methods [91] make use of a resonant excitation and a spontaneous process which eliminates any coherence in the system. The set-up consists of a laser that goes through a modulator and filter to block one of the side bands in order to emit two beams at frequencies  $\omega_1$  and  $\omega_2$  with  $\omega_1 = \omega_2 + \omega_m$ , where  $\omega_m$  is the frequency of an RF generator. Both beams pass through the sample, where the sample properties change the phase and the amplitude of the beams, and then arrive at the photo-diode sensor which will produce a current  $S_1$  that depends on the light that arrives on it. The current is combined through a mixer with a second current  $S_2$  originating from the microwave oscillator with a known phase, the signal is then sent to a low-pass filter (LPF) and is then measured. A schematic of the proposed design is illustrated in Fig. 2.4 a).

## 2.3.1 Signal Current for the hybrid microwave-optical interferometer

I begin by deriving the expression for the final current in the hybrid microwave-optical interferometer, the electric fields of the beams right as they arrive at the photo-diode are

$$\tilde{E}_1 = E_1 \exp \left[ i \left( \phi_1 - \omega_1 t \right) \right],$$
  
 $\tilde{E}_2 = E_2 \exp \left[ i \left( \phi_2 - \omega_2 t \right) \right],$ 
(2.50)

where  $\phi_1, \phi_2$  are the phases of each of the beams, these phases have contributions of the initial phase, propagation, modulation, and sample effect. The current produced by the photo-diode from the arriving light intensity is then

$$i_{pd} = \frac{1}{2} R A \epsilon_0 c \left| \tilde{E}_1 + \tilde{E}_2 \right|^2, \tag{2.51}$$

and by expanding this expression I obtain

$$i_{pd} = \frac{1}{2} R A \epsilon_0 c \left( E_1^2 + E_2^2 + 2E_1 E_2 \cos \left[ \phi_1 - \phi_2 - \omega_m t \right] \right)$$
 (2.52)

this current is then mixed with a second current  $i_m$  coming from the RF generator that is feeding the modulator,

$$i_m = \beta \cos \left[\omega_m t - \phi_m\right] \tag{2.53}$$

the mixed current is then

$$i_{mix} = \frac{1}{2}\beta R A \epsilon_0 c \left( E_1^2 \cos \left[ \omega_m t - \phi_m \right] + E_2^2 \cos \left[ \omega_m t - \phi_m \right] \right)$$

$$+ E_1 E_2 \cos \left[ 2\omega_m t - \phi_m - (\phi_1 - \phi_2) \right] + E_1 E_2 \cos \left[ (\phi_1 - \phi_2) - \phi_m \right] ,$$
(2.54)

this current will then be filtered in frequency, allowing only the non-oscillating terms to come through, so I obtain

$$i_{lpf} = \frac{1}{2}\beta R A \epsilon_0 c E_1 E_2 \cos[(\phi_1 - \phi_2) - \phi_m]$$
 (2.55)

with an appropriate selection for the value of the phase of the modulation current  $\phi_m = \pi/2$  and by approximating for small phase values of  $(\phi_1 - \phi_2) < 1$  I obtain

$$i_{\text{hybrid}} \approx RP'\beta \left(\phi_1 - \phi_2\right)$$
 (2.56)

were I introduced the term  $P'=\frac{1}{2}\epsilon_0cE_1E_2A$  which has units of power however is not the total power arriving at the photo-diode, in order to simplify the equations I have made that the cross sectional beam and sample area to be equal. Now let us write the expressions for the propagation phases of the beams, they are

$$\phi_1 = k_1(L - l) + k_1 n_1 l + \phi_{E_1}$$

$$\phi_2 = k_2(L - l) + k_2 n_2 l + \phi_{E_2}$$
(2.57)

where  $n_1, n_2$  are the refraction indexes for beams 1, 2 in the sample, and  $\phi_{E_1}, \phi_{E_2}$  are the initial phase of the each of the beams, so the expression for  $\phi_1 - \phi_2$  is

$$\phi_1 - \phi_2 = k_m(L - l) + (k_1 n_1 - k_2 n_2)l + (\phi_{E_1} - \phi_{E_2})$$
(2.58)

We can see then that the signal will be proportional to the phase difference  $(\phi_1 - \phi_2)$  of the two beams; this makes it really robust against effects that have common changes in the phase of both beams such as temperature variations, which are the dominant error when measuring phase changes [85]. A deviation in temperature changes the length of the sample by a factor  $\Delta l$  likewise the refractive index is changed by a factor  $\Delta n$ , both of these factors contribute to a drift in the phase measurement. Now, since the two frequencies are very similar I take the same  $\Delta n$  for both, and the drift in the phase measurement is given by

$$\Delta (\phi_1 - \phi_2) = k_m ((n-1)\Delta l + \Delta n l + \Delta n \Delta l)$$
(2.59)

where  $k_m = k_1 - k_2$ , is the wavenumber of the modulation frequency. The drift is strongly suppressed in the hybrid microwave-optical interferometer because it scales with the wavenumber of the modulation, which is in the range of microwaves, in contrast to more standard interferometers whose drift scales with an optical wavenumber, which is orders-of-magnitude greater. Similarly as before, I need to make a connection between the quantum properties of the medium and the index of refraction.

### 2.3.2 Index of refraction for the hybrid microwave-optical interferometer

The procedure that I will take will be similar as before for the two-level system and the Mach-Zehnder interferometer. However, since I am modeling our sample as a three-level quantum system, being driven by two electric fields, the expressions for the polarization density are

$$P = \frac{1}{2}\epsilon_0 \tilde{\chi}_1 \tilde{E}_1 + \frac{1}{2}\epsilon_0 \tilde{\chi}_2 \tilde{E}_2 + c.c., \tag{2.60}$$

and

$$P = 2N \left(\mu_{ab} \operatorname{Re} \left[\rho_{ab}\right] + \mu_{ac} \operatorname{Re} \left[\rho_{ac}\right] + \mu_{cb} \operatorname{Re} \left[\rho_{cb}\right]\right), \tag{2.61}$$

but since the levels b and c are very close to each other, I am considering that they are rotational or vibrational levels of a molecule, I can approximate the dipole moment  $\mu_{cb} = e\vec{\xi} \cdot \langle c | \vec{r} | b \rangle$  to zero. I then proceed in a similar fashion as before, equating both expressions for the polarization density, and I obtain the following expressions

$$\chi_{re,1} = -\frac{2N\mu_{ab}^2}{\hbar\epsilon_0} \operatorname{Re} \left[ \frac{\rho_{ab}}{\Omega_{ab}} \right],$$

$$\chi_{im,1} = -\frac{2N\mu_{ab}^2}{\hbar\epsilon_0} \operatorname{Im} \left[ \frac{\rho_{ab}}{\Omega_{ab}} \right],$$

$$\chi_{re,2} = -\frac{2N\mu_{ac}^2}{\hbar\epsilon_0} \operatorname{Re} \left[ \frac{\rho_{ac}}{\Omega_{ac}} \right],$$

$$\chi_{im,2} = -\frac{2N\mu_{ac}^2}{\hbar\epsilon_0} \operatorname{Im} \left[ \frac{\rho_{ac}}{\Omega_{ac}} \right],$$
(2.62)

and the expressions for the refraction indexes for each beam are

$$n_1 = 1 - \frac{N\mu_{ab}^2}{\hbar\epsilon_0} \operatorname{Re}\left[\frac{\rho_{ab}}{\Omega_{ab}}\right], \qquad (2.63)$$

$$n_2 = 1 - \frac{N\mu_{ac}^2}{\hbar\epsilon_0} \operatorname{Re}\left[\frac{\rho_{ac}}{\Omega_{ac}}\right], \qquad (2.64)$$

by substituting the expressions for the refractive indexes into the expression for the phase difference that the hybrid microwave-optical interferometer reads (Eq. 2.56), I obtain the following

$$\phi_1 - \phi_2 = k_m L - \frac{Nl}{\hbar \epsilon_0} \left( k_1 \mu_{ab}^2 \operatorname{Re} \left[ \frac{\rho_{ab}}{\Omega_{ab}} \right] - k_2 \mu_{ac}^2 \operatorname{Re} \left[ \frac{\rho_{ac}}{\Omega_{ac}} \right] \right) + (\phi_{E_1} - \phi_{E_2}), \qquad (2.65)$$

now by making use of the following relationships  $\mu_{nm}^2 = 3\pi\epsilon_0\hbar\gamma_{nm}/k_{nm}^3$  and  $\sigma_{nm} = 6\pi/k_{nm}^2$  were  $\gamma$  is the decay rate and  $\sigma$  is the cross section of interaction, I can rewrite the previous expression as

$$\phi_1 - \phi_2 = k_m L - \frac{Nl}{2} \left( \frac{k_1}{k_{ab}} \sigma_{ab} \gamma_{ab} \operatorname{Re} \left[ \frac{\rho_{ab}}{\Omega_{ab}} \right] - \frac{k_2}{k_{ac}} \sigma_{ac} \gamma_{ac} \operatorname{Re} \left[ \frac{\rho_{ac}}{\Omega_{ac}} \right] \right) + (\phi_{E_1} - \phi_{E_2}), \quad (2.66)$$

I will now make the following approximations,  $k_1$  is the wavenumber of the electric field  $E_1$ , while  $k_{ab}$  denotes the wavenumber of the  $a \leftrightarrow b$  transition, and similarly for  $k_2$  and

 $k_{ac}$ , I can write  $k_1$  as  $k_1 = k_{ab} + k_{\delta_{ab}}$ , where  $k_{\delta_{ab}}$  is the wavenumber of the detuning from the transition, and therefore the ratio  $k_1/k_{ab}$  is equal to  $1 + k_{\delta_{ab}}/k_{ab}$ , similarly for  $k_2/k_{ac}$ , the first approximation I make is  $k_1/k_{ab} \approx 1$  and  $k_2/k_{ac} \approx 1$  since the detuning I am considering it will be much smaller that an optical wavenumber. The next approximation I will make is to consider  $\sigma_{ab} \approx \sigma_{ac}$ , which is equivalent to making  $\sigma_{ab}/\sigma_{ac} \approx 1$ , if I write explicitly this ratio I obtain  $\sigma_{ab}/\sigma_{ac} = k_{ac}^2/k_{ab}^2$ , I can write  $k_{ac}$  as  $k_{ac} = k_{ab} + k_{cb}$ , where  $k_{cb}$  is the wavenumber of the rotational/vibrational transition between levels b and c, therefore  $\sigma_{ab}/\sigma_{ac} = k_{ac}^2/k_{ab}^2 \approx 1 + 2k_{cb}/k_{ab} \approx 1$  where again  $k_{cb}$  would be very small compared to  $k_{ab}$ , with these approximations in mind I rewrite the expression for the differential phase

$$\phi_1 - \phi_2 = k_m L - \frac{Nl\sigma}{2} \left( \gamma_{ab} \operatorname{Re} \left[ \frac{\rho_{ab}}{\Omega_{ab}} \right] - \gamma_{ac} \operatorname{Re} \left[ \frac{\rho_{ac}}{\Omega_{ac}} \right] \right) + (\phi_{E_1} - \phi_{E_2}), \qquad (2.67)$$

the  $k_mL$  term will be just normal oscillations in the signal but the second term contains the information about the system that I am looking for, so our focus will be on this second term. Substituting this expression for  $\phi_1 - \phi_2$  into the expression for the hybrid microwave-optical interferometer current Eq. 2.56 and considering only the term that we are interested in we obtain the following expression for the hybrid interferometer current

$$i_{\text{hybrid}} = -\frac{1}{2}RP'\beta Nl\sigma \left(\gamma_{ab}\text{Re}\left[\frac{\rho_{ab}}{\Omega_{ab}}\right] - \gamma_{ac}\text{Re}\left[\frac{\rho_{ac}}{\Omega_{ac}}\right]\right).$$
 (2.68)

## 2.3.3 Analytical approximations for the hybrid microwave-optical interferometer signal

In this section, I present some analytical approximations for the expression of the signal of the hybrid microwave-optical interferometer to better understand how the signal scales with the experimental parameters. The system is characterized by its optical Bloch equations that are derived in Appendix C and I present the complete solutions and some approximations of interest for the steady state in Appendix D. Figure 2.5 shows several graphs of the coherence terms normalized by the Rabi frequency as a function of the detuning of one of the beams  $(\delta_{ab})$ , the other beam is detuned by a fixed amount  $(\delta_{ac})$ . We can observe two distinct features happening simultaneously, one is the optical pumping, which is the wider curve centered around  $\delta_{ab} = 0$ , this curve is much wider than  $\gamma$  because it depends on a competition of the pumping coming from the two detuned beams and ends up having a width proportional to the detuning that I am keeping fixed (see Eq. D.5). The other is a much narrower feature that appears in resonance with a two-photon transition ( $\delta_{cb} = \delta_{ab} - \delta_{ac} = 0$ ). This specific point is associated with Electromagnetic-Induced Transparency (EIT) and is frequently represented as a dip in the excited-state population ( $\rho_{aa}$ ) [92, 90].

Here, instead, I graph the coherence terms since these are the parameters that will be measured in the proposed experimental configuration. Both terms exhibit a characteristic dispersive profile as they become zero precisely at the two-photon resonance point (Eq. D.2). I am interested in this specific dispersive behavior, because its presence is due to the formation of a compound molecule. I can obtain just the optical pumping behavior by considering an equilibrium between decay and excitation rates of two two-level systems that both share the same excited level  $|a\rangle$ , this condition can be expressed as

$$S_{ba}\rho_{bb} = S_{ab}\rho_{aa} + \gamma_{ab}\rho_{aa},$$

$$S_{ca}\rho_{cc} = S_{ac}\rho_{aa} + \gamma_{ac}\rho_{aa},$$
(2.69)

Where  $S_{i,a}$ , i = b, c is the rate of induced absorption from the i level to the a level,  $S_{a,i}$ , i = b, c is the rate of induced emission from the a level to the i level, the rates of induced absorption and emission for each of the transitions are equal, a fact that is well known from the Einstein coefficients for induced emission and absorption [93]. Considering the conservation of population between the three levels  $\rho_{aa} + \rho_{bb} + \rho_{cc} = 1$  as well as Eq. 2.69 we can obtain solutions for the populations of each level

$$\rho_{aa} = \frac{S_{ba}S_{ca}}{3S_{ba}S_{ca} + \gamma_{ac}S_{ba} + \gamma_{ab}S_{ca}},$$

$$\rho_{bb} = \frac{S_{ba}S_{ca} + \gamma_{ab}S_{ca}}{3S_{ba}S_{ca} + \gamma_{ac}S_{ba} + \gamma_{ab}S_{ca}},$$

$$\rho_{cc} = \frac{S_{ba}S_{ca} + \gamma_{ac}S_{ba}}{3S_{ba}S_{ca} + \gamma_{ac}S_{ba} + \gamma_{ab}S_{ca}},$$
(2.70)

The excitation rate  $S_{i,a}$  can be considered as the rate of photon dispersion, for each of the transitions, in a low-intensity approximation. This is because in the stationary state the rate of dispersion of light must also equal the rate of induced absorption, so the expression for each of the induced absorption rates is [49]

$$S_{i,a} \approx \gamma_{ai} \rho_{aa}^{(i)} \approx \frac{\gamma_{ai} |\Omega_{ai}|^2}{\gamma_{ai}^2 + 4\delta_{ai}^2}.$$
 (2.71)

Since I am considering a low-intensity case  $(\Omega < \gamma)$ , the excitation rate is pretty small compared to the decay rate  $(S < \gamma)$  this allows me to disregarding any term of the form  $S^2$ , since it will be the less dominant one, and considering a high-detuning scenario  $(\delta > \gamma)$  we obtain approximations for the expressions of the populations

$$\rho_{aa} \approx \frac{|\Omega_{ab}|^2 |\Omega_{ac}|^2}{4 \left( |\Omega_{ab}|^2 \delta_{ac}^2 + |\Omega_{ac}|^2 \delta_{ab}^2 \right)},$$

$$\rho_{bb} \approx \frac{|\Omega_{ac}|^2 \delta_{ab}^2}{|\Omega_{ab}|^2 \delta_{ac}^2 + |\Omega_{ac}|^2 \delta_{ab}^2},$$

$$\rho_{cc} \approx \frac{|\Omega_{ab}|^2 \delta_{ac}^2}{|\Omega_{ab}|^2 \delta_{ac}^2 + |\Omega_{ac}|^2 \delta_{ab}^2},$$

We can then approximate the expression for the coherence  $\rho_{ab} \approx \sqrt{\rho_{aa}\rho_{bb}}$  and  $\rho_{ac} \approx \sqrt{\rho_{aa}\rho_{cc}}$  to obtain

$$\rho_{ab}/\Omega_{ab} \approx \frac{|\Omega_{ac}|^2 \delta_{ab}}{2\left(|\Omega_{ab}|^2 \delta_{ac}^2 + |\Omega_{ac}|^2 \delta_{ab}^2\right)},$$

$$\rho_{ac}/\Omega_{ac} \approx \frac{|\Omega_{ab}|^2 \delta_{ac}}{2\left(|\Omega_{ab}|^2 \delta_{ac}^2 + |\Omega_{ac}|^2 \delta_{ab}^2\right)},$$
(2.73)

which, except for a sign that might be missing, are the same expression we obtained for the approximations of the complete solution Eq. D.4 with  $\gamma_{ab} = \gamma_{ac}$ .

Figure 2.6 shows a comparison of the coherences  $\rho_{ab}$  and  $\rho_{ac}$  for a three-level system for two cases, one is the complete description given by Eq. D.1 and the other one is only the optical pumping phenomena given by Eq. 2.73. The figure shows that both terms have the same optical-pumping curve, which means that these are similar for detunings far away from the two-photon dispersion zone, that is the narrow feature ( $|\delta_{cb}| > 0$ ).

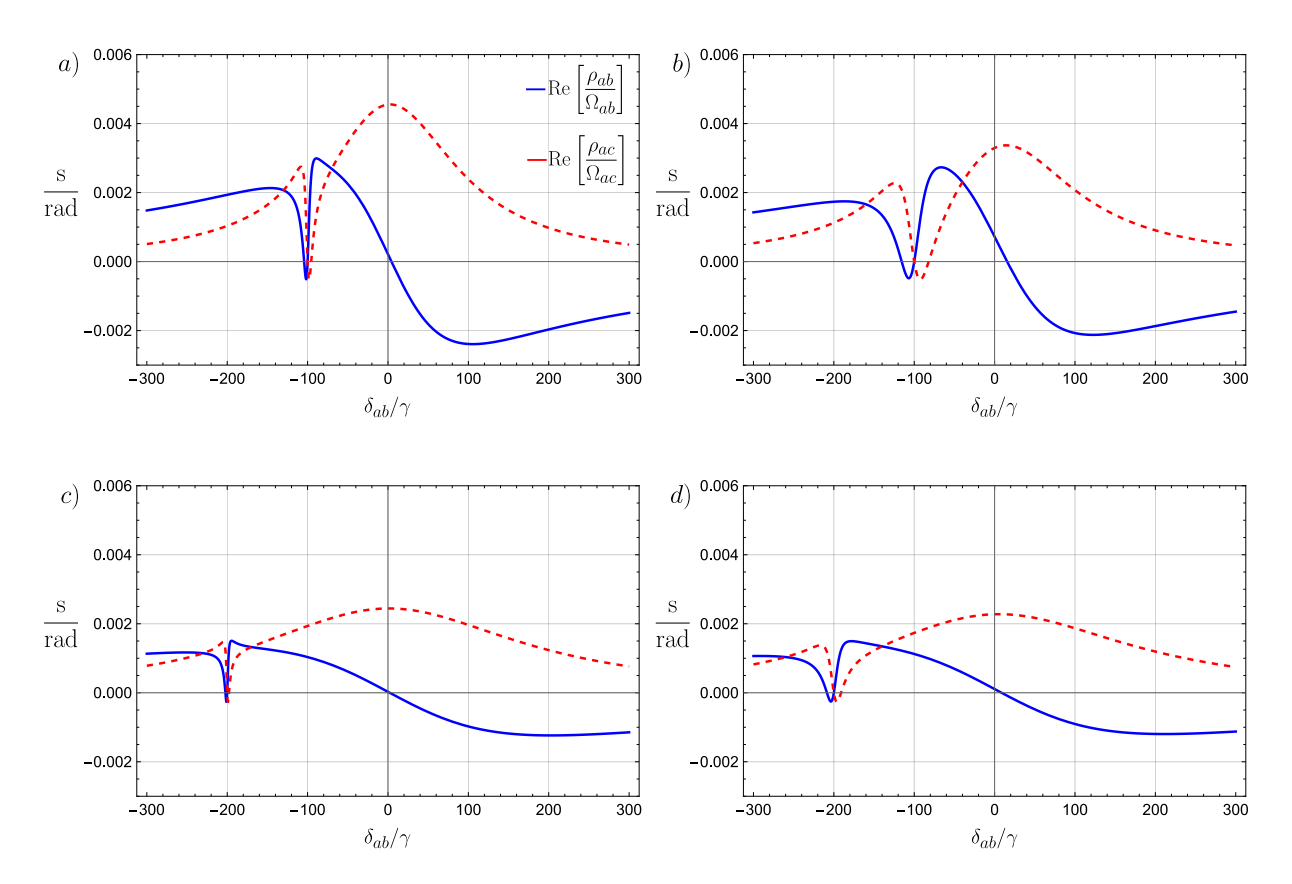


Figure 2.5: Plot of the real components of the coherence's  $\rho_{ab}/\Omega_{ab}$ , in solid blue, and  $\rho_{ac}/\Omega_{ac}$ , in dasehd red, as a function of the detuning of one of the beams  $(\delta_{ab}/\gamma)$  given by Eq. D.1. For all plots  $\gamma_{ab}=\gamma_{ac}=\gamma$  and  $\Omega_{ab}=\Omega_{ac}=\Omega$ . For a),  $\Omega=30\gamma$  and  $\delta_{ac}=-100\gamma$ . For b)  $\Omega=60\gamma$  and  $\delta_{ac}=-100\gamma$ . For c),  $\Omega=30\gamma$  and  $\delta_{ac}=-200\gamma$ . For d),  $\Omega=60\gamma$  and  $\delta_{ac}=-200\gamma$ .

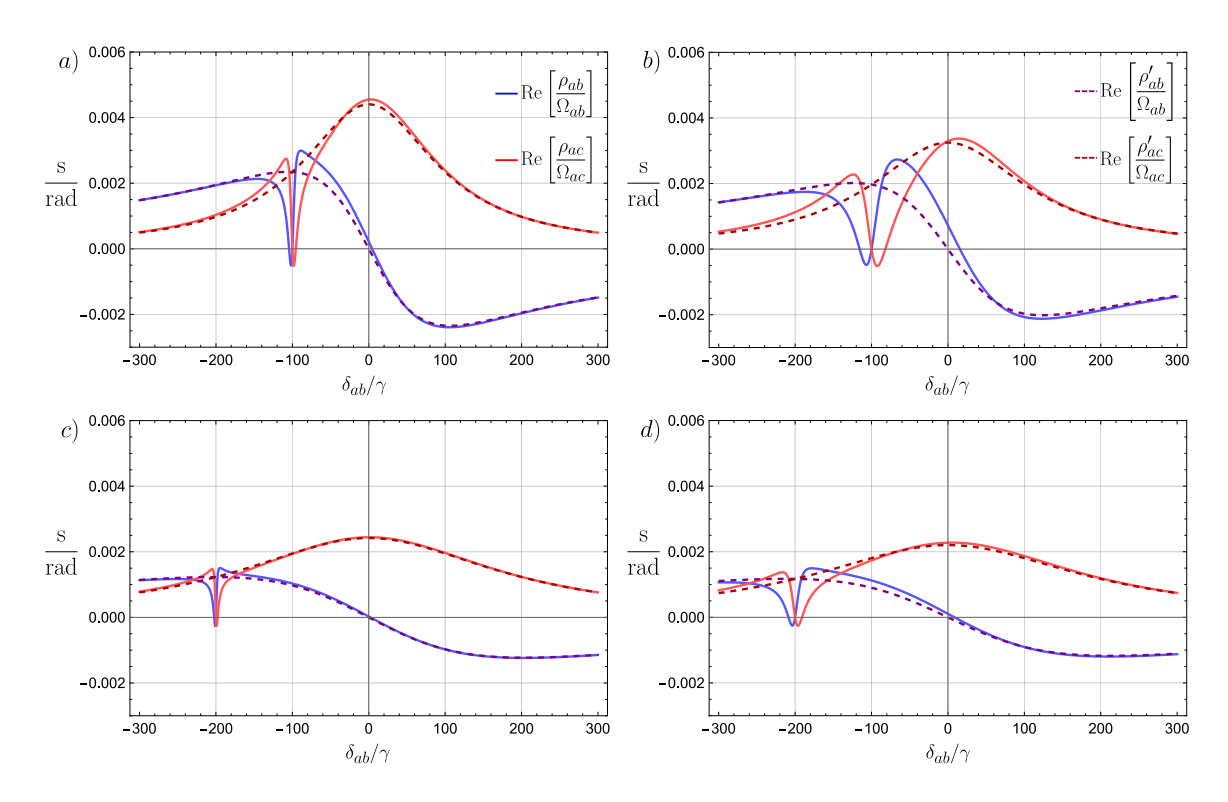


Figure 2.6: Plot of the real components of the coherence's  $\rho_{ab}/\Omega_{ab}$  and  $\rho_{ac}/\Omega_{ac}$  as a function of the detuning of one of the beams  $(\delta_{ab})$ . Solid lines are given by Eq. D.1, dashed lines are given by Eq. 2.73. For all plots  $\gamma_{ab} = \gamma_{ac} = \gamma$  and  $\Omega_{ab} = \Omega_{ac} = \Omega$ . For a,  $\Omega = 30\gamma$  and  $\delta_{ac} = -100\gamma$ . For b,  $\Omega = 60\gamma$  and  $\delta_{ac} = -100\gamma$ . For c,  $\Omega = 30\gamma$  and  $\delta_{ac} = -200\gamma$ . For d,  $\Omega = 60\gamma$  and  $\delta_{ac} = -200\gamma$ 

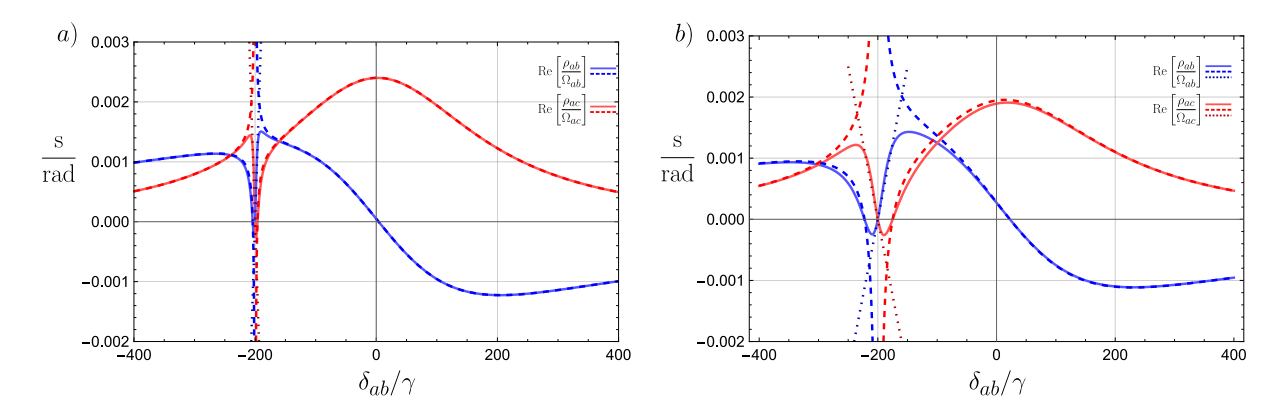


Figure 2.7: Plot of the real components of the coherence's  $\rho_{ab}/\Omega_{ab}$  (blue) and  $\rho_{ac}/\Omega_{ac}$  (red) as a function of the detuning of one of the beams  $(\delta_{ab}/\gamma)$ . Solid lines are the full solution (Eq. D.1), in blue  $\rho_{ab}$  and in red  $\rho_{ac}$ , dashed lines are the approximation detuned from the two-photon resonance (Eq. D.6) and dotted lines are the linear approximation at the two-photon resonance (Eq. D.2). At higher detunings both curves follow the envelope given by Eq. D.4. For both plots  $\gamma_{ab} = \gamma_{ac} = \gamma$ ,  $\Omega_{ab} = \Omega_{ac} = \Omega$  and  $\delta_{ac} = -200\gamma$ . For a)  $|\Omega| = 40\gamma$  and for b)  $|\Omega| = 100\gamma$ .

I will focus on the non-resonant case, once the particles have bonded and formed a compound molecule, there will be present the two-photon resonance, I express the solutions for the coherence terms ( $\rho_{ab}$  and  $\rho_{ac}$ ) under the assumption of a small decay rate ( $\gamma$ ) in comparison to the other parameters ( $\Omega$ ,  $\delta$ ).

By approximating the solutions for the coherence's (Eq. D.1) around the two-photon resonance ( $\delta_{cb} < \Omega$ ) I obtain (Eq. D.3)

$$\operatorname{Re}\left[\frac{\rho_{ab}}{\Omega_{ab}} - \frac{\rho_{ac}}{\Omega_{ac}}\right] = \frac{2\delta_{cb}}{|\Omega_{ab}|^2 + |\Omega_{ac}|^2},\tag{2.74}$$

with this approximation, the current detected in the hybrid microwave-optical interferometer becomes

$$i_{\text{hybrid}} = -RP'(Nl\sigma)\beta\gamma \frac{\delta_{cb}}{|\Omega_{ab}|^2 + |\Omega_{ac}|^2}.$$
 (2.75)

A comparison of the approximation and the full solution is depicted in Fig. 2.7 and Fig. 2.8a) which is basically the signal output from the hybrid interferometer except for a scaling factor, as it can be seen by Eq. 2.75. The width of the two-photon feature increases with the Rabi frequency, this is well known in the context of EIT [94]. Taking two beams that possess the same Rabi frequency  $(\Omega)$ , the width is proportional to  $|\Omega|^2$ . More details on the magnitude of the two-photon dispersion feature can be found in Appendix D (see also Fig. 2.9). As we deviate from the two-photon resonance ( $|\delta_{cb}| > 0$ ), the observed phase undergoes changes due to optical pumping between the energy levels (which corresponds to the broad dependence illustrated in Fig. 2.7), as well as the influence of the two-photon transition (depicted as a narrow feature in Fig. 2.7). Our main focus is on the latter effect. We came up with a way that allows us to isolate this effect by comparing measurements taken at two distinct power levels. In this scenario, the optical pumping remains constant, as it can be seen comparing Fig. 2.5 c) and Fig. 2.5 d); while the two-photon resonance increases in width, again see Figs. 2.5 c) and 2.5 d), becoming detectable at greater detunings from the two-photon resonance. By calculating the difference between the signals at high (denoted as subindex H, while still maintaining  $\Omega < \delta_{cb}$ ) and low (denoted as subindex L) powers, we derive (Eq. D.11)

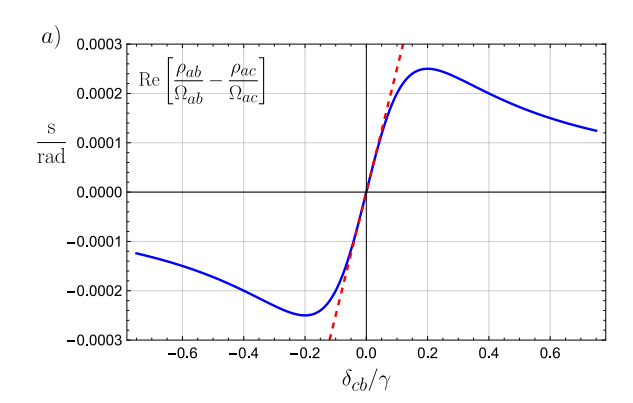
$$\operatorname{Re}\left[\frac{\rho_{ab}}{\Omega_{ab}} - \frac{\rho_{ac}}{\Omega_{ac}}\right]_{L}^{H} = \frac{(|\Omega_{ab,H}|^{2} + |\Omega_{ac,H}|^{2})^{2}}{8\delta_{cb}\left(|\Omega_{ab,H}|^{2}\delta_{ac}^{2} + |\Omega_{ac,H}|^{2}\delta_{ab}^{2}\right)},$$
(2.76)

and the current difference of the hybrid microwave-optical interferometer is

$$\Delta \left( \frac{i_{\text{hybrid}}}{P'} \right) = \frac{i_{\text{hybrid},H}}{P'_{H}} - \frac{i_{\text{hybrid},L}}{P'_{L}}$$

$$\Delta \left( \frac{i_{\text{hybrid}}}{P'} \right) = -R \left( Nl\sigma \right) \beta \left( \frac{\gamma}{16\delta_{cb}} \right) \frac{\left( |\Omega_{ab,H}|^2 + |\Omega_{ac,H}|^2 \right)^2}{\left( |\Omega_{ab,H}|^2 \delta_{ac}^2 + |\Omega_{ac,H}|^2 \delta_{ab}^2 \right)}.$$
(2.77)

A plot comparing the full solution and this approximation is presented in Fig.2.8b). The expression shows that we obtain a dependence as a function of the detuning with the two-photon transition proportional to  $\delta_{cb}^{-1}$ , which is the same dependence as in a single beam Mach-Zehnder interferometer with the optical detuning Eq. 2.44 [85, 61]. For comparison, take the case of a phase change measurement using a single beam in a Mach-Zehnder interferometer and two transitions, so that the detuning  $(\delta_{ab})$  is greater than



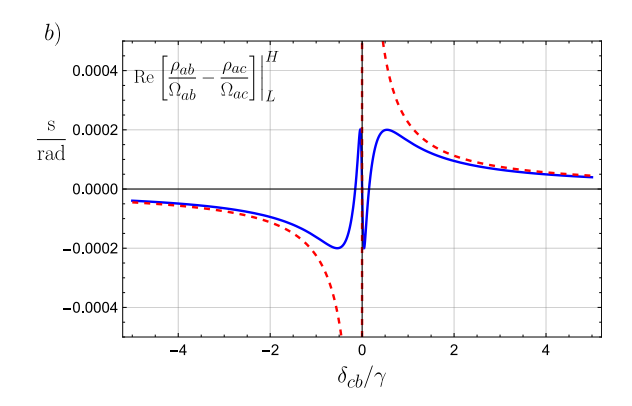


Figure 2.8: Plot of the real components of the differential normalized coherence's  $(\rho_{ab}/\Omega_{ab} - \rho_{ac}/\Omega_{ac})$  as a function of the two-photon detuning  $\delta_{cb}/\gamma$ . Solid blue lines are the full solution (Eq.D.1) and red dashed lines are the analytical approximations. In both graphs  $\gamma_{ab} = \gamma_{ac} = \gamma$  and  $\Omega_{ab} = \Omega_{ac} = \Omega$ . For a) in red Eq.D.3  $\Omega = 20\gamma$ ,  $\delta_{ab} \approx \delta_{ac} = 1000\gamma$ . For b) in red Eq.D.11  $\Omega_H = 30\gamma$  and  $\delta_{ab} \approx \delta_{ac} = 1000\gamma$ .

the separation between the two transitions ( $\omega_{bc}$ ). The current difference between the two transitions using Eq. 2.44 is

$$i_{\rm MZ} = (NRl\sigma) P \frac{\gamma}{8} \left( \frac{1}{\delta_{ab}} - \frac{1}{\delta_{ab} + \omega_{bc}} \right) \simeq (NRl\sigma) P \frac{\gamma \omega_{bc}}{8\delta_{ab}^2},$$
 (2.78)

which scales as  $\delta_{ab}^{-2}$ . So, the process of taking the difference of the non-resonant two-photon signal at different powers recovers a favorable dependence of  $\delta_{cb}^{-1}$ . Have I considered the case where the sample did not form a compound molecule, there will be no coherence between levels b and c, this will remove the two-photon feature in the signal, and with the difference between high and low power the resulting signal will be zero.

Usually, molecular resonances typically fall within the frequency domain of 10 to 100 THz for vibrational modes and from 100 GHz to 10 THz for rotational modes, and frequency modulators are effective up to 10 GHz, although there are specific exceptions that can achieve frequencies of up to 100 GHz [95]. This means that contemporary modulators struggle to reach the two-photon resonance, relying instead on a detuned two-photon detection method. This detuned detection yields a signal that represents the sum contributions of all resonances, each weighted according to their respective detuning, which is advantageous when there is no prior knowledge regarding the position of a specific resonance. This approach is in contrast to resonant detection, which responds primarily to the nearest resonance.

Consider a sample without Doppler broadening; it has an optical density (absorption cross section) given by  $OD = Nl\sigma$  [49]. We can calibrate this number by performing a standard absorption measurement (Eq. 2.21). By taking the difference between the maximum and minimum values of the signal current around the two-photon resonance (see Fig. 2.9), we obtain the maximum size of the phase difference measured in the hybrid microwave-optical interferometer, and by working on an analytical approximation we obtain (Eq. D.18)

$$(\phi_1 - \phi_2)|_{\delta_{cb,min}}^{\delta_{cb,max}} \simeq \text{OD}\frac{\gamma}{2|\delta|},$$
 (2.79)

which scales as  $|\delta|^{-1}$  with the one-photon detuning. In a more realistic scenario, the experimentalists have two possible parameters that they can change in order to obtain a

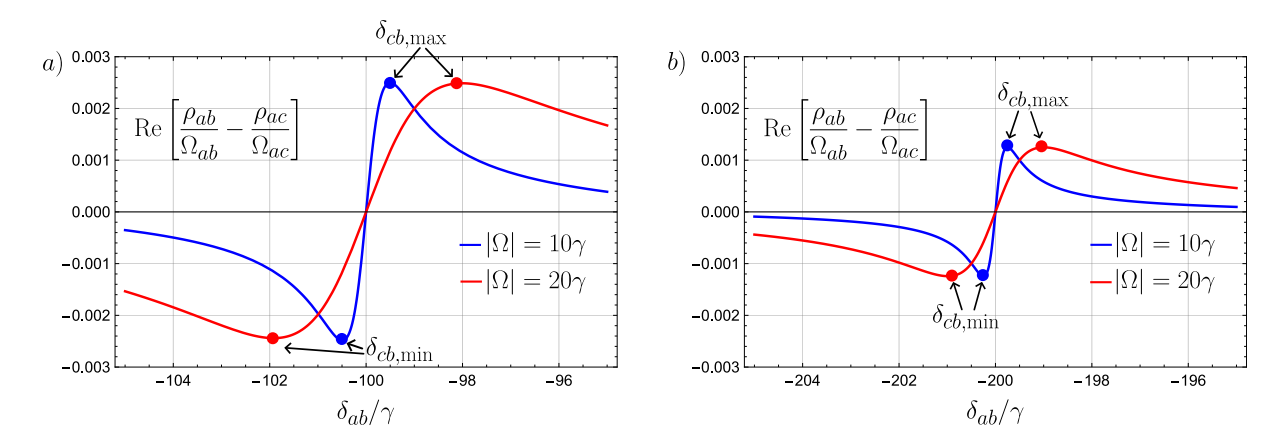


Figure 2.9: Plot of the real part of the difference of coherences normalized by their corresponding Rabi frequency as a function of the one-photon detuning  $\delta_{ab}/\gamma$ . The graph is centered around the two-photon resonance  $\delta_{cb} = 0 = \delta_{ab} - \delta_{ac}$ . For both graphs  $\Omega_{ab} = \Omega_{ac} = \Omega$  and  $\gamma_{ab} = \gamma_{ac} = \gamma$ . For a)  $\delta_{ac} = 100\gamma$ , in blue  $|\Omega| = 10\gamma$  and in red  $|\Omega| = 20\gamma$ . For b)  $\delta_{ac} = 200\gamma$ , in blue  $|\Omega| = 10\gamma$  and in red  $|\Omega| = 20\gamma$ .

measurement, those are the laser frequency  $\omega_l$  and the modulation frequency  $\omega_m$ . Figure 2.10 is the graph for the phase difference  $(\phi_1 - \phi_2)$  for these two parameters, the size of the phase difference is represented as a color level in a two-dimensional plane. I have also included several regions delimited by red dashed lines and blue dot-dashed lines. The area inside the red dashed lines represents values for the parameters that are less than the decay rate  $\gamma$ , the points inside this zone must be avoided since they are parameters where there is a strong resonant response of the system and the proposed design does not operate in resonance. The points inside the dot-dashed blue lines are values of the parameters that are less than the Rabi frequency, these zones do not particularly have to be excluded; however, they represent areas where the best suited analytical approximation for the signal is the one close to resonance (Eq. 2.75 for example) these zone still may be out of reach for the experimentalist, unless in a high-intensity case. Lastly, the area outside the dot-dashed blue lines represents the values of the parameters that are greater than the Rabi frequency and the decay rate, this is where the hybrid interferometer is most likely to operate, and this graph may be helpful in obtaining a set of parameters in order to optimize the signal of the hybrid interferometer, as one can see from the graph, there is a zone of large signal around  $\delta_{ac} = 10\gamma$  and  $\omega_{cb} = 10\gamma$  just outside the region delimited by the dot-dashed blue lines. There is a similar zone, but with reverse sign, mirrored at higher modulation frequencies, but this zone involves being able to modulate above the two-photon transition, I have previously discussed that this would be almost impossible to reach due to technical limitations of the modulators. Although Fig. 2.10 might seem a little dense in information, one can obtain a similar curve to that of Fig. 2.9 by keeping one parameter fixed, say  $\delta_{ac}$ , and scanning the other one  $(\omega_m)$ , doing so means moving vertically in Fig. 2.10 at a particular value for  $\delta_{ac}$ .

To end this chapter, I gather all of the expressions that I have obtained so far for all of the methods we have previously discussed. For each of the listed methods, the first expression that appears is the most general one, without explicitly working the dependence with external parameters or choosing a specific scenario, however this first expression shows weather the method measures population of a state or coherence between states, the second expression that appears is for an explicit case, and it shows the dependence

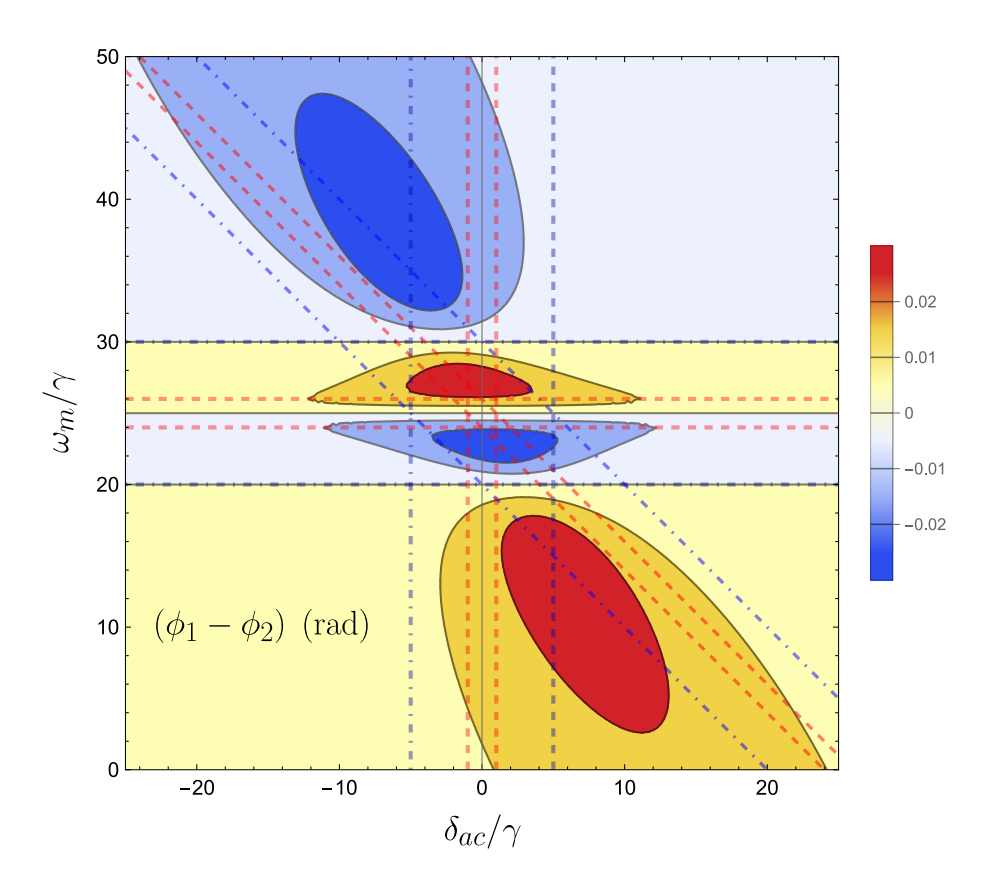


Figure 2.10: Phase difference  $(\phi_1 - \phi_2)$ , with an OD = 1, as a function of two parameters,  $\delta_{ac}$ , which is the detunining of the non-modulated laser with respect to the  $a \leftrightarrow c$  transition, and modulation frequency  $\omega_m$ . For this graph  $\gamma_{ab} = \gamma_{ac} = \gamma$ ,  $\Omega_{ac} = \Omega_{ab} = \Omega = 5\gamma$ , and the two-photon transition frequency  $\omega_{cb} = 25\gamma$ .

of the signal current with experimental parameters.

Fluorescence: 
$$i_{\rm f} = RP(Nl\sigma)\eta\gamma^2 \frac{\rho_{aa}}{|\Omega_{ab}|^2}; \quad i_{\rm f} = RP(Nl\sigma)\eta C_D.$$
 (2.80)

Absorption: 
$$i_{\rm a} = RP(Nl\sigma)\gamma^2 \frac{\rho_{aa}}{|\Omega_{ab}|^2}; \quad i_{\rm a} = RP(Nl\sigma)C_D.$$
 (2.81)

Phase change: 
$$i_{\text{phase}} = \frac{1}{2} RP(Nl\sigma) \gamma \text{Re} \left[ -\frac{\rho_{ab}}{\Omega_{ab}} \right]; \quad i_{\text{phase}} = \frac{1}{2} RP(Nl\sigma) \frac{\gamma}{2\delta}.$$
 (2.82)

Hybrid Int.: 
$$i_{\text{hybrid}} = -RP'\beta \frac{(Nl\sigma)}{2} \left( \gamma_{ab} \text{Re} \left[ \frac{\rho_{ab}}{\Omega_{ab}} \right] - \gamma_{ac} \text{Re} \left[ \frac{\rho_{ac}}{\Omega_{ac}} \right] \right);$$
 (2.83)

$$\Delta \left( \frac{i_{\text{hybrid}}}{P'} \right) = -R \left( N l \sigma \right) \beta \left( \frac{\gamma}{16 \delta_{cb}} \right) \frac{\left( |\Omega_{ab,H}|^2 + |\Omega_{ac,H}|^2 \right)^2}{\left( |\Omega_{ab,H}|^2 \delta_{ac}^2 + |\Omega_{ac,H}|^2 \delta_{ab}^2 \right)}. \tag{2.84}$$

We can observe that in all expressions the factor  $Nl\sigma = OD$  is common among them. This is an indication that the main phenomenon behind the detection is the interaction with light. However, in great contrast to the traditional methods, the signal current for the hybrid microwave-optical scales with the detuning in the microwave domain  $(\delta_{cb})$  while the traditional methods scale with an optical detuning. This shows that the proposed interferometer clearly is 'hybrid' in its nature because of the strong response with an optical phenomena but a scaling with a microwave parameter.

#### 2.4 Conclusions

This part of my thesis expands on a previous work in which they analyzed several common detection methods for atoms or molecules, and introduced a new detection method for molecular interactions. This method employs coherent excitation using two lasers and measures the relative phase shift of the beams after passing through a sample using a hybrid microwave-optical interferometer. The hybrid interferometer features one arm operating in the optical regime, which facilitates a strong response in the sample via two-photon excitation, while also benefiting from the interferometric stability found operating in the microwave domain. The proposed method utilizes two distinct frequencies and performs a non-resonant detection, a category that currently has very few existing methods. This hybrid microwave-optical interferometer is notably resistant to external phase fluctuations, such as those caused by temperature changes, which is often a significant challenge in interferometric measurements. To compare this method with more traditional ones, I managed to obtain expressions for the signal current for all methods and unify their dependence under the common experimental parameters, this enhances the similarities and differences between them. The signal current of all methods is proportional to the cross section of the light-matter interaction, the sample length, molecular density, detector responsivity, and incident beam power. In addition, the hybrid interferometer depends on the one- and two-photon detunings. We demonstrate that our method exhibits advantageous scaling with experimental parameters such as the two-photon detuning and power, making it a suitable choice for detecting molecular interactions.

### Bibliography

- [1] A. A. Michelson and E. W. Morley, "On the relative motion of the earth and the luminiferous ether," *American Journal of Science*, vol. s3-34, no. 203, pp. 333–345, 11 1887.
- [2] M. Kasevich and S. Chu, "Atomic interferometry using stimulated raman transitions," *Phys. Rev. Lett.*, vol. 67, pp. 181–184, Jul 1991. [Online]. Available: https://link.aps.org/doi/10.1103/PhysRevLett.67.181
- [3] F. Riehle, T. Kisters, A. Witte, J. Helmcke, and C. Borde, "Optical ramsey spectroscopy in a rotating frame: Sagnac effect in a matter-wave interferometer," *Phys. Rev. Lett.*, vol. 67, p. 177, 1991.
- [4] R. Geiger, A. Landragin, S. Merlet, and F. P. D. Santos, "High-accuracy inertial measurements with cold-atom sensors," AVS Quantum Science, vol. 2, p. 024702, 2020.
- [5] A. Peters, K. Y. Chung, and S. Chu, "High-precision gravity measurements using atom interferometry," *Metrologia*, vol. 38, 2001.
- [6] V. Ménoret, P. Vermeulen, N. Le Moigne, S. Bonvalot, P. Bouyer, A. Landragin, and B. Desruelle, "Gravity measurements below 10 9 g with a transportable absolute quantum gravimeter," *Sci. Rep.*, vol. 8, no. 1, pp. 0–11, 2018.
- [7] V. Xu, M. Jaffe, C. D. Panda, S. L. Kristensen, L. W. Clark, and H. Müller, "Probing gravity by holding atoms for 20 seconds," *Science*, vol. 366, p. 745, 2019.
- [8] M. J. M., F. G. T., J. B. Fixler, M. J. Snadden, and M. A. Kasevich, "Sensitive absolute-gravity gradiometry using atom interferometry," *Phys. Rev. A*, vol. 65, p. 033608, Feb 2002. [Online]. Available: https://link.aps.org/doi/10.1103/PhysRevA.65.033608
- [9] B. Stray, A. Lamb, A. Kaushik, J. Vovrosh, A. Rodgers, J. Winch, F. Hayati, D. Boddice, A. Stabrawa, A. Niggebaum, M. Langlois, Y.-H. Lien, S. Lellouch, S. Roshanmanesh, K. Ridley, G. de Villiers, G. Brown, T. Cross, G. Tuckwell, A. Faramarzi, N. Metje, K. Bongs, and M. Holynski, "Quantum sensing for gravity cartography," *Nature*, vol. 602, p. 590, February 2022.
- [10] T. L. Gustavson, A. Landragin, and M. A. Kasevich, "Rotation sensing with a dual atom-interferometer sagnac gyroscope," *Classical and Quantum Gravity*, vol. 17, p. 2385–2398, 2000.
- [11] B. Barrett, P. Cheiney, B. Battelier, F. Napolitano, and P. Bouyer, "Multidimensional atom optics and interferometry," *Phys. Rev. Lett.*, vol. 122, p. 043604, February 2019.

- [12] S. M. Dickerson, J. M. Hogan, A. Sugarbaker, D. M. S. Johnson, and M. A. Kasevich, "Multiaxis inertial sensing with long-time point source atom interferometry," *Phys. Rev. Lett.*, vol. 111, p. 083001, August 2013.
- [13] R. Bouchendira, P. Cladé, S. Guellati-Khélifa, F. Nez, and F. Biraben, "New determination of the fine structure constant and test of the quantum electrodynamics," *Phys. Rev. Lett.*, vol. 106, p. 080801, 2011.
- [14] R. H. Parker, C. Yu, W. Zhong, B. Estey, and H. Müller, "Measurement of the fine-structure constant as a test of the standard model," *Science*, vol. 360, p. 191, 2018.
- [15] G. Rosi, F. Sorrentino, L. Cacciapuoti, M. Prevedelli, and G. M. Tino, "Precision measurement of the newtonian gravitational constant using cold atoms," *Nature*, vol. 510, pp. 518–521, 2014.
- [16] J. B. Fixler, G. T. Foster, J. M. McGuirk, and M. A. Kasevich, "Atom interferometer measurement of the newtonian constant of gravity," *Science*, vol. 315, p. 74, 2007.
- [17] B. Barrett, L. Antoni-Micollier, L. Chichet, B. Battelier, P.-A. Gominet, A. Bertoldi, P. Bouyer, and A. Landragin, "Correlative methods for dual-species quantum tests of the weak equivalence principle," New. J. Phys., vol. 17, p. 085010, 2015.
- [18] M. G. Tarallo, T. Mazzoni, N. Poli, D. V. Sutyrin, X. Zhang, and G. M. Tino, "Test of einstein equivalence principle for 0-spin and half-integer-spin atoms: Search for spin-gravity coupling effects," *Phys. Rev. Lett.*, vol. 113, p. 023005, 2014.
- [19] G. M. Tino, "Testing gravity with cold atom interferometry: results and prospects," *Quantum Science and Technology*, vol. 6, 2021.
- [20] B. Canuel and L. e. a. Bertoldi, A.and Amand, "Exploring gravity with the migal large scale atom interferometer," Sci. Rep., 2018.
- [21] Q. Beaufils1, L. A. Sidorenkov, P. Lebegue, B. Venon, D. Holleville, L. Volodimer, M. Lours, J. Junca, X. Zou, A. Bertoldi, M. Prevedelli, D. O. Sabulsky, P. Bouyer, A. Landragin, B. Canuel, and R. Geiger, "Cold-atom sources for the matter-wave laser interferometric gravitation antenna (miga)," Sci. Rep., vol. 12, p. 19000, 2022.
- [22] K. Tim, H. J. M., S. Alex, D. S. M., C. A. Donnelly, O. Chris, and K. M. A., "Matter wave lensing to picokelvin temperatures," *Phys. Rev. Lett.*, vol. 114, p. 143004, Apr 2015. [Online]. Available: https://link.aps.org/doi/10.1103/PhysRevLett.114.143004
- [23] M. A. et al., "Matter-wave atomic gradiometer interferometric sensor (magis-100)," *Quantum Sci. Technol.*, 2021.
- [24] M. Schmidt, A. Senger, C. F. M. Hauth, V. Schkolnik, and A. Peters, "A mobile high-precision absolute gravimeter based on atom interferometry," *Gyroscopy and Navigation*, vol. 2, pp. 170–177, 2011.
- [25] Z.-K. Hu, B.-L. Sun, X.-C. Duan, M.-K. Zhou, L.-L. Chen, S. Zhan, Q.-Z. Zhang, and J. Luo, "Demonstration of an ultrahigh-sensitivity atom-interferometry absolute gravimeter," *Phys. Rev. A*, vol. 88, p. 043610, Oct 2013. [Online]. Available: https://link.aps.org/doi/10.1103/PhysRevA.88.043610

- [26] X. Wu, Z. Pagel, B. S. Malek, T. H. Nguyen, F. Zi, D. S. Scheirer, and H. Müller, "Gravity surveys using a mobile atom interferometer," *Science Advances*, vol. 5, no. 9, p. eaax0800, 2019.
- [27] S. Kulas, C. Vogt, A. Resch, J. Hartwig, S. Ganske, J. Matthias, D. Schlippert, T. Wendrich, W. Ertmer, E. M. Rasel, M. Damjanic, P. Weßels, A. Kohfeldt, E. Luvsandamdin, M. Schiemangk, C. Grzeschik, M. Krutzik, A. Wicht, A. Peters, S. Herrmann, and C. Lämmerzahl, "Miniaturized lab system for future cold atom experiments in microgravity," *Microgravity Science and Technology*, vol. 29, pp. 37–48, 2017.
- [28] S. wey Chiow and N. Yu, "Compact atom interferometer using single laser," *Applied Physics B*, vol. 124, 2018.
- [29] Y. Bidel, N. Zahzam, A. Bresson, C. Blanchard, M. Cadoret, A. V. Olesen, and R. Forsberg, "Absolute airborne gravimetry with a cold atom sensor," *J. Geodesy*, vol. 94, p. 20, 2020.
- [30] J. Lee, R. Ding, J. Christensen, R. R. Rosenthal, A. Ison, D. P. Gillund, D. Bossert, K. H. Fuerschbach, W. Kindel, P. S. Finnegan, J. R. Wendt, M. Gehl, A. Kodigala, H. McGuinness, C. A. Walker, S. A. Kemme, A. Lentine, G. Biedermann, and P. D. D. Schwindt, "A compact cold-atom interferometer with a high data-rate grating magneto-optical trap and a photonic-integrated-circuit-compatible laser system," Nat. Commun., vol. 13, p. 5131, 2022.
- [31] X. Zhang, J. Zhong, B. Tang, X. Chen, L. Zhu, P. Huang, J. Wang, and M. Zhan, "Compact portable laser system for mobile cold atom gravimeters," *Appl. Optics*, vol. 57, p. 6545, 2018.
- [32] Q. Luo, H. Zhang, K. Zhang, X.-C. Duan, Z.-K. Hu, L.-L. Chen, and M.-K. Zhou, "A compact laser system for a portable atom interferometry gravimeter," *Rev. Sci. Instrum.*, vol. 90, p. 043104, 2019.
- [33] A. López-Vázquez, M. Maldonado, E. Gomez, N. Corzo, E. de Carlos-López, A. F. Villafañe, K. Jiménez-García, J. Jiménez-Mier, J. López-González, C. López-Monjaraz, J. López-Romero, A. M. Herrera, R. Méndez-Fragoso, C. Ortiz, H. Peña, J. R. Borbolla, F. R. Martínez, and V. Valenzuela, "Compact laser modulation system for a transportable atomic gravimeter," Opt. Express, vol. 31, p. 3504, 2023.
- [34] A.-M. L., C. D., M. V., L.-G. J., K. T., and G. F. et al., "Detecting volcano-related underground mass changes with a quantum gravimeter." *Geophysical Research Letters*, 2022.
- [35] H. J.M. and D. D. S. e. a. Johnson, "An atomic gravitational wave interferometric sensor in low earth orbit (agis-leo)," *Gen Relativ Gravit*, 2011.
- [36] V. Schkolnik, B. Leykauf, M. Hauth, C. Freier, and A. Peters, "The effect of wavefront aberrations in atom interferometry," *Applied Physics B*, vol. 120, p. 311–316, 2015.
- [37] B. Cheng, Z. Wang, B. Wu, A. Xu, Q. Wang, and Q. Lin, "The effects of the non-uniformity of raman laser beams on an atom interferometer," *Eur. Phys. J. D*, vol. 68, p. 343, 2014.

- [38] M. Zhou, Q. Luo, L. Chen, X. Duan, and Z. Hu, "Observing the effect of wave-front aberrations in an atom interferometer by modulating the diameter of raman beams," *Phys. Rev. A*, vol. 93, p. 043610, 2016.
- [39] Y. Bidel, N. Zahzam, C. Blanchard, A. Bonnin, M. Cadoret, A. Bresson, D. Rouxel, and M. Lequentrec-Lalancette, "Absolute marine gravimetry with matter-wave interferometry," *Nat. Commun.*, vol. 9, p. 627, 2018.
- [40] H. Zhang, X. Ren, W. Yan, Y. Cheng, H. Zhou, Z. Gao, Q. Luo, M. Zhou, and Z. Hu, "Effects related to the temperature of atoms in an atom interferometry gravimeter based on ultra-cold atoms," *Opt. Express*, vol. 29, no. 19, pp. 30 007–30 019, Sep 2021. [Online]. Available: https://opg.optica.org/oe/abstract.cfm?URI=oe-29-19-30007
- [41] A. Trimeche, M. Langlois, and S. M. . P. D. Santos, "Active control of laser wavefronts in atom interferometers," *Physical Review Applied*, vol. 7, p. 034016, 2017.
- [42] R. Karcher, A. Imanaliev, S. Merlet, , and F. P. D. Santos, "Improving the accuracy of atom interferometers with ultracold sources," New J. Phys., vol. 20, p. 113041, 2018.
- [43] Y. Luo, J. You, Y. Li, Q. Hu, M. Ma, J. Wang, and F. Xu, "A general method for evaluation of effective Raman wavefront and phase shift in atom interferometry," in *Optical Manipulation and Structured Materials Conference 2020*, T. Omatsu, K. Dholakia, H. Ishihara, and K. Sasaki, Eds., vol. 11522, International Society for Optics and Photonics. SPIE, 2020, p. 115220D. [Online]. Available: https://doi.org/10.1117/12.2573801
- [44] N. Mielec, M. Altorio, S. Ranjita Chanu, D. Horville, D. Holleville, L. Sidorenkov, A. Landragin, and R. Geiger, "Atom interferometry with top-hat laser beams," Applied Physics Letters, vol. 113, p. 161108, 10 2018.
- [45] A. López, Y. Torres, M. Billión, W. Pimenta, J. Franco-Villafañe, and E. Gomez, "Experimental generation of a flat-top beam profile in a stable ring cavity," Opt. Lett., vol. 44, p. 4428, August 2019.
- [46] J. Cervantes, M. Maldonado, J. Franco-Villafañe, T. Roach, V. Valenzuela, and E. Gomez, "Selection of a raman beam waist in atomic gravimetry," OSA Contin., vol. 4, p. 1996, 2021.
- [47] P.-W. Huang, B. Tang, X. Chen, J.-Q. Zhong, Z.-Y. Xiong, L. Zhou, J. Wang, and M.-S. Zhan, "Accuracy and stability evaluation of the 85rb atom gravimeter wag-h5-1 at the 2017 international comparison of absolute gravimeters," *Metrologia*, vol. 56, no. 4, p. 045012, jul 2019. [Online]. Available: https://dx.doi.org/10.1088/1681-7575/ab2f01
- [48] Y.-Y. Xu, J.-F. Cui, K. Qi, L.-L. Chen, X.-B. Deng, Q. Luo, H. Zhang, Y.-J. Tan, C.-G. Shao, M.-K. Zhou, X.-C. Duan, and Z.-K. Hu, "Evaluation of the transportable atom gravimeter hust-qg," *Metrologia*, vol. 59, no. 5, p. 055001, aug 2022. [Online]. Available: https://dx.doi.org/10.1088/1681-7575/ac8258
- [49] P. v. d. S. Harold J. Metcalf, Laser cooling and trapping. Springer, 1999.
- [50] J. J. Sakurai, Modern quantum mechanics. Addison-Wesley Pub. Co, 1994.

- [51] N. Arias, V. Abediyeh, S. Hamzeloui, and E. Gomez, "Low phase noise beams for raman transitions with a phase modulator and a highly birefringent crystal," *Optics Express*, vol. 25, p. 5290, 2017.
- [52] Q. Hu, Y. Luo, A. Jia, C. Wei, S. Yan, and J. Yang, "Scheme for suppressing atom expansion induced contrast loss in atom interferometers," *Opt. Commun.*, vol. 390, p. 111, 2017.
- [53] A. Louchet-Chauvet, T. Farah, Q. Bodart, A. Clairon, A. Landragin, S. Merlet, and F. P. D. Santos, "The influence of transverse motion within an atomic gravimeter," New J. Phys., vol. 13, p. 065025, 2011.
- [54] J. E. Debs, P. A. Altin, T. H. Barter, D. Döring, G. R. Dennis, G. McDonald, R. P. Anderson, J. D. Close, and N. P. Robins, "Cold-atom gravimetry with a bose-einstein condensate," *Phys. Rev. A*, vol. 84, p. 033610, Sep 2011. [Online]. Available: https://link.aps.org/doi/10.1103/PhysRevA.84.033610
- [55] A. Humphrey and C. Campbell, "Fresnel diffraction of gausian laser beams by circular apertures," *Optical Engineering*, vol. 26(3), p. 263270, 1987.
- [56] B. E. A. Saleh and M. C. Teich, Fundamentals of Photonics, Second Edition, ser. Wiley Series in pure and applied Optics. Wiley, 2005.
- [57] E. Hecht, *Optics*, ser. Always learning. Pearson, 2016. [Online]. Available: https://books.google.com.mx/books?id=Bv1RrgEACAAJ
- S. [58] S. Bade, L. Djadaojee, Μ. Andia, Р. Cladé, and Guellati-"Observation of extra photon recoil in a distorted optical field," Khelifa, Rev. Lett., vol. 121, p. 073603, Aug 2018. [Online]. Available: https://link.aps.org/doi/10.1103/PhysRevLett.121.073603
- [59] S. Feng and H. G. Winful, "Physical origin of the gouy phase shift," Opt. Lett., vol. 26, p. 485, April 2001.
- [60] J. M. Cervantes and E. Gomez, "Effect of an aperture in atomic gravimetry," J. Opt. Soc. Am. A, vol. 41, no. 5, pp. 881–891, May 2024. [Online]. Available: https://opg.optica.org/josaa/abstract.cfm?URI=josaa-41-5-881
- [61] J. M. Cabello, "Caracterizacion de se nales de procesos de transicion atomicos," Master's thesis, Universidad de las Americas Puebla, 2021.
- [62] G. Gauglitz, "Abc spotlight on single-molecule detection," *Analytical and Bioanalytical Chemistry*, vol. 412, no. 26, pp. 7043–7045, Oct 2020.
- [63] N. Chauhan, K. Saxena, and U. Jain, "Single molecule detection; from microscopy to sensors," *International Journal of Biological Macromolecules*, vol. 209, pp. 1389– 1401, Jun 2022.
- [64] M. Hattori, K. Yamada, and H. Suzuki, "Plasma resonance absorption in thin metal films," *Journal of the Physical Society of Japan*, vol. 18, no. 2, pp. 203–206, Feb 1963. [Online]. Available: https://doi.org/10.1143/JPSJ.18.203

- "Laser-raman spectroscopic study of egg |65| R.Mendelsohn, lecithin lecithin-cholesterol mixtures," Biochimicaet Biophysica Actavol. 290, 15-21, 1972. [Online]. Available: pp. https://www.sciencedirect.com/science/article/pii/0005273672900478
- [66] D. Τ. P. Burghardt, and N. L. "Total Axelrod, Thompson, influorescence," AnnualReviewofternal reflection Biophysics, vol. 13. Volume 13. 1984, 247-268, 1984. [Online]. Available: pp. https://www.annualreviews.org/content/journals/10.1146/annurev.bb.13.060184.001335
- [67] D. R. Walt, T. M. Blicharz, and R. B. e. Hayman, "Microsensor arrays for saliva diagnostics," Annals of the New York Academy of Sciences, vol. 1098, no. 1, pp. 389–400, Mar 2007.
- [68] H. H. Hopkins and N. S. Kapany, "A flexible fibrescope, using static scanning," *Nature*, vol. 173, no. 4392, pp. 39–41, Jan 1954. [Online]. Available: https://doi.org/10.1038/173039b0
- [69] L. Rayleigh, "Ix. further applications of bessel's functions of high order to the whispering gallery and allied problems," *The London, Edinburgh, and Dublin Philosophical Magazine and Journal of Science*, vol. 27, no. 157, pp. 100–109, Jan 1914. [Online]. Available: https://doi.org/10.1080/14786440108635067
- [70] T. Förster, "Zwischenmolekulare energiewanderung und fluoreszenz," Annalen der Physik, vol. 437, no. 1-2, pp. 55–75, 1948. [Online]. Available: https://onlinelibrary.wiley.com/doi/abs/10.1002/andp.19484370105
- [71] W. Denk, J. H. Strickler, and W. W. Webb, "Two-photon laser scanning fluorescence microscopy," *Science*, vol. 248, no. 4951, pp. 73–76, 1990. [Online]. Available: https://www.science.org/doi/abs/10.1126/science.2321027
- [72] D. R. Walt, "Optical methods for single molecule detection and analysis," *Analytical Chemistry*, vol. 85, no. 3, pp. 1258–1263, Feb 2013. [Online]. Available: https://doi.org/10.1021/ac3027178
- [73] M. A. Cooper, "Label-free screening of bio-molecular interactions," *Anal Bioanal Chem*, vol. 377, no. 5, pp. 834–842, aug 2003.
- [74] W. U. Wang, C. Chen, and K. hui Lin *et al.*, "Label-free detection of small-molecule–protein interactions by using nanowire nanosensors," *Proceedings of the National Academy of Sciences*, vol. 102, no. 9, pp. 3208–3212, 2005. [Online]. Available: https://www.pnas.org/doi/abs/10.1073/pnas.0406368102
- [75] R. Peltomaa, B. Glahn-Martínez, and E. e. Benito-Peña, "Optical biosensors for label-free detection of small molecules," *Sensors*, vol. 18, no. 12, 2018. [Online]. Available: https://www.mdpi.com/1424-8220/18/12/4126
- [76] A. Chieng, Z. Wan, and S. Wang, "Recent advances in real-time label-free detection of small molecules," *Biosensors*, vol. 14, no. 2, 2024. [Online]. Available: https://www.mdpi.com/2079-6374/14/2/80
- [77] P. Fechner, O. Bleher, and M. e. Ewald, "Size does matter! label-free detection of small molecule-protein interaction," *Anal Bioanal Chem*, vol. 406, no. 17, pp. 4033–4051, may 2014.

- [78] J. Su, A. F. Goldberg, and B. M. Stoltz, "Label-free detection of single nanoparticles and biological molecules using microtoroid optical resonators," *Light: Science & Applications*, vol. 5, no. 1, pp. e16 001–e16 001, Jan 2016. [Online]. Available: https://doi.org/10.1038/lsa.2016.1
- [79] S. Subramanian, S. Vincent, and F. Vollmer, "Effective linewidth shifts in single-molecule detection using optical whispering gallery modes," *Applied Physics Letters*, vol. 117, no. 15, p. 151106, 10 2020.
- [80] J. D. Swaim, J. Knittel, and W. P. Bowen, "Detection of nanoparticles with a frequency locked whispering gallery mode microresonator," *Applied Physics Letters*, vol. 102, no. 18, p. 183106, 05 2013.
- [81] H. H. Nguyen, J. Park, S. Kang, and M. Kim, "Surface plasmon resonance: a versatile technique for biosensor applications," *Sensors (Basel)*, vol. 15, no. 5, pp. 10481–10510, may 2015.
- [82] L.-M. Needham, C. Saavedra, and J. K. e. Rasch, "Label-free detection and profiling of individual solution-phase molecules," *Nature*, vol. 629, no. 8014, pp. 1062–1068, May 2024.
- [83] R. W. Taylor and V. Sandoghdar, "Interferometric scattering microscopy: Seeing single nanoparticles and molecules via rayleigh scattering," *Nano Letters*, vol. 19, no. 8, pp. 4827–4835, Aug 2019. [Online]. Available: https://doi.org/10.1021/acs.nanolett.9b01822
- [84] A. Jechow, E. Streed, B. G. Norton, S. Händel, V. Blums, and D. Kielpinski, "Imaging a single atom's absorption and phase shift," in 2013 Conference on Lasers and Electro-Optics Pacific Rim. Optica Publishing Group, 2013, p. TuG1<sub>2</sub>.
- [85] A. Kussrow, C. S. Enders, and D. J. Bornhop, "Interferometric methods for label-free molecular interaction studies," *Analytical Chemistry*, vol. 84, no. 2, pp. 779–792, Jan 2012. [Online]. Available: https://doi.org/10.1021/ac202812h
- [86] M. M. Schmidt, A. G. Brolo, and N. C. Lindquist, "Single-molecule surface-enhanced raman spectroscopy: Challenges, opportunities, and future directions," *ACS Nano*, vol. 18, no. 38, pp. 25930–25938, Sep 2024. [Online]. Available: https://doi.org/10.1021/acsnano.4c09483
- [87] K. Kneipp, Y. Wang, H. Kneipp, L. T. Perelman, I. Itzkan, R. R. Dasari, and M. S. Feld, "Single molecule detection using surface-enhanced raman scattering (sers)," *Phys. Rev. Lett.*, vol. 78, pp. 1667–1670, Mar 1997. [Online]. Available: https://link.aps.org/doi/10.1103/PhysRevLett.78.1667
- [88] W. Mao, Y. Li, X. Jiang, Z. Liu, and L. Yang, "A whispering-gallery scanning microprobe for raman spectroscopy and imaging," *Light: Science & Applications*, vol. 12, no. 1, p. 247, Oct 2023. [Online]. Available: https://doi.org/10.1038/s41377-023-01276-2
- [89] C. Zong, R. Premasiri, H. Lin, Y. Huang, C. Zhang, C. Yang, B. Ren, L. D. Ziegler, and J.-X. Cheng, "Plasmon-enhanced stimulated raman scattering microscopy with single-molecule detection sensitivity," *Nature Communications*, vol. 10, no. 1, p. 5318, Nov 2019. [Online]. Available: https://doi.org/10.1038/s41467-019-13230-1

- [90] M. O. Scully and M. S. Zubairy, *Quantum Optics*. Cambridge University Press, 1997.
- [91] P. Rostron, S. Gaber, and D. Gaber, "Raman spectroscopy, review," *laser*, vol. 21, p. 24, 2016.
- [92] K.-J. Boller, A. Imamoğlu, and S. E. Harris, "Observation of electromagnetically induced transparency," *Phys. Rev. Lett.*, vol. 66, pp. 2593–2596, May 1991. [Online]. Available: https://link.aps.org/doi/10.1103/PhysRevLett.66.2593
- [93] W. Demtröder, Atoms, Molecules and Photons An Introduction to Atomic, Molecular and Quantum Physics. Springer, 2006.
- [94] M. Fleischhauer, A. Imamoglu, and J. P. Marangos, "Electromagnetically induced transparency: Optics in coherent media," *Rev. Mod. Phys.*, vol. 77, pp. 633–673, Jul 2005. [Online]. Available: https://link.aps.org/doi/10.1103/RevModPhys.77.633
- [95] L. Alloatti, R. Palmer, S. Diebold, K. P. Pahl, B. Chen, R. Dinu, M. Fournier, J.-M. Fedeli, T. Zwick, W. Freude, C. Koos, and J. Leuthold, "100ghz silicon-organic hybrid modulator," *Light: Science & Applications*, vol. 3, no. 5, pp. e173–e173, May 2014. [Online]. Available: https://doi.org/10.1038/lsa.2014.54
- [96] L. C. Andrews, Special Functions of Mathematics for Engineers. SPIE Publications, 1998.
- [97] F. E. H. George B. Arfken, Hans J. Weber, *Mathematical methods for physicists*. Elsevier, 2013.

### Appendix A

## Diffraction of a Gaussian beam by a square aperture

The diffraction for a Gaussian beam in the is given by the expression 1.20 where if we input our actual Gaussian beam given by expression 1.12 the final expression for the diffraction integral is

$$E(\vec{r}) = \left(\frac{Ak}{2\pi z z_0}\right) \frac{W_0}{W(-z_W)} \exp\left[ik(z - z_W) + i\frac{k\rho^2}{2z} - i\zeta(-z_W)\right] \times \left(A.1\right) \times \int_{-a}^{a} \int_{-a}^{a} \exp\left[-\frac{{\rho'}^2}{W^2(-z_W)} + i\frac{k{\rho'}^2}{2R(z_W)} - i\frac{k}{z}(xx' + yy')\right] dx'dy',$$

where  $z_W$  refers to the beam waist location on the z axis. The integral can be divided into two similar integrals, so practically we only need to solve one, the integral that we need to solve is

$$I_x = \int_{-a}^{a} \exp\left[-\frac{x'^2}{W^2(-z_W)} + i\frac{kx'^2}{2R(z_W)} - i\frac{kxx'}{z}\right] dx'. \tag{A.2}$$

In order to solve this integral we complete the squared binomial in the argument of the exponential of the integral, but first we group the terms in the following order

$$I_x = \int_{-a}^{a} \exp\left[-\left(Qx'^2 + i\frac{kxx'}{z}\right)\right] dx',\tag{A.3}$$

where  $Q = 1/W^2(-z_W) - ik/(2R(-z_W))$ , completing the squared binomial in the argument of the exponential we obtain

$$I_{x} = \int_{-a}^{a} \exp\left[-\left(\left(\sqrt{Q}x' + i\frac{kx}{2z\sqrt{Q}}\right)^{2} + \frac{k^{2}x^{2}}{4z^{2}Q}\right)\right] dx'. \tag{A.4}$$

We can factor out any term that remains constant for the integration process and we also proceed to do the following change of variables  $u = \sqrt{Q}x' + ikx/2z\sqrt{Q}$ , so with these additional steps our integral is

$$I_x = \frac{1}{\sqrt{Q}} \exp\left[-\frac{k^2 x^2}{4z^2 Q}\right] \int_{-a\sqrt{Q} + i\frac{kx}{2z\sqrt{Q}}}^{a\sqrt{Q} + i\frac{kx}{2z\sqrt{Q}}} \exp\left[-u^2\right] du. \tag{A.5}$$

Lastly we use the definition for the error function [96] as a last step in order to obtain the final expression of the integral

$$I_x = \frac{\sqrt{\pi}}{2\sqrt{Q}} \exp\left[-\frac{k^2 x^2}{4z^2 Q}\right] \left(\operatorname{erf}\left[a\sqrt{Q} + i\frac{kx}{2z\sqrt{Q}}\right] - \operatorname{erf}\left[-a\sqrt{Q} + i\frac{kx}{2z\sqrt{Q}}\right]\right). \quad (A.6)$$

The same steps can be done on the remaining integral and it will produce a similar result

$$I_{y} = \int_{-a}^{a} \exp\left[-\frac{y'^{2}}{W^{2}(-z_{W})} + i\frac{ky'^{2}}{2R(z_{W})} - i\frac{kyy'}{z}\right]dy', \tag{A.7}$$

$$I_{y} = \frac{\sqrt{\pi}}{2\sqrt{Q}} \exp\left[-\frac{k^{2}y^{2}}{4z^{2}Q}\right] \left(\operatorname{erf}\left[a\sqrt{Q} + i\frac{ky}{2z\sqrt{Q}}\right] - \operatorname{erf}\left[-a\sqrt{Q} + i\frac{ky}{2z\sqrt{Q}}\right]\right),$$

so the total diffracted field is

$$E(\vec{r}) = \left(\frac{Ak}{2\pi z z_0}\right) \frac{W_0}{W(-z_W)} \exp\left[ik(z - z_W) + i\frac{k\rho^2}{2z} - i\zeta(-z_W)\right] \times \left(A.8\right)$$
$$\times \frac{\pi}{Q} \exp\left[-\frac{k^2\rho^2}{4z^2Q}\right] f_E(x) f_E(y),$$

with

$$f_E(x) = \frac{1}{2} \mathbf{erf} \left[ a\sqrt{Q} + i\frac{kx}{2z\sqrt{Q}} \right] - \frac{1}{2} \mathbf{erf} \left[ -a\sqrt{Q} + i\frac{kx}{2z\sqrt{Q}} \right]$$

$$f_E(y) = \frac{1}{2} \mathbf{erf} \left[ a\sqrt{Q} + i\frac{ky}{2z\sqrt{Q}} \right] - \frac{1}{2} \mathbf{erf} \left[ -a\sqrt{Q} + i\frac{ky}{2z\sqrt{Q}} \right]$$
(A.9)

which is the same as expression 1.21.

### Appendix B

# Contributions to the wavefront curvature from a square aperture in the far field.

The electric field in the Fraunhofer approximation for a square aperture is represented by Equation 1.21. This equation encompasses three components contributing to the transverse phase, as detailed in Equation 1.26. Initially, we examine the scenario where the beam waist is situated near the aperture, specifically when  $|z_W| \ll z_0$ . Under these conditions,  $R(-z_W) \to \infty$  indicates the presence of a plane wavefront, while  $W(-z_W) \simeq$  $W_0$  and  $Q(-z_W) \simeq 1/W_0^2$  yield no imaginary component, thus having no effect on the transverse phase in Equation 1.26. The third contribution is as follows

$$f_E(x) \simeq \frac{1}{2} \left( \text{Erf} \left[ \frac{a}{W_0} + i \frac{kxW_0}{2z} \right] + \text{Erf} \left[ \frac{a}{W_0} - i \frac{kxW_0}{2z} \right] \right),$$
 (B.1)

and similarly for  $f_E(y)$ , where the argument of one error functions is the conjugate of the other. Using the Mclaurin expansion of the error function [97]

$$\operatorname{Erf}[\eta] = \frac{2}{\sqrt{\pi}} \sum_{n=0}^{\infty} \frac{(-1)^n \eta^{2n+1}}{n!(2n+1)},\tag{B.2}$$

gives

$$\operatorname{Erf}[\eta] + \operatorname{Erf}[\eta^*] = \frac{4|\eta|}{\sqrt{\pi}} \left( Cos(\phi_{\eta}) - \frac{|\eta|^2}{3} Cos(3\phi_{\eta}) + \frac{|\eta|^4}{10} Cos(5\phi_{\eta}) + \dots \right), \quad (B.3)$$

which is a real number and gives no contribution to the phase ( $\Xi_E = 0$ ). In this scenario, it is solely the initial term that affects the transverse phase (as indicated in Eq. 1.26), resulting in  $\Psi_T = (k/2z)\rho^2$ . To put it differently, in the far field approximation, where the waist aligns with the aperture, the radius of curvature at the screen is merely the distance from the aperture to the screen.

When the waist is significantly distant from the aperture, specifically when  $|z_W| \gg z_0$ , the beam exhibits curvature at the aperture location, approximated as  $R(-z_W) \simeq z_W$ . Additionally, the beam width increases to  $W(-z_W) \simeq W_0 z_W/z_0$ , leading to the phase term  $Q(-z_W) \simeq -ik/2z_W$ . In the case of a large aperture, the phase contribution from  $f_E(x)f_E(y)$  is negligible, resulting in  $\Xi_E = 0$ . Consequently, the transverse phase contribution, as described in Eq. 1.26, is represented by Eq. 1.27.

When we decrease the aperture, the phase will be influenced by the error function, which we express as follows.

$$f_E(x) \simeq \frac{1}{2} \left( \text{Erf} \left[ \sqrt{Q(-z_W)} \left( a - \frac{z_W x}{z} \right) \right] + \text{Erf} \left[ \sqrt{Q(-z_W)} \left( a + \frac{z_W x}{z} \right) \right] \right),$$
 (B.4)

and similarly for  $f_E(y)$ . Expanding the error function (Eq. B.2) and rearranging terms we obtain

$$f_E(x) \simeq 2a\sqrt{\frac{Q}{\pi}} \left( 1 - \frac{(Qa^2)}{3} \left[ 1 + 3x^2 \xi^2 \right] + \frac{(Qa^2)^2}{10} \left[ 1 + 10x^2 \xi^2 + 5x^4 \xi^4 \right] - \frac{(Qa^2)^3}{42} \left[ 1 + 21x^2 \xi^2 + 35x^4 \xi^4 + 7x^6 \xi^6 \right] + \dots \right), \tag{B.5}$$

where  $\xi = z_W/az$ . By decreasing the aperture size (a), we ensure that  $x\xi \gg 1$ , leading to the dominance of the final term within each square bracket, which results in the following expression.

$$f_E(x) \simeq 2a\sqrt{\frac{Q(-z_W)}{\pi}} \exp\left(-Q(-z_W)\frac{z_W^2x^2}{z^2}\right) \simeq 2a\sqrt{\frac{-ik}{2\pi z_W}} \exp\left(i\frac{kz_W}{2z^2}x^2\right),$$
 (B.6)

and  $\Xi_E \simeq (kz_W/2z^2)\rho^2$ . Including this in Eq. 1.26 gives the transverse phase contribution of Eq. 1.28.

### Appendix C

# Derivation of the optical Bloch equations for the three-Level $\Lambda$ System

Here I will work out the quantum system regarding our sample, which I model as a three-level  $\Lambda$  system, driven by two external electrical fields; see Fig. 2.4 b). The Hamiltonian of the system is

$$\hat{H} = \hat{H}_0 + \hat{V}(\vec{r}, t), \tag{C.1}$$

were

$$\hat{H}_0 = \hbar \omega_a |a\rangle \langle a| + \hbar \omega_b |b\rangle \langle b| + \hbar \omega_c |c\rangle \langle c|, \tag{C.2}$$

and the interaction term  $\hat{V}(\vec{r},t)$  defined as

$$\hat{V}(\vec{r},t) = -e\vec{r} \cdot \vec{E}_1(\vec{r},t) - e\vec{r} \cdot \vec{E}_2(\vec{r},t), \tag{C.3}$$

which is the dipole interaction with two distinct fields  $E_1$  and  $E_2$ , that are defined as

$$\vec{E}_i(\vec{r},t) = E_i \vec{\xi}_i \cos(k_i z - \omega_i t + \phi_{E_i}), \qquad (C.4)$$

where  $\vec{\xi_i}$  is the polarization vector, for the moment I will not mind any effect related to polarization. Without the interaction Hamiltonian the eigenstates of the system are just  $|a\rangle, |b\rangle, |c\rangle$ . I am interested in finding a state  $|\Psi(t)\rangle$  that fulfills the Schrödinger equation

$$i\hbar \frac{d}{dt} |\Psi(t)\rangle = \hat{H} |\Psi(t)\rangle.$$
 (C.5)

By a standard procedure, let us propose that the state  $|\Psi(t)\rangle$  can be written as

$$|\Psi(t)\rangle = \sum_{m} c_m(t)e^{-i\omega_m t}|m\rangle,$$
 (C.6)

where the states  $|m\rangle$  are the eigenstates of  $\hat{H}_0$  which are  $|a\rangle$ ,  $|b\rangle$  or  $|c\rangle$ . Now the task is to find equations for the coefficients  $c_m(t)$ , to do so, I substitute the previous equation into the complete Schrödinger equation to obtain

$$\sum_{m} i\hbar \dot{c}_{m}(t)e^{-i\omega_{m}t}|m\rangle + \sum_{m} \hbar \omega_{m}c_{m}(t)e^{-i\omega_{m}t}|m\rangle =$$

$$\sum_{m} \hbar \omega_{m}c_{m}(t)e^{-i\omega_{m}t}|m\rangle + \sum_{m} c_{m}(t)e^{-i\omega_{m}t}\hat{V}(\vec{r},t)|m\rangle,$$
(C.7)

which simplifies to

$$\sum_{m} i\hbar \dot{c}_{m}(t)e^{-i\omega_{m}t}|m\rangle = \sum_{m} c_{m}(t)e^{-i\omega_{m}t}\hat{V}(\vec{r},t)|m\rangle, \qquad (C.8)$$

taking the inner product with the basis state  $|n\rangle$  I obtain an expression for  $\dot{c}_n(t)$ 

$$\dot{c}_n(t) = -\frac{i}{\hbar} \sum_m c_m(t) e^{-i(\omega_m - \omega_n)t} \langle n | \hat{V}(\vec{r}, t) | m \rangle.$$
 (C.9)

Let us analyze the  $\langle n|\hat{V}(\vec{r},t)|m\rangle$  terms; by rewriting them I obtain the following

$$\langle n|\hat{V}(\vec{r},t)|m\rangle = -e\sum_{i=1}^{2} \langle n|\vec{r}\cdot\vec{E}_{i}(\vec{r},t)|m\rangle. \tag{C.10}$$

Now, let me explicitly write the terms on the right side of the equation to obtain

$$-e\langle n|\vec{r}\cdot\vec{E}_i(\vec{r},t)|m\rangle = -eE_i\vec{\xi}_i\cdot\langle n|\vec{r}\cos(k_iz - \omega_it + \phi_{E_i})|m\rangle.$$
 (C.11)

I will consider the standard dipolar approximation where  $k_i z \ll 1$  due to the wavelength of the E.M. field being much larger than the size of the quantum system, so I approximate the terms as

$$-e\langle n|\vec{r}\cdot\vec{E}_i(\vec{r},t)|m\rangle \approx -eE_i\cos\left(-\omega_i t + \phi_{E_i}\right)\vec{\xi}_i\cdot\langle n|\vec{r}|m\rangle. \tag{C.12}$$

Now writing explicitly the term  $\langle n|\vec{r}|m\rangle$ 

$$\langle n|\vec{r}|m\rangle = \int \psi_n^*(\vec{r})\vec{r}\psi_m(\vec{r})d^3r, \qquad (C.13)$$

if n=m then I have the product of an even square-integrable function with an odd function, which is integrated in a symmetric interval, this set of conditions allows us to obtain the result that such integral is zero; therefore, the only terms that contribute are those that  $n \neq m$  then the terms for the interaction Hamiltonian are approximately

$$-e\langle n|\vec{r}\cdot\vec{E}_{i}(\vec{r},t)|m\rangle \approx -E_{i}\cos\left(-\omega_{i}t + \phi_{E_{i}}\right)\langle n|e\vec{\xi}_{i}\cdot\vec{r}|m\rangle\left(1 - \delta_{nm}\right)$$

$$= -\mu_{nm} E_{i}\cos\left(-\omega_{i}t + \phi_{E_{i}}\right)\left(1 - \delta_{nm}\right).$$
(C.14)

where I introduced the dipole matrix element  $\mu_{nm,i} = \langle n|e\vec{\xi}_i \cdot \vec{r}|m\rangle$ . Having worked out these expressions, I can write the differential equations for the coefficients  $c_m(t)$ 

$$\dot{c}_a(t) = -\frac{i}{\hbar} c_b(t) e^{-i(\omega_b - \omega_a)t} \left( \sum_{i=1}^2 -\mu_{ab,i} E_i \cos\left(-\omega_i t + \phi_{E_i}\right) \right)$$

$$-\frac{i}{\hbar} c_c(t) e^{-i(\omega_c - \omega_a)t} \left( \sum_{i=1}^2 -\mu_{ac,i} E_i \cos\left(-\omega_i t + \phi_{E_i}\right) \right).$$
(C.15)

I can rewrite the previous expression as

$$\dot{c}_{a}(t) = -\frac{i}{2}c_{b}(t) \left(\Omega_{ab,1}^{*} e^{i(\omega_{ab}+\omega_{1})t} + \Omega_{ab,1} e^{i(\omega_{ab}-\omega_{1})t} + \Omega_{ab,2} e^{i(\omega_{ab}+\omega_{2})t} + \Omega_{ab,2} e^{i(\omega_{ab}-\omega_{2})t}\right) 
-\frac{i}{2}c_{c}(t) \left(\Omega_{ac,1}^{*} e^{i(\omega_{ac}+\omega_{1})t} + \Omega_{ac,1} e^{i(\omega_{ac}-\omega_{1})t} + \Omega_{ac,2} e^{i(\omega_{ac}+\omega_{2})t} + \Omega_{ac,2} e^{i(\omega_{ac}-\omega_{2})t}\right),$$
(C.16)

where I have used the following definitions  $\omega_{nm} = \omega_n - \omega_m$  and the Rabi frequency  $\Omega_{nm,i}^* = -\frac{\mu_{nm,i}E_i}{\hbar}e^{-i\phi_{E_i}}$ . Using the rotating-wave approximation, meaning that the fast oscillating terms average to zero, which are the exponentials whose argument is of the form  $\omega_{nm} + \omega_i$ , I obtain the following

$$\dot{c}_{a}(t) = -\frac{i}{2}c_{b}(t)\left(\Omega_{ab,1}e^{-i\delta_{ab,1}t} + \Omega_{ab,2}e^{-i\delta_{ab,2}t}\right)$$

$$-\frac{i}{2}c_{c}(t)\left(\Omega_{ac,1}e^{-i\delta_{ac,1}t} + \Omega_{ac,2}e^{-i\delta_{ac,2}t}\right)$$
(C.17)

where  $\delta_{nm,i} = \omega_i - \omega_{nm}$  is the detuning of the field  $E_i$  with respect to the transition between levels n, m. This is the differential equation for  $\dot{c}_a(t)$  and we can observe that both fields couple the levels a and b as well as the levels a and c. Using a similar procedure, I can write the differential equation for  $\dot{c}_b(t)$ 

$$\dot{c}_{b}(t) = -\frac{i}{2}c_{a}(t) \left(\Omega_{ab,1}^{*}e^{i(\omega_{1}-\omega_{ab})t} + \Omega_{ab,1}e^{-i(\omega_{1}+\omega_{ab})t} + \Omega_{ab,2}e^{-i(\omega_{2}+\omega_{ab})t}\right)$$

$$+\Omega_{ab,2}^{*}e^{i(\omega_{2}-\omega_{ab})t} + \Omega_{ab,2}e^{-i(\omega_{2}+\omega_{ab})t}\right)$$

$$-\frac{i}{2}c_{c}(t) \left(\Omega_{bc,1}^{*}e^{i(\omega_{1}-\omega_{cb})t} + \Omega_{bc,1}e^{-i(\omega_{1}+\omega_{cb})t} + \Omega_{bc,2}e^{-i(\omega_{2}+\omega_{cb})t}\right),$$

$$(C.18)$$

$$C.18$$

and by using the rotating-wave approximation I obtain

$$\dot{c}_{b}(t) = -\frac{i}{2}c_{a}(t)\left(\Omega_{ab,1}^{*}e^{i(\omega_{1}-\omega_{ab})t} + \Omega_{ab,2}^{*}e^{i(\omega_{2}-\omega_{ab})t}\right)$$

$$-\frac{i}{2}c_{c}(t)\left(\Omega_{bc,1}^{*}e^{i(\omega_{1}-\omega_{cb})t} + \Omega_{bc,2}^{*}e^{i(\omega_{2}-\omega_{cb})t}\right).$$
(C.19)

Now, let us analyze the terms that are factored with the coefficient  $c_c(t)$ , since I am modeling a  $\Lambda$  system, the frequency difference  $\omega_{cb} = \omega_c - \omega_b$  (with  $\omega_c > \omega_b$ ) is much smaller than  $\omega_{ab}$  or  $\omega_{ac}$  ( $\omega_{cb} \ll \omega_{ab}, \omega_{ac}$ ), also, the frequency  $\omega_1$  and  $\omega_2$  of the fields  $E_1$  and  $E_2$  are of the order of magnitude of  $\omega_{ab}$  and  $\omega_{ac}$ , which makes the frequency difference  $\omega_i - \omega_{cb}$  much greater than  $\omega_i - \omega_{ab}$  or  $\omega_i - \omega_{ac}$  (i = 1, 2) this means that the terms with  $\omega_i - \omega_{cb}$  will oscillate much quicker which allows us vanish them by using the rotating wave approximation. In addition, by analyzing the Rabi frequencies  $\Omega_{cb,i} = \mu_{cb,i} E_i e^{-i\phi_{E_i}}/\hbar$  and explicitly writing the dipole matrix element  $\mu_{cb,i} = \langle c|e\vec{\xi}_i \cdot \vec{r}|b\rangle$  since c and b are modeled as hyperfine levels in atomic systems or rotational/vibrational in molecular systems, the dipole matrix element will probably be very small when compared against the dipole element  $\mu_{am,i}$ . With all of these considerations I can then vanish the terms factored with  $c_c(t)$ , doing so I obtain

$$\dot{c}_b(t) = -\frac{i}{2}c_a(t)\left(\Omega_{ab,1}^* e^{i\delta_{ab,1}t} + \Omega_{ab,2}^* e^{i\delta_{ab,2}t}\right),\tag{C.20}$$

this basically means that the electric fields can not strongly drive a transition between levels b and c, with similar arguments I can obtain then the differential equation for  $\dot{c}_c(t)$ 

$$\dot{c}_c(t) = -\frac{i}{2}c_a(t)\left(\Omega_{ac,1}^* e^{i\delta_{ac,1}t} + \Omega_{ac,2}^* e^{i\delta_{ac,2}t}\right). \tag{C.21}$$

I have the differential equations for all of the coefficients; however, both fields can drive the same transition, I would like that only the  $E_1$  field drives the  $a \leftrightarrow b$  transition and

the  $E_2$  field drives the  $a \leftrightarrow c$  transition, in order to do so I can use the rotating-wave approximation, therefore I impose that  $|\delta_{ab,1}| << |\delta_{ab,2}|$  so that even though the  $E_2$  field can drive the  $a \leftrightarrow b$  transition it is heavily suppressed by a fast oscillating term. Likewise, I impose  $|\delta_{ac,2}| \ll |\delta_{ac,1}|$ . If both of these conditions are satisfied, then I have the following set of coupled differential equations

$$\dot{c}_{a}(t) = -\frac{i}{2}c_{b}(t)\Omega_{ab}e^{-i\delta_{ab}t} - \frac{i}{2}c_{c}(t)\Omega_{ac}e^{-i\delta_{ac}t},$$

$$\dot{c}_{b}(t) = -\frac{i}{2}c_{a}(t)\Omega_{ab}^{*}e^{i\delta_{ab}t},$$

$$\dot{c}_{c}(t) = -\frac{i}{2}c_{a}(t)\Omega_{ac}^{*}e^{i\delta_{ac}t},$$
(C.22)

with

Proceeding forward, I am not interested in solving exactly this set of equations, rather, our focus will be then on obtaining the optical Bloch equations for this system, in order to do so I have to calculate the density matrix for this system, by definition

$$\hat{\rho}(t) = |\Psi(t)\rangle\langle\Psi(t)|,\tag{C.24}$$

and writing it in matrix form I obtain

$$\rho_{\text{matrix}} = \begin{pmatrix} c_a c_a^* & c_a c_b^* & c_a c_c^* \\ c_b c_a^* & c_b c_b^* & c_b c_c^* \\ c_c c_a^* & c_c c_b^* & c_c c_c^* \end{pmatrix}, \tag{C.25}$$

whereby construction of the  $\rho$  matrix, the elements  $\rho_{nm}$  satisfy  $\rho_{nm} = \rho_{mn}^*$ . To obtain the optical Bloch equations, I must find the time evolution of these elements

$$\frac{d}{dt}\rho_{nm} = \frac{dc_n}{dt}c_m^* + c_n\frac{dc_m^*}{dt},\tag{C.26}$$

beginning with elements  $\rho_{aa}$ ,  $\rho_{bb}$ , and  $\rho_{cc}$ 

$$\frac{d}{dt}\rho_{aa} = \left(-\frac{i}{2}c_{b}(t)\Omega_{ab}e^{-i\delta_{ab}t} - \frac{i}{2}c_{c}(t)\Omega_{ac}e^{-i\delta_{ac}t} - \frac{1}{2}(\gamma_{ab} + \gamma_{ac})c_{a}\right)c_{a}^{*} + c_{a}\left(\frac{i}{2}c_{b}^{*}(t)\Omega_{ab}^{*}e^{i\delta_{ab}t} + \frac{i}{2}c_{c}^{*}(t)\Omega_{ac}^{*}e^{i\delta_{ac}t} - \frac{1}{2}(\gamma_{ab} + \gamma_{ac})c_{a}^{*}\right),$$
(C.27)

where I have added extra terms as  $\frac{1}{2}(\gamma_{ab} + \gamma_{ac}) c_a$  that represent spontaneous emission from the *a* level considering two different decay rates  $\gamma_{ab}$  and  $\gamma_{ac}$ , the spontaneous emission follows the equation

$$\frac{dc_a}{dt} = -\frac{1}{2}(\gamma_{ab} + \gamma_{ac})c_a, \tag{C.28}$$

with  $\gamma_{nm} = \omega_{nm}^3 \mu_{nm}^2 / 3\pi \epsilon_0 \hbar c^3$ . A more in-depth explanation for spontaneous emission can be found in the literature [49]. Rearranging the equation for  $d\rho_{aa}/dt$  I obtain

$$\frac{d\rho_{aa}}{dt} = -(\gamma_{ab} + \gamma_{ac})\rho_{aa} + \frac{i}{2}\left(\tilde{\rho}_{ab}\Omega_{ab}^* - \tilde{\rho}_{ba}\Omega_{ab}\right) + \frac{i}{2}\left(\tilde{\rho}_{ac}\Omega_{ac}^* - \tilde{\rho}_{ca}\Omega_{ac}\right), \tag{C.29}$$

with  $\tilde{\rho}_{ab} = \rho_{ab}e^{i\delta_{ab}t}$  and  $\Omega_{ba} = \Omega_{ab}^*$ . Now for the other elements

$$\frac{d\rho_{bb}}{dt} = \gamma_{ab}\rho_{aa} + \frac{i}{2}\left(\tilde{\rho}_{ba}\Omega_{ab} - \tilde{\rho}_{ab}\Omega_{ab}^*\right),\tag{C.30}$$

$$\frac{d\rho_{cc}}{dt} = \gamma_{ac}\rho_{aa} + \frac{i}{2} \left( \tilde{\rho}_{ca}\Omega_{ac} - \tilde{\rho}_{ac}\Omega_{ac}^* \right), \tag{C.31}$$

where again, due to spontaneous emission, I introduced the terms  $\gamma_{ab}\rho_{aa}$  and  $\gamma_{ac}\rho_{aa}$  to conserve the population of the energy levels. Now for the coherece terms  $\rho_{nm}$  with  $n \neq m$ 

$$\frac{d\rho_{ab}}{dt} = \frac{dc_a(t)}{dt}c_b^*(t) + c_a(t)\frac{dc_b^*(t)}{dt}, \qquad (C.32)$$

$$\frac{d\rho_{ab}(t)}{dt} = \left(-\frac{i}{2}c_b(t)\Omega_{ab}e^{-i\delta_{ab}t} - \frac{i}{2}c_c(t)\Omega_{ac}e^{-i\delta_{ac}t} - \frac{1}{2}\left(\gamma_{ab} + \gamma_{ac}\right)c_a(t)\right)c_b^*(t)$$

$$+c_a(t)\left(\frac{i}{2}c_a^*(t)\Omega_{ab}e^{-i\delta_{ab}t}\right).$$

Simplifying this equation I obtain

$$\frac{d\rho_{ab}}{dt} = -\frac{1}{2} \left( \gamma_{ab} + \gamma_{ac} \right) \rho_{ab} + \frac{i}{2} e^{-i\delta_{ab}t} \left( \left( \rho_{aa} - \rho_{bb} \right) \Omega_{ab} - \tilde{\rho}_{cb} \Omega_{ac} \right), \tag{C.33}$$

where  $\tilde{\rho}_{cb} = \rho_{cb}e^{i\delta_{cb}t}$  and I have defined  $\delta_{cb} = \delta_{ab} - \delta_{ac}$ . However, I would like to write this equation as a function of  $\tilde{\rho}_{ab} = \rho_{ab}e^{i\delta_{ab}t}$  to simplify the time dependence, to do so let us do the following

$$\frac{d\tilde{\rho}_{ab}}{dt} = \frac{d}{dt} \left( \rho_{ab} e^{i\delta_{ab}t} \right) = \frac{d\rho_{ab}}{dt} e^{i\delta_{ab}t} + i\delta_{ab}\rho_{ab} e^{i\delta_{ab}t}, \tag{C.34}$$

and now I can substitute the expression for  $d\rho_{ab}/dt$  to obtain

$$\frac{d\tilde{\rho}_{ab}}{dt} = \left(i\delta_{ab} - \frac{1}{2}\left(\gamma_{ab} + \gamma_{ac}\right)\right)\tilde{\rho}_{ab} + \frac{i}{2}\left(\left(\rho_{aa} - \rho_{bb}\right)\Omega_{ab} - \tilde{\rho_{cb}}\Omega_{ac}\right). \tag{C.35}$$

Likewise with a similar treatment, I obtain for  $d\tilde{\rho}_{ac}/dt$ 

$$\frac{d\tilde{\rho}_{ac}}{dt} = \left(i\delta_{ac} - \frac{1}{2}\left(\gamma_{ab} + \gamma_{ac}\right)\right)\tilde{\rho}_{ac} + \frac{i}{2}\left(\left(\rho_{aa} - \rho_{cc}\right)\Omega_{ac} - \tilde{\rho}_{bc}\Omega_{ab}\right),\tag{C.36}$$

and for  $d\tilde{\rho}_{cb}/dt$  I obtain

$$\frac{d\tilde{\rho}_{cb}}{dt} = i\delta_{cb}\tilde{\rho}_{cb} + \frac{i}{2}\left(\tilde{\rho}_{ca}\Omega_{ab} - \tilde{\rho}_{ab}\Omega_{ac}^*\right). \tag{C.37}$$

I have then obtained all of the optical Bloch equations for the system, I have for the populations

$$\frac{d\rho_{aa}}{dt} = -(\gamma_{ab} + \gamma_{ac})\rho_{aa} + \frac{i}{2} \left( \tilde{\rho}_{ab} \Omega_{ab}^* - \tilde{\rho}_{ba} \Omega_{ab} \right) + \frac{i}{2} \left( \tilde{\rho}_{ac} \Omega_{ac}^* - \tilde{\rho}_{ca} \Omega_{ac} \right), \qquad (C.38)$$

$$\frac{d\rho_{bb}}{dt} = \gamma_{ab}\rho_{aa} + \frac{i}{2} \left( \tilde{\rho}_{ba} \Omega_{ab} - \tilde{\rho}_{ab} \Omega_{ab}^* \right),$$

$$\frac{d\rho_{cc}}{dt} = \gamma_{ac}\rho_{aa} + \frac{i}{2} \left( \tilde{\rho}_{ca} \Omega_{ac} - \tilde{\rho}_{ac} \Omega_{ac}^* \right),$$

and for the coherences

$$\frac{d\tilde{\rho}_{ab}}{dt} = \left(i\delta_{ab} - \frac{1}{2}\left(\gamma_{ab} + \gamma_{ac}\right)\right)\tilde{\rho}_{ab} + \frac{i}{2}\left(\left(\rho_{aa} - \rho_{bb}\right)\Omega_{ab} - \tilde{\rho}_{cb}\Omega_{ac}\right), \tag{C.39}$$

$$\frac{d\tilde{\rho}_{ac}}{dt} = \left(i\delta_{ac} - \frac{1}{2}\left(\gamma_{ab} + \gamma_{ac}\right)\right)\tilde{\rho}_{ac} + \frac{i}{2}\left(\left(\rho_{aa} - \rho_{cc}\right)\Omega_{ac} - \tilde{\rho}_{bc}\Omega_{ab}\right),$$

$$\frac{d\tilde{\rho}_{cb}}{dt} = i\delta_{cb}\tilde{\rho}_{cb} + \frac{i}{2}\left(\tilde{\rho}_{ca}\Omega_{ab} - \tilde{\rho}_{ab}\Omega_{ac}^{*}\right),$$

where the complex conjugates of the time evolution of the coherences have to be considered to obtain all nine equations for each one of the elements of the density matrix.

### Appendix D

# Approximations for the steady-state of the optical Bloch equations of the three-Level $\lambda$ system.

We modeled the response of a three-level system driven with two lasers with frequencies  $\omega_1$  and  $\omega_2$  as depicted in Fig. 2.4b). Each transition has a Rabi frequency  $\Omega_{ab}$  and  $\Omega_{ac}$ , a resonant frequency  $\omega_{ab}$  and  $\omega_{ac}$ , a de-tuning  $\delta_{ab} = \omega_1 - \omega_{ab}$  and  $\delta_{ac} = \omega_2 - \omega_{ac}$ , a decay rate  $\gamma_{ab}$  and  $\gamma_{ac}$  respectively, and a two-photon resonant frequency  $\omega_{cb}$  and detuning  $\delta_{cb} = \delta_{ab} - \delta_{ac}$ . The optical Bloch equations of this system are given by Eqs. C.38, C.39. I obtained the steady-state solutions ( $\dot{\rho}_{nm} = 0$ ) by entering them into Wolfram Mathematica software along with the conservation of population  $\rho_{aa} + \rho_{bb} + \rho_{cc} = 1$ , and then using the Solve command; next, I simplified the result of the command and obtained the following expressions for the coherences.

$$\rho_{ab} = -2\delta_{cb}\Omega_{ab}|\Omega_{ac}|^{2} \left(-2i\gamma_{ab}^{2}\delta_{cb} - 2i\gamma_{ab}\gamma_{ac}\delta_{cb} + 4\gamma_{ab}\delta_{ab}\delta_{cb} - \gamma_{ab}|\Omega_{ac}|^{2} - \gamma_{ac}|\Omega_{ab}|^{2}\right)/D, 
+4\gamma_{ab}\delta_{ab}\delta_{cb} - \gamma_{ab}|\Omega_{ac}|^{2} - 2i\gamma_{ac}\delta_{cb} - 2i\gamma_{ac}\gamma_{ab}\delta_{cb} + 4\gamma_{ac}\delta_{ac}\delta_{cb} + \gamma_{ab}|\Omega_{ac}|^{2} + \gamma_{ac}|\Omega_{ab}|^{2}\right)/D, 
D = 4\gamma_{ab}|\Omega_{ac}|^{2}\delta_{cb}^{2} \left(4\delta_{ab}^{2} + (\gamma_{ab} + \gamma_{ac})^{2}\right) + 4\gamma_{ac}|\Omega_{ab}|^{2}\delta_{cb}^{2} \left(4\delta_{ac}^{2} + (\gamma_{ab} + \gamma_{ac})^{2}\right) + 8\delta_{cb} \left(\gamma_{ac}\delta_{ac}|\Omega_{ab}|^{4} - \gamma_{ab}\delta_{ab}|\Omega_{ac}|^{4} + (\gamma_{ab} + \gamma_{ac})|\Omega_{ab}|^{2}|\Omega_{ac}|^{2}\delta_{cb}\right) 
+ |\Omega_{ab}|^{2}|\Omega_{ac}|^{2} \left(|\Omega_{ab}|^{2}(\gamma_{ab} + 2\gamma_{ac}) + |\Omega_{ac}|^{2}(2\gamma_{ab} + \gamma_{ac})\right) + \gamma_{ac}|\Omega_{ab}|^{6} + \gamma_{ab}|\Omega_{ac}|^{6}. \tag{D.1}$$

The first approximation that I will consider for these solutions is around the two-photon resonance, for that I will take the following relations, first the Rabi frequencies are greater than the one- and two-photon detunings ( $|\Omega_{nm}| > \delta_{ab}, \delta_{ab}, \delta_{cb}$ ) as well as greater than the decay rates ( $|\Omega_{nm}| > \gamma_{nm}$ ), at the same time the one- and two-photon detunings are greater than the decay rates ( $\delta_{ab}, \delta_{ac}, \delta_{cb} > \gamma_{nm}$ ) lastly the one-photon detunings are of similar magnitude to the two-photon detunings ( $|\delta_{ab}|, |\delta_{ac}| \approx |\delta_{cb}|$ ), with this relations the terms of the form  $\gamma |\Omega|^2$  of the term in parentheses on the numerator on Eq. D.1 are the dominant ones and the terms of the form  $\gamma |\Omega|^6$  on the denominator (D factor in Eq. D.1) are the dominant ones, we discard then the other terms, and with this we obtain the following approximation for the real part of the coherences around the two-photon resonance.

$$\operatorname{Re}\left[\rho_{ab}\right] \simeq 2\delta_{cb}\Omega_{ab}|\Omega_{ac}|^{2} \left(\gamma_{ac}|\Omega_{ab}|^{2} + \gamma_{ab}|\Omega_{ac}|^{2}\right)/D_{r},$$

$$\operatorname{Re}\left[\rho_{ac}\right] \simeq -2\delta_{cb}\Omega_{ac}|\Omega_{ab}|^{2} \left(\gamma_{ac}|\Omega_{ab}|^{2} + \gamma_{ab}|\Omega_{ac}|^{2}\right)/D_{r},$$

$$D_{r} = |\Omega_{ab}|^{2}|\Omega_{ac}|^{2} (|\Omega_{ab}|^{2} \left(\gamma_{ab} + 2\gamma_{ac}\right) + |\Omega_{ac}|^{2} (2\gamma_{ab} + \gamma_{ac})) + \gamma_{ac}|\Omega_{ab}|^{6} + \gamma_{ab}|\Omega_{ac}|^{6},$$

$$(D.2)$$

taking the difference of these expressions as shown in Eq.2.67 we obtain

$$\operatorname{Re}\left[\gamma_{ab}\frac{\rho_{ab}}{\Omega_{ab}} - \gamma_{ac}\frac{\rho_{ac}}{\Omega_{ac}}\right] = \frac{2\delta_{cb}\left(\gamma_{ac}|\Omega_{ab}|^2 + \gamma_{ab}|\Omega_{ac}|^2\right)}{\left(|\Omega_{ab}|^2 + |\Omega_{ac}|^2\right)^2},\tag{D.3}$$

which taking  $\gamma_{ab} = \gamma_{ac} = \gamma$  leads to Eq. 2.74. The next approximation that we are interested in is far away from the two-photon resonance, for that I will consider that the one- and two-photon detuning are of the same magnitude  $|\delta_{ab}|, |\delta_{ac}| \approx |\delta_{cb}|$  as well as consider that the detuning is greater than the Rabi frequencies which themselves are greater than the decay rates  $|\delta_{nm}| > |\Omega_{kl}| > \gamma_{pq}$ , with these relations the terms of the form  $\gamma |\Omega|^2 \delta_{nm}^2 \delta_{cb}^2$  on the denominator in Eq. D.1 (*D* term) are the dominant ones so I will discard the other terms, as for the numerator in Eq. D.1 the terms of the form  $\gamma \delta_{nm} \delta_{cb}$  inside the parentheses are the dominant ones, so I will discard the other terms, with these considerations in mind, I obtain the following approximation far away from the two-photon resonance

$$\operatorname{Re}\left[\rho_{ab}\right] \simeq -\frac{\gamma_{ab}\Omega_{ab}|\Omega_{ac}|^{2}\delta_{ab}}{2\left(\gamma_{ab}|\Omega_{ac}|^{2}\delta_{ab}^{2} + \gamma_{ac}|\Omega_{ab}|^{2}\delta_{ac}^{2}\right)},$$

$$\operatorname{Re}\left[\rho_{ac}\right] \simeq -\frac{\gamma_{ac}\Omega_{ac}|\Omega_{ab}|^{2}\delta_{ac}}{2\left(\gamma_{ab}|\Omega_{ac}|^{2}\delta_{ab}^{2} + \gamma_{ac}|\Omega_{ab}|^{2}\delta_{ac}^{2}\right)}.$$
(D.4)

As shown in Fig.2.7, we observe that by keeping fixed one of the detunings  $(\delta_{ac})$  and varying the other one  $(\delta_{ab})$  the width of the envelope of the coherences is proportional to the fixed detuning instead of the Rabi frequecy  $\Omega$ . By taking  $\gamma_{ab} = \gamma_{ac} = \gamma$  and  $|\Omega_{ab}|^2 = |\Omega_{ac}|^2 = |\Omega|^2$  in Eq. D.4 we obtain

$$\operatorname{Re}\left[\frac{\rho_{ab}}{\Omega_{ab}}\right] \simeq -\frac{\delta_{ab}}{2\left(\delta_{ab}^2 + \delta_{ac}^2\right)},$$

$$\operatorname{Re}\left[\frac{\rho_{ac}}{\Omega_{ac}}\right] \simeq -\frac{\delta_{ac}}{2\left(\delta_{ab}^2 + \delta_{ac}^2\right)},$$
(D.5)

where we can see from the expression for  $\rho_{ac}/\Omega_{ac}$  that the FWHM happens when  $\delta_{ab} = \delta_{ac}$  as it can be seen in Fig. 2.5.

These two limit cases give some insight into the dependence of the signal with external experimental parameters, however none of them can be used in order to extract information about a change of the two bottom levels, particularly the detuning  $\delta_{cb}$ , one might be tempted to use the near-two-photon resonance approximation (Eq. D.3) but there are technical limits to it, so using it is not a viable option. One way we solve this problem is by making two measurements at different powers (high H and low L powers) and taking the difference of the normalized signals with respect to the power, so in this way the signal amplitude is independent of the power. I require a different approximation of the full solution for this measurement procedure; this approximation is still off-resonance with the two-photon transition but close enough so that some of the information about it is

still present in the expressión. For this approximation I will consider that the one- and two-photon detunings are of similar magnitude  $|\delta_{ab}|, |\delta_{ac}| \approx |\delta_{cb}|$ , the Rabi frequencies are also of similar magnitude to the detunings  $|\Omega_{nm}| \approx \delta_{kl}$ , and the detunings and Rabi frequencies are greater than the decay rates  $|\delta_{kl}|, |\Omega_{nm}| > \gamma_{pq}$ , with these relations the only terms that I discard of Eq. D.1 are those of the form  $\gamma^3 |\Omega|^2 \delta_{cb}^2$  in the denominator (D factor) and in the numerator the terms of the form  $\gamma^2 \delta_{cb}$  inside the parentheses, which will vanish anyway since we are taking the real part. The expressions for the coherences under these approximations are

$$\operatorname{Re}\left[\rho_{ab}\right] \simeq -2\delta_{cb}\Omega_{ab}|\Omega_{ac}|^{2} \left(4\gamma_{ab}\delta_{ab}\delta_{cb} - \gamma_{ac}|\Omega_{ab}|^{2} - \gamma_{ab}|\Omega_{ac}|^{2}\right)/D_{d}, \tag{D.6}$$

$$\operatorname{Re}\left[\rho_{ac}\right] \simeq -2\delta_{cb}\Omega_{ac}|\Omega_{ab}|^{2} \left(4\gamma_{ac}\delta_{ac}\delta_{cb} + \gamma_{ac}|\Omega_{ab}|^{2} + \gamma_{ab}|\Omega_{ac}|^{2}\right)/D_{d}, \tag{D.6}$$

$$D_{d} = 16\gamma_{ac}|\Omega_{ab}|^{2}\delta_{ac}^{2}\delta_{cb}^{2} + 16\gamma_{ab}|\Omega_{ac}|^{2}\delta_{ab}^{2}\delta_{cb}^{2}$$

$$+8\delta_{cb}\left(\gamma_{ac}\delta_{ac}|\Omega_{ab}|^{4} - \gamma_{ab}\delta_{ab}|\Omega_{ac}|^{4} + (\gamma_{ab} + \gamma_{ac})\delta_{cb}|\Omega_{ab}|^{2}|\Omega_{ac}|^{2}\right)$$

$$+|\Omega_{ab}|^{2}|\Omega_{ac}|^{2}\left(|\Omega_{ab}|^{2}(\gamma_{ab} + 2\gamma_{ac}) + |\Omega_{ac}|^{2}(2\gamma_{ab} + \gamma_{ac})\right) + \gamma_{ac}|\Omega_{ab}|^{6} + \gamma_{ab}|\Omega_{ac}|^{6}.$$

Now for these expressions, I will take the difference between the normalized coherences with respect to the Rabi frequency (Re  $(\rho_{ab}/\Omega_{ab} - \rho_{ac}/\Omega_{ac})$ ) and introduce a new factor of the form  $|\Omega|^2/\delta_{cb}^2 = x$ . Writing the difference of the normalized coherences of Eq. D.6 using this new factor and only keeping the linear terms of it, I obtain

$$\operatorname{Re}\left[\frac{\rho_{ab}}{\Omega_{ab}} - \frac{\rho_{ac}}{\Omega_{ac}}\right] \approx \frac{4(b\delta_{ac} - c\delta_{ab}) + x\delta_{cb}(1+c)(b+c)}{4(2(b\delta_{ac}^2 + c\delta_{ab}^2) + x\delta_{cb}(b\delta_{ac} - c^2\delta_{ab} + (1+b)c\delta_{cb}))},\tag{D.7}$$

where  $c = |\Omega_{ac}|^2/|\Omega_{ab}|^2$  and  $b = \gamma_{ac}/\gamma_{ab}$ , I can rewrite and approximate this previous expression as

$$\operatorname{Re}\left[\frac{\rho_{ab}}{\Omega_{ab}} - \frac{\rho_{ac}}{\Omega_{ac}}\right] \approx \frac{1}{4} \frac{a + bx}{c + dx} \approx \frac{1}{4} \left(\frac{a}{c} + \frac{x(bc - ad)}{c^2}\right),\tag{D.8}$$

with

$$a = 4(b\delta_{ac} - c\delta_{ab}),$$

$$b = \delta_{cb}(1+c)(b+c),$$

$$c = 2(b\delta_{ac}^2 + c\delta_{ab}^2),$$

$$d = \delta_{cb}(b\delta_{ac} - c^2\delta_{ab} + (1+b)c\delta_{cb}).$$

Considering that  $x \ll 1$  I can discard the linear term in x on Eq. D.8, and by rewriting the remaining term I obtain

$$\operatorname{Re}\left[\frac{\rho_{ab}}{\Omega_{ab}} - \frac{\rho_{ac}}{\Omega_{ac}}\right] \approx \frac{a}{4c} = \frac{\gamma_{ac}|\Omega_{ab}|^2 \delta_{ac} - \gamma_{ab}|\Omega_{ac}|^2 \delta_{ab}}{2\left(\gamma_{ac}|\Omega_{ab}|^2 \delta_{ac}^2 + \gamma_{ab}|\Omega_{ac}|^2 \delta_{ab}^2\right)},\tag{D.9}$$

which is the same as taking the difference of the normalized coherences from Eq. D.4. This previous expression is the signal for low power L, for high power H we need to take the next linear term in x which is approximately

$$\operatorname{Re}\left[\frac{\rho_{ab}}{\Omega_{ab}} - \frac{\rho_{ac}}{\Omega_{ac}}\right] \approx \frac{a}{4c} + \frac{x(bx - ad)}{c^2} \approx \frac{\gamma_{ac}|\Omega_{ab}|^2 \delta_{ac} - \gamma_{ab}|\Omega_{ac}|^2 \delta_{ab}}{2\left(\gamma_{ac}|\Omega_{ab}|^2 \delta_{ac}^2 + \gamma_{ab}|\Omega_{ac}|^2 \delta_{ab}^2\right)} + \frac{(|\Omega_{ab}|^2 + |\Omega_{ac}|^2)\left(\gamma_{ac}|\Omega_{ab}|^2 + \gamma_{ab}|\Omega_{ac}|^2\right)}{8\delta_{cb}\left(\gamma_{ac}|\Omega_{ab}|^2 \delta_{ac}^2 + \gamma_{ab}|\Omega_{ac}|^2 \delta_{ab}^2\right)},$$
(D.10)

Taking the difference between the signal at high H and low L power, but still with  $\delta_{cb} > \Omega$  we obtain

$$\operatorname{Re}\left[\gamma_{ab}\frac{\rho_{ab}}{\Omega_{ab}} - \gamma_{ac}\frac{\rho_{ac}}{\Omega_{ac}}\right]_{L}^{H} = \frac{\left(\gamma_{ac}|\Omega_{ab,H}|^{2} + \gamma_{ab}|\Omega_{ac,H}|^{2}\right)^{2}}{8\delta_{cb}\left(\gamma_{ac}|\Omega_{ab,H}|^{2}\delta_{ac}^{2} + \gamma_{ab}|\Omega_{ac,H}|^{2}\delta_{ab}^{2}\right)},$$
(D.11)

The constant term vanishes because I considered a proportional increase in power, meaning that the Rabi frequencies for high power can be expressed as the Rabi frequencies for low power multiplied by a scaling factor ( $|\Omega_{\rm H}| = \alpha |\Omega_{\rm L}|$ ). This expression ends up depending only on the high power Rabi frequency ( $\Omega_{nm,\rm H}$ ). Taking  $\gamma_{ab} = \gamma_{ac} = \gamma$  gives Eq. 2.76. I would like to find now the width and amplitude of the two-photon feature as it would appear in the signal Eq. 2.68 which can be visualized in Fig. 2.9. One can infer from the graph that the two-photon feature increases in width as the Rabi frequency increases. To estimate the width dependence, I look for the maximum and minimum points around the two-photon resonance, this means searching for the values of  $\delta_{cb}$  that fulfill the following equation

$$\frac{d}{d\delta_{cb}} \operatorname{Re} \left[ \gamma_{ab} \frac{\rho_{ab}}{\Omega_{ab}} - \gamma_{ac} \frac{\rho_{ac}}{\Omega_{ac}} \right] = 0.$$
 (D.12)

Using the same approximation that leads to Eq. D.6 I can write the difference of the coherences as

$$\operatorname{Re}\left[\gamma_{ab}\frac{\rho_{ab}}{\Omega_{ab}} - \gamma_{ac}\frac{\rho_{ac}}{\Omega_{ac}}\right] \approx \tag{D.13}$$

$$\frac{2\gamma^{2}|\Omega|^{2}\delta_{cb}\left(|\Omega|^{2}(b+c)^{2} - 4\delta_{cb}((c-b^{2})\delta_{ac} + c\delta_{cb})\right)}{16\gamma|\Omega|^{2}\delta_{cb}^{2}(b\delta_{ac}^{2} + c\delta_{ab}^{2}) + 8\gamma|\Omega|^{2}\delta_{cb}((b-c^{2})\delta_{ac} + \delta_{cb}c(1+b-c)) + \gamma|\Omega|^{6}(c+1)^{2}(b+c)},$$

with  $b = \gamma_{ac}/\gamma_{ab}$ ,  $c = |\Omega_{ac}|^2/|\Omega_{ab}|^2$  and  $\gamma_{ab} = \gamma$ ,  $|\Omega_{ab}| = |\Omega|$ . Next, I consider that  $c - b^2 \approx 0$  and  $c^2 - b \approx 0$  meaning that the Rabi frequencies are of similar value as well as the decay rates. I will also consider that the one-photon detunings are larger than the Rabi frequency ( $\delta^2 > |\Omega|^2$ ), with these considerations I can approximate the previous expression by

$$\operatorname{Re}\left[\gamma_{ab}\frac{\rho_{ab}}{\Omega_{ab}} - \gamma_{ac}\frac{\rho_{ac}}{\Omega_{ac}}\right] \approx \frac{2\gamma\delta_{cb}\left(|\Omega|^{2}(b+c)^{2} - 4\delta_{cb}^{2}\right)}{16\delta_{cb}^{2}(b\delta_{ac}^{2} + c\delta_{ab}^{2}) + |\Omega|^{4}(c+1)^{2}(b+c)},$$

Then by deriving this expression and finding the maximum and minimum I obtain the following values for  $\delta_{cb,\text{max}}$  and  $\delta_{cb,\text{min}}$ 

$$\delta_{cb,\text{max}} = \frac{1}{4} (|\Omega_{ab}|^2 + |\Omega_{ac}|^2) \sqrt{\frac{\gamma_{ac} |\Omega_{ab}|^2 + \gamma_{ab} |\Omega_{ac}|^2}{\gamma_{ac} |\Omega_{ab}|^2 \delta_{ac}^2 + \gamma_{ab} |\Omega_{ac}|^2 \delta_{ab}^2}},$$
 (D.14)

$$\delta_{cb,\min} = -\frac{1}{4} (|\Omega_{ab}|^2 + |\Omega_{ac}|^2) \sqrt{\frac{\gamma_{ac} |\Omega_{ab}|^2 + \gamma_{ab} |\Omega_{ac}|^2}{\gamma_{ac} |\Omega_{ab}|^2 \delta_{ac}^2 + \gamma_{ab} |\Omega_{ac}|^2 \delta_{ab}^2}}.$$
 (D.15)

Now I can calculate the width of the two-photon feature, which gives

$$\sigma_{\delta} = \delta_{cb,max} - \delta_{cb,min} \simeq \frac{1}{2} \left( |\Omega_{ab}|^2 + |\Omega_{ac}|^2 \right) \sqrt{\frac{\gamma_{ac} |\Omega_{ab}|^2 + \gamma_{ab} |\Omega_{ac}|^2}{\gamma_{ac} |\Omega_{ab}|^2 \delta_{ac}^2 + \gamma_{ab} |\Omega_{ac}|^2 \delta_{ab}^2}}.$$
 (D.16)

Taking  $\gamma_{ac} = \gamma_{ab}$ ,  $|\Omega_{ab}| = |\Omega_{ac}|$  and similar one photon detunings  $\delta_{ab} \simeq \delta_{ac}$  the signal difference between the two points of the width is

$$\operatorname{Re}\left[\gamma_{ab}\frac{\rho_{ab}}{\Omega_{ab}} - \gamma_{ac}\frac{\rho_{ac}}{\Omega_{ac}}\right]\Big|_{\delta_{cb,min}}^{\delta_{cb,max}} \simeq \frac{\gamma}{2\sqrt{\delta^2}} - \frac{3\gamma|\Omega|^2}{16\sqrt{\delta^2}^3},\tag{D.17}$$

and the phase difference change between the maximum and minimum is approximately given by

$$(\phi_1 - \phi_2)|_{\delta_{cb,min}}^{\delta_{cb,max}} = \text{OD} \times \text{Re} \left[ \gamma_{ab} \frac{\rho_{ab}}{\Omega_{ab}} - \gamma_{ac} \frac{\rho_{ac}}{\Omega_{ac}} \right] \Big|_{\delta_{cb,min}}^{\delta_{cb,max}} \simeq \text{OD} \frac{\gamma}{2|\delta|}, \tag{D.18}$$

with  $OD = N\sigma l$  the optical density.